

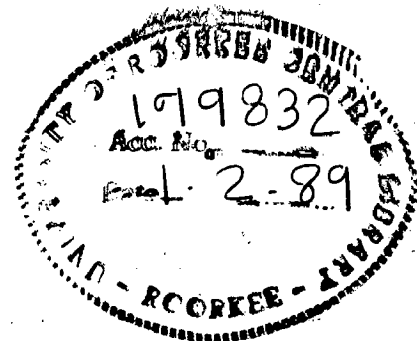
ANALYSIS OF CONNECTING-ROD BIG-END BEARING OF AN INTERNAL COMBUSTION ENGINE

A THESIS

submitted in fulfilment of the
requirements for the award of the degree
of
DOCTOR OF PHILOSOPHY
in
MECHANICAL ENGINEERING

By

ROSHAN PAL



DEPARTMENT OF MECHANICAL & INDUSTRIAL ENGINEERING
UNIVERSITY OF ROORKEE
ROORKEE-247 667 (INDIA)

September, 1987

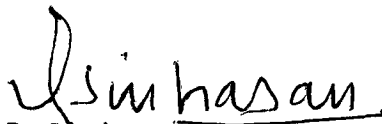
CANDIDATE'S DECLARATION

I hereby certify that the work which is being presented in the thesis entitled 'ANALYSIS OF CONNECTING-ROD BIG-END BEARING OF AN INTERNAL COMBUSTION ENGINE' in fulfilment of the requirement for the award of the Degree of Doctor of Philosophy, submitted in the Department of Mechanical and Industrial Engineering of the University is an authentic record of my own work carried out during a period from July, 1983 to Sept.1987 under the supervision of Dr. D.V.Singh and Dr.R.Sinhasan.

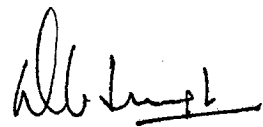
The matter embodied in this thesis has not been submitted by me for the award of any other degree.


(ROSHAN PAL)

This is to certify that the above statement made by the candidate is correct to the best of our knowledge.


(R.Sinhasan)
Professor

Mechanical and Industrial
Engineering Department,
University of Roorkee,
ROORKEE-247 667(INDIA)


(D.V.Singh)
Professor

Mechanical and Industrial
Engineering Department,
University of Roorkee,
ROORKEE-247 667(INDIA)

Date: Sept. 29, 1987

Place: ROORKEE

The Candidate has passed the Viva-Voce examination held on _____ at _____ . The thesis is recommended for award of the Ph.D. Degree.

Signature of Guide's

Signature of External Examiners



ACKNOWLEDGEMENT

With great pleasure I express my profound sense of gratitude to Dr.D.V.Singh and Dr.R.Sinhasan, Professors in Mechanical and Industrial Engineering Department, University of Roorkee, Roorkee, for kind help, keen interest and invaluable guidance throughout the research work leading to the completion of this thesis. Without their sustained interest, patience and sound counsel, this work would not have been possible.

I take this opportunity to express my sincere thanks and appreciation to Dr.P.C. Pandey, Professor and Head of Mechanical and Industrial Engineering Department, University of Roorkee for providing necessary research facilities.

I owe my gratitude to Prof.B.K. Kaul (the then Principal), Prof.P.V.Gupta, Principal and Dr.R.K. Bakshi, Professor in Mechanical Engineering Department (the then Chairman of Department), Regional Engineering college, KURUKSHETRA for encouraging and sponsoring me for this research assignment, and the Government of India for providing a fellowship under the Quality Improvement Programme.

My heartfelt thanks are due to Dr.Jia Lal, Programmer and other staff of Regional Computer Centre of University of Roorkee for cooperation and help for the consistent progress of this research work.

No expression is over adequate to express my thanks to my wife Saroj, son Anupam, and daughter Prerna for their patience and forebearance during the entire period of this work.

I dedicate this thesis to my father-in-law, Sri Sangram Singh, retired Principal, who had always desired me to engage in higher pursuits.


(ROSHAN PAL)

The connecting-rod big-end bearing, which is subjected to a complex dynamic loading, is an important component of an internal combustion engine. Gas force, inertia force due to the reciprocating masses (Piston, gudgeon pin, and small-end of the connecting-rod) and the centrifugal force due to the rotary mass of the connecting-rod big-end, contribute to the total load experienced by the big-end bearing, which varies in magnitude and direction. The relative speed of the bearing with respect to the crank pin is also variable. These factors make the analysis and design of the big-end bearing quite complex.

The existence of the fluid-film at all crank angles, consistent with its required minimum thickness in the clearance space of the big-end bearing, is imperative to obviate unnecessary wear and enhance the life of the system. Time history of the minimum film thickness depends on the motion of the bearing centre which has been studied by various investigators. A review of the available literature on the studies of the big-end bearing is presented in Chapter 1.

The literature indicates that some aspects of the big-end bearing analysis need further studies. With this view point, studies were planned in the area of the big-end bearing analysis to include the temperature and pressure (piezo-thermal) effects on viscosity, non-Newtonian lubricant characteristics, misalignment of the bearing and pin axes, effect of grooves, and deformation of the bearing body. Navier-stokes equations are used in the analysis instead of the traditional Reynolds equation so that variations of viscosity may be

accounted for piezoviscous, non-Newtonian and piezo-thermal effects.

This thesis work presents the solution of the following problems.

1. Rigid bearing with isoviscous lubricants,
2. Rigid bearing with piezoviscous lubricants,
3. Rigid bearing with the lubricants having piezo-thermal effects on viscosity,
4. Rigid bearing with non-Newtonian lubricants,
5. Rigid bearing (ungrooved) with axes(i) parallel and (ii) skewed,
6. Elastothermohydrodynamic (ETHD) lubrication.

The clearance space is discretized using three dimensional isoparametric elements by a mesh of $12 \times 4 \times 1$ elements, each containing 20 nodes. Full Sommerfeld boundary condition is used to solve the Navier-Stokes equation and the continuity equation. To account for the cavitation effect, all the negative values of the nodal pressures are replaced by zero. At each crank angle interval, the pressure and velocity fields are established by solving the momentum and continuity equations in the cylindrical coordinates. The finite-element formulation based on Galerkin's method and a direct iterative technique is used. The boundary conditions are substituted at the element stage to reduce the computer storage requirements. The global system equations are solved with each respective column of the right hand side to evaluate the pressure field contributions due to wedge, squeeze, and whirling actions of the fluid-film. In the case of deformation calculation, the three dimensional deformations in the bearing body are obtained by using the frontal solution technique to reduce the computer storage requirement. For the time marching scheme, Euler-Cauchy's predictor-corrector method is employed which is

found more suitable in comparison to Runge-Kutta or higher-order predictor-corrector methods (such as Adams-Moulton) for this problem.

The algorithm evolved in this work is general and can be used for the solution of any dynamically loaded circular bearings with isoviscous/piezoviscous/non-Newtonian lubricants, and can also handle piezo-thermal effects on viscosity. Using additional subroutines, the elastothermohydrodynamic effect is also studied. Deformations of the bearing body are computed using the hydrodynamic pressure developed in the fluid-film.

A summary of the studies based on the data of the big-end bearing of a Ruston-Hornsby 6VEB-X, Mk-III engine [10] reported in this thesis is given below.

The salient values in the column 3 refer to a SAE-30 oil (viscosity 14.95 mPa.s at 89°C)

Bearing specifications	Bearing characteristics	Salient value
1. Rigid bearing, isoviscous lubricants	(a) bearing centre orbit	-
	(b) minimum film thickness	3.85 μm
	(c) maximum film pressure	38.61 MPa
2. Rigid bearing, piezoviscous lubricants	(a) bearing centre orbit	-
	(b) minimum film thickness	4.09 μm
	(c) maximum film pressure	42.30 MPa
	(d) power loss	1.24 kW

3. Rigid bearing, piezo-thermal effects on viscosity	(a) bearing centre orbit	-
	(b) minimum film thickness	3.15 μm
	(c) maximum film pressure	48.07 MPa
	(d) maximum temperature rise	30°C
	(e) power loss	1.11kW

4. Rigid bearing, non-Newtonian lubricants (cubic shear stress law)	(a) bearing centre orbit	-
	(b) minimum film thickness	3.17 μm
	(c) maximum film pressure	41.10 MPa

5. Ungrooved bearing, parallel axes	(a) bearing centre orbit	-
	(b) minimum film thickness	9.10 μm
	(c) maximum film pressure	19.35 MPa

6. Ungrooved bearing, skewed axes ($\sigma = \delta = 0.0001$)	(a) bearing centre orbit	-
	(b) minimum film thickness	6.56 μm
	(c) maximum film pressure	28.25 MPa

The big-end bearing performance characteristics are also studied considering the bearing body deformation along with the lubricant having piezo-thermal viscosity characteristics. The results are obtained for a finite crank rotation with 2° interval.

The detailed results are presented in Chapter 6. A modular computer program is developed and described with the help of flow diagrams in Chapter 5. From the results obtained, it can be concluded that the minimum film thickness is comparatively smaller in the presence of non-Newtonian and piezo-thermal effects than those for lubricants either isoviscous or piezoviscous. The piezoviscosity effect on the minimum film thickness, however, noticeable only at high loads. The CPU time required for each of the cases of rigid

bearing is of the same order, but in the case of ETHD the CPU time is considerably more and is about ten times of that for the isoviscous case of the rigid bearing. For accurate analysis or design of the connecting-rod big-end bearing, it may however be necessary to consider ETHD lubrication but for most practical purposes one may analyze or design the big-end bearing as a rigid bearing with non-Newtonian lubricants or with the lubricants having piezo-thermal viscosity characteristics.

CONTENTS

CANDIDATE'S DECLARATION	...	i
ACKNOWLEDGEMENT	...	ii
ABSTRACT	...	iv
CONTENTS	...	ix
NOMENCLATURE	...	xiii
LIST OF FIGURES	...	xxii
LIST OF TABLES	...	xxv
CHAPTER 1	INTRODUCTION	... 1
CHAPTER 2	FLOW-FIELD	... 29
2.1.1	Navier-Stokes Equations (Cylindrical-Coordinates)	... 29
2.1.2	Continuity Equation	... 30
2.2	Boundary Conditions	... 30
2.3	Finite-Element Formulation	... 31
2.4	Non-Newtonian Lubricant Model-Analysis	... 36
2.4.1	Non-Newtonian Lubricant Models	... 37
2.4.2	Non-Newtonian Model Using Curve Fit (Curve-Fit Model)	... 39
2.5	Piezo-Thermal Viscosity Charact- eristics (Piezo-Thermal Effects)	... 42
2.5.1	Energy Equation	... 42
2.5.2	Boundary Conditions for Solution of Energy Equation	... 45
2.5.3	Viscosity Relation with Temperature and Pressure	... 45
2.5.4	Finite-Element Formulation for Energy Equation	... 45

CHAPTER 3	ELASTIC DEFORMATION	... 48
3.1	Big-End Bearing Material	... 48
3.2	Deformation in Bearing Body- Finite Element Formulation	... 49
3.3	Loading and Boundary Conditions	... 54
CHAPTER 4	BEARING CHARACTERISTICS	... 56
4.1	Bearing Force and Relative Motion...	56
4.2	Friction Force and Power Loss	... 61
4.3	Equations of Motion of the Bearing Centre	... 62
CHAPTER 5	SOLUTION SCHEME AND COMPUTER PROGRAM STRUCTURE	... 65
5.1	Solution Procedure to obtain Nodal Pressure, Velocity Fields and Fluid-Film Forces	... 66
5.1.1	Rigid Bearing	... 66
5.1.1a	Isoviscous Lubricants	... 66
5.1.1b	Piezoviscous Lubricants	... 69
5.1.1c	Lubricants having Piezo-Thermal Viscosity Characteristics	... 69
5.1.1d	Non-Newtonian Lubricants	... 73
5.1.1e	Misalignmeant of Axes	... 75
5.1.2	Flexible Bearing	... 77
5.2	Integration Scheme for the Equations of Motion of the Bearing Centre	... 78
5.2.1	Integration Scheme	... 78
CHAPTER 6	RESULTS AND DISCUSSIONS	... 83
6.1	Sample Problem	... 85
6.2	Discretization of Fluid-Film	... 86
6.3	Selection of the Method for Numerical Integration of the Equations of Motion of the Bearing Centre	... 86

6.4	Results and Discussions	... 89
6.4.1	Rigid Bearing with Isoviscous Lubricants	... 92
6.4.1a	Bearing Centre Orbit	... 92
6.4.1b	Maximum Film Pressure	... 94
6.4.1c	Minimum Film Thickness	... 94
6.4.2	Rigid Bearing with Piezoviscous Lubricants	... 97
6.4.2a	Bearing Centre Orbit	... 97
6.4.2b	Maximum Film Pressure	... 100
6.4.2c	Minimum Film Thickness	... 100
6.4.2d	Power Loss	... 100
6.4.3	Rigid Bearing with the lubricant having Piezo-Thermal Viscosity Characteristics (Piezo-Thermal case)	... 103
6.4.3a	Bearing Centre Orbit	... 103
6.4.3b	Maximum Film Pressure	... 103
6.4.3c	Minimum Film Thickness	... 106
6.4.3d	Maximum Temperature Rise	... 106
6.4.3e	Power Loss	... 109
6.4.4	Rigid Bearing with Non-Newtonian Lubricants	... 109
6.4.4(i)	Cubic Shear Stress Law Model	... 109
6.4.4(i)a	Bearing Centre Orbit	... 109
6.4.4(i)b	Maximum Film Pressure	... 112
6.4.4(i)c	Minimum Film Thickness	... 114
6.4.4(ii)	Curve-Fit Model	... 114
6.4.5	Ungrooved Rigid Bearing with Isoviscous Lubricants	... 118
6.4.5(i)	Parallel Axes System	... 118
6.4.5(i)a	Bearing Centre Orbit	... 118

6.4.5(i)b	Maximum Film Pressure	... 122
6.4.5(i)c	Minimum Film Thickness	... 122
6.4.5(ii)	Skewed Axes System	... 122
6.4.5(ii)a	Bearing Centre Orbit	... 122
6.4.5(ii)b	Maximum Film Pressure	... 124
6.4.5(ii)c	Minimum Film Thickness	... 124
6.4.6	Elastothermohydrodynamic (ETHD) Lubrication Study of the Big-End Bearing	... 128
6.5	Computational CPU Time	... 135
6.6	Conclusions	... 137
6.6.1	Algorithm and the Computer Program	... 137
6.6.2	Bearing Performance	... 138
	CLOSURE	... 141
	REFERENCES	... 143
	APPENDICES	
A-1	List of Non-Newtonian Oils	... 149
A-2	Heat Balance Condition	... 150
A-3	Predictor-Corrector Formulae	... 154
A-4	Data for the Ruston-Hornsby 6VEB-X Mk-III Engine Big-End Bearing	... 155
A-5	Expression for Film Thickness in Skew Axes System	... 159
A-6	The Big-End Bearing Equilibrium Locus	... 163

NOMENCLATURE

A	acceleration of the piston
a_0, \dots, a_4	coefficients of the polynomial
\bar{B}	aspect ratio (L/2R)
c	radial clearance
C_v	specific heat of lubricant
C_1, C_2, C_3	constants for different non-Newtonian models
D	diameter of the engine cylinder
d_x, d_z, d_e	components of bearing body deformation
$\bar{d}_x, \bar{d}_z, \bar{d}_e$	components of bearing body deformation (non-dimensional)
dV, dV'	elemental volume for fluid and bearing body respectively
dA, dA'	elemental area for fluid and bearing body respectively
E	Young's modulus of bearing body material
e_m	total number of elements in the elastic continuum of bearing body
F	external force on crank pin
F_I	inertia force of the reciprocating engine parts
F_G	gas force in the cylinder
F_1	centrifugal force of the rotating mass
F_2	force component transmitted to the bearing through connecting-rod
$\bar{F}_s(\dot{\epsilon}, \dot{\beta})$	fluid-film force along line of centres due to squeeze and whirling actions of fluid
$\bar{F}_n(\dot{\epsilon}, \dot{\beta})$	fluid-film force normal to the line of centres due to squeeze and whirling actions of fluid
F_x, F_z, F_θ	force components of surface traction
$\bar{F}_x, \bar{F}_z, \bar{F}_\theta$	force components of surface traction (non-dimensional)

\bar{F}_{01}	coefficient of column vector for surface traction force
F_f	friction force
\bar{F}_f	friction force (non-dimensional)
G_1, G_2, G_3	Coefficients of elasticity matrix
H	enthalphy
h_c	convective heat transfer coefficient
\bar{h}	fluid-film thickness
K_m	thermal conductivity of bearing material
K_o	thermal conductivity of lubricant
\bar{K}_{d13}	coefficients of fluidity matrix in EHD part
\bar{K}_{mn}	coefficients of fluidity matrix in hydrodynamic part
L	length of bearing or length of one land of bearing which having circumferential groove
L_1	length of connecting-rod
M^*	shape function for deformation variation
M_p	shape function for pressure variation
M_1	equivalent mass of connecting-rod at small-end (=1/3 of total mass)
M_2	equivalent mass of connecting-rod at big-end (=2/3 of total mass)
\bar{M}_2	mass at big-end (non-dimensional)
M_p	mass of piston and its accessories
M_T	total mass of connecting-rod
N_B	bearing speed
N_1	shape function for velocity and temperature variation
\bar{p}	fluid-film pressure (non-dimensional)
P_c	gas pressure inside the cylinder
P_r, P_z, P_θ	components of nodal pressure in r, z, θ direction
\bar{p}_h	fluid-film pressure due to wedge action

\bar{p}_e	fluid-film pressure due to squeeze action per unit of squeeze velocity
\bar{p}_w	fluid-film pressure due to whirl action per unit of whirl velocity
P	power loss
q	ratio of connecting-rod length to crank radius (L_1/R_1)
Re	average Reynolds number ($= \rho \Omega R c / \mu_o$)
R	radius of crank pin
R_1	crank radius
\bar{R}	(R/c)
R_B, R_i	bearing inner surface radii
R_o	bearing outer surface radius
\bar{R}_B	($(R+c)/t_h$)
\bar{r}	non-dimensional radial coordinate in hydrodynamic part (r/c)
\bar{r}'	non-dimensional radial coordinate in EHD part (r'/t_h)
r	radial coordinate of system measured from bearing centre
r'	radial coordinate of nodes in the bearing body measured from bearing centre
\bar{S}_1, \bar{S}_4	fluid-film force components due to wedge action along and normal to the line of centres respectively
\bar{S}_2, \bar{S}_5	damping coefficients due to squeeze action along and normal to the line of centres respectively
\bar{S}_3, \bar{S}_6	damping coefficients due to whirl action along and normal to the line of centres respectively
T	temperature
T_o	operating temperature
T_B	temperature at bearing outer surface
T_a	surrounding temperature
\bar{T}	non-dimensional temperature (T/T_o)
\bar{T}_B	non-dimensional bearing inner surface temperature (T_B/T_o)

\bar{T}_s	non-dimensional crank pin surface temperature (T_s/T_o)
t	time
\bar{t}	non-dimensional time (Ωt)
t_h	bearing body thickness
\bar{t}_h	(t_h/R)
$\bar{u}, \bar{v}, \bar{w}$	fluid velocity components in θ, r, z directions respectively (non-dimensional)
V_θ, V_r, V_z	fluid velocity components in θ, r, z directions respectively
W	external load on the bearing
\bar{W}	external load on the bearing (non-dimensional)
\bar{W}_a	load component along line of centres
\bar{W}_n	load component normal to the line of centres
\bar{z}	axial coordinate of the bearing in hydrodynamic part (z/R)
\bar{z}'	axial coordinate of the bearing in EHD part (z'/t_h)
z	axial coordinate of bearing measured from central plane
z'	axial coordinate of node inside the bearing body measured from central plane of the bearing (or bearing land)
α_1	angle between connecting-rod axis and crank axis, Fig.4.1
α	position of load vector measured from an axis parallel to the engine axis, Fig.4.1
$\bar{\alpha}_p$	piezoviscous coefficient (non-dimensional)
β	angular position of line of centres measured from an axis parallel to the engine axis, Fig.4.4
$\dot{\bar{\beta}}$	whirl velocity ($d\bar{\beta}/d\bar{t}$)
$\ddot{\bar{\beta}}$	whirl acceleration ($d^2\bar{\beta}/d\bar{t}^2$)
$\bar{\beta}_T$	viscosity-temperature coefficient

$\gamma_x, \gamma_z, \gamma_\theta$	elements of strain matrix
$\gamma_{xe}, \gamma_{re}, \gamma_{rz}$	
$\dot{\gamma}$	shear strain rate
$\bar{\dot{\gamma}}$	non-dimensional shear strain rate
σ, δ	angle between bearing and pin axes due to misalignment (Appendix A-5)
e	eccentricity ratio
\dot{e}	squeeze velocity ($d\bar{e}/dt$)
\ddot{e}	squeeze acceleration
θ	angular coordinate measured from the position of the maximum fluid-film thickness in the bearing clearance
θ_1	crank angular rotation
θ_{1i}	instantaneous i^{th} value of crank angle
μ_p	Poisson's ratio
μ_o	viscosity at ambient pressure and operating temperature
μ_a	apparent viscosity
$\bar{\mu}_a$	non-dimensional apparent viscosity
$\bar{\mu}_\infty$	apparent viscosity at infinite shear rate
π	3.1415926
\mathcal{P}	potential energy
θ_1	connecting-rod angular rotation
θ_v	viscous dissipation term of energy equation
$\bar{\theta}_v$	nondimensional viscous dissipation term
ρ	fluid-density
$\bar{\Phi}$	deformation coefficient
Ω	angular crank speed
R_T	total heat resistance

Ω_1	angular speed of bearing rotation relative to the crank pin speed
τ	shear stress
$\bar{\tau}$	non-dimensional shear stress
ξ, η, ζ	local coordinates in θ, r, z directions respectively

Matrices

$\{\bar{a}\}$	global column vector for unknown quantities
$[B_a]$	$[L] [M^*]$
$\{d\}$	column vector for nodal displacements
$\{\bar{d}\}$	column vector for non-dimensional nodal displacements
$[D_a]$	elasticity matrix
$[\bar{D}_a]$	non-dimensional elasticity matrix
$\{F_o\}$	column vector for nodal traction forces
$\{\bar{F}_o\}$	column vector for non-dimensional nodal forces
$\{\bar{F}_\tau\}$	column vector for viscous dissipation term
$[\bar{G}]$	element fluidity matrix in hydrodynamic part
$[J]$	Jacobine matrix
$ J $	determinant of Jacobian matrix
$ J_a $	determinant of Jacobian matrix in two dimension
$[\bar{K}]$	global fluidity matrix in hydrodynamic part
$[\bar{K}^v]$	submatrix for viscous terms
$[\bar{K}^p]$	submatrix for pressure terms
$[\bar{K}^c]$	submatrix for continuity equation terms
$[K_a]$	global fluidity matrix in EHD part
$[\bar{K}_a]$	global fluidity matrix in non-dimensional
$[\bar{K}_\tau]$	fluidity matrix for temperature field
$[L]$	operator matrix
$[M^*]$	shape function matrix in EHD part

$\{\bar{R}_A\}^+$	column vector for right hand side for wedge action
$\{\bar{R}_w\}^+$	column vector for right-hand side for whirl terms
$\{\bar{R}_s\}^+$	column vector for right-hand side for squeeze terms
$\{T_x\}$	column vector for traction forces
$[T_x]$	row vector for traction forces
$\{\bar{T}\}$	column vector for temperature
$\{\bar{\theta}_u\}$	sub-column vector for velocity variables for element equation
$\{\bar{\theta}_p\}$	sub-column vector for pressure variables for element equation
$\{\bar{\theta}\}$	column vector for nodal velocities ($\bar{u}, \bar{v}, \bar{w}$) and nodal pressuree (p) for the entire assemblage
$\{S\}$	column vector for nodal displacement components.
$\{Y\}$	strain column matrix
$[\sigma]$	stress row matrix
$[S]$	row vector for nodal displacement components.

+ vectors $\{\bar{R}_A\}$, $\{\bar{R}_w\}$ and $\{\bar{R}_s\}$ are for the entire assemblage obtained after applying the boundary conditions

MULTIPLICATION FACTORS FOR OBTAINING DIMENSIONAL VALUES

Non-dimensional quantity	Multiplication factor
$\bar{d}_x, \bar{d}_z, \bar{d}_\theta, \bar{h}, \bar{r}, \bar{R}$	c
$\bar{F}_x, \bar{F}_z, \bar{S}_1, \bar{S}_2, \bar{W}, \bar{W}_x, \bar{W}_z$	$\mu_0 R^2 \Omega (R/c)^2$
$\bar{F}_x, \bar{F}_z, \bar{F}_\theta, \bar{F}_\phi$	$\mu_0 \Omega (R/c) t_h^2$
$\bar{d}V$	$R^2 c$
$\bar{d}V'$	t_h^3
dA	R^2
$\bar{d}A'$	t_h^2
\bar{F}_z	$\mu_0 R^2 \Omega (R/c)$
\bar{M}_2	$c^3 \Omega / (\mu_0 R^4)$
\bar{P}	$\mu_0 \Omega (R/c)^2$
\bar{P}	$\mu_0 R^3 \Omega^2 (R/c)^2$
$\bar{R}_B, \bar{r}', \bar{z}'$	t_h
$\bar{u}, \bar{v}, \bar{w}$	$R \Omega$
\bar{t}	$(1/\Omega)$
\bar{z}	R
$\bar{\alpha}_p$	$[1/(\mu_0 \Omega (R/c)^2)]$
$\bar{\alpha}_1, \bar{\beta}, \bar{\epsilon}$	Ω
$\bar{\beta}, \bar{\epsilon}$	Ω^2
$\bar{\gamma}$	$R \Omega / c$
$\bar{\mu}, \bar{\mu}_x, \bar{\mu}_z$	μ_0
$\bar{\Gamma}$	$\mu_0 R \Omega / c$
$\bar{\Phi}$	$(\mu_0 \Omega / E) (t_h / R) (R/c)^3$

SUBSCRIPTS AND SUPERSCRIPTS

-(bar)	Superscript for non-dimensional quantities
.(dot)	Superscript for derivative with respect to time
..(double dot)	superscript for acceleration
T	superscript for transpose of a matrix
e	superscript for element numbers
i,j	subscript for local node numbers
m,n	subscript for global node numbers
p	superscript for predicted values Chapter 5
c	superscript for corrected values Chapter 5

LIST OF FIGURES

Fig. No.	Title	Page
1.1	Sectional view of a connecting-rod and piston assembly	... 2
1.2	Predicted journal centre cyclic paths for the Ruston-Hornsby 6VEB-X Mk-III engine connecting-rod bearing [10]	... 8
1.3	Minimum oil film thickness comparison (results from engine, similarity machine and theoretical methods) [10]	... 11
1.4	Oil passages for lubrication of engine bearings	... 24
1.5	Circumferential grooved bearing showing effect on pressure distribution	... 24
2.1	Apparent viscosity as a function of shear rate for commercial oil (C-2) at 210°F	... 41
3.1	Big-end bearing geometry	... 55
4.1	Forces acting on a slider crank mechanism	... 57
4.2	Polar force diagram for the big-end bearing	... 59
4.3	Variation of bearing speed	... 60
4.4	Kinematic and dynamic quantities for a journal bearing system	... 63
5.1a	Flow diagram for mesh generation (Subroutine ATODAT)	... 68
5.1b	Flow diagram for the hydrodynamic problem (BLOCK-I)	... 70
5.2	Flow diagram for piezoviscous effect (BLOCK-II)	... 71
5.3	Flow diagram for piezo-thermal effects (BLOCK-III)	... 74
5.4	Flow diagram for solution with non-Newtonian lubricants (BLOCK-IV)	... 76
5.5	Flow diagram for solution of the elastic problem (BLOCK-V)	... 79
5.6	Flow diagram for the time marching scheme	... 82
6.1	Discretization of a symmetric half of the bearing (one land)	... 88
6.2	Element	... 88

6.3	Comparison of load capacity for non-Newtonian lubricants using cubic shear stress law (static load)	91
6.4	Bearing centre orbit (Isoviscous case)	93
6.5	Variation of maximum film pressure (Rigid bearing, isoviscous case)	95
6.6	Variation of minimum film thickness (Rigid bearing, isoviscous case)	96
6.7	Bearing centre orbit (Piezoviscous case)	99
6.8	Variation of maximum film pressure	101
6.9	Variation of minimum film thickness	102
6.10	Power loss as a function of crank angle (Rigid bearing, piezoviscous case)	104
6.11	Bearing centre orbit (Piezo-Thermal case)	105
6.12	Variation of maximum film pressure	107
6.13	Variation of minimum film thickness	108
6.14	Variation of maximum temperature rise (Rigid bearing, piezo-thermal case)	110
6.15	Comparison of power loss	111
6.16	Bearing centre orbit (Non-Newtonian case, cubic shear stress law model)	113
6.17	Variation of maximum film pressure	116
6.18	Variation of minimum film thickness	117
6.19	Bearing centre orbit of the big-end bearing without circumferential groove (Parallel axes case)	119
6.20	Variation of maximum film pressure	120
6.21	Variation of minimum film thickness	121
6.22	Bearing centre orbit of the big-end bearing without circumferential groove (skewed axes case)	123
6.23	Variation of maximum film pressure	125
6.24	Variation of minimum film thickness	126
6.25a	Deformation pattern of bearing body at 260° crank angle	131

6.25b	Deformation pattern of bearing body at 270° crank angle	... 132
6.25c	Deformation pattern of bearing body at 280° crank angle	... 133
6.25d	Deformation pattern of bearing body at 300° crank angle	... 134
A-5.1	Axes misalignment in bearing system	... 162
A-6.1	Bearing center equilibrium locus	... 164

LIST OF TABLES

Table No.	Title	Page
2.1	Apparent viscosities of non-Newtonian oils [66] as function of shear rate at 99°C (210°F)	... 40
2.2	Values of the Coefficients (a_0, a_1, a_2, a_3, a_4) for the polynomial, Eq.(2.20) representing the non-linear relation between the apparent viscosity (μ_a) and shear rate ($\dot{\gamma}$) for different non-Newtonian oils	... 43
6.1	Studies for the rigid big-end bearing	... 84
6.2	Comparison of the results obtained by Euler-Cauchy's predictor-corrector and Runge-kutta-higher-order predictor-corrector methods	... 87
6.3	Static performance of circular bearing (aspect ratio 1.0) and its comparison with the data available in the literature	... 90
6.4	Comparison of the minimum film thickness obtained in the isoviscous case with the experimental and theoretical values available in the literature for the Ruston-Hornsby 6 VEB-X, MK-III engine big-end bearing	... 98
6.5	Comparison of the results obtained for the big-end bearing with non-Newtonian lubricants (cubic shear stress law and curve-fit model)	... 115
6.6	Deviations in the minimum film thickness and the maximum peak pressure for the rigid bearing cases	... 127
6.7	Values of ϵ, β , the minimum film thickness (h_{min}), the maximum temperature rise (T_{max}), and the maximum deformation at the inner surface of the bearing body (d_{rmax}) in the elastothermohydrodynamic lubrication case for finite crank rotation	... 129
6.8	CPU time required for the cases studied	... 135
A-4.1	Force components (SI units) on the connecting-rod big-end bearing of the Ruston-Hornsby 6VEB-X, Mk-III engine relative to the cylinder axis	... 156

CHAPTER 1

INTRODUCTION

The internal combustion engines particularly the diesel engines, are the most widely used energy conversion devices employed as prime-movers. Of their many important components, the big-end bearing, Fig. 1.1, certainly is one. The performance of the big-end bearing of an internal combustion engine is therefore critical for the satisfactory performance of the engine as a whole.

The performance of the big-end bearing has been a subject of extensive investigations, both, theoretically and experimentally for the last two decades. This Chapter aims at presenting the state-of-the-art on the analysis and design of the big-end bearing which is subjected to a complex dynamic loading that varies both in magnitude and direction during each cycle of the engine. The gas force, the inertia force due to reciprocating masses and the centrifugal force due to rotary mass of the engine are the main forces which act on the big-end bearing. For computation of the total inertia forces at the big-end bearing, masses of the connecting-rod, piston and other accessories may be represented by an equivalent mass system comprising a reciprocating mass at the piston-end and a rotating mass at the big-end of the connecting-rod. The gas force acting on the piston and the inertia force due to the equivalent mass at the piston-end is communicated to the big-end bearing through the connecting-rod. These forces are vectorially added to the inertia force due to the equivalent mass at the big-end to determine the resultant dynamic force on the big-end bearing.

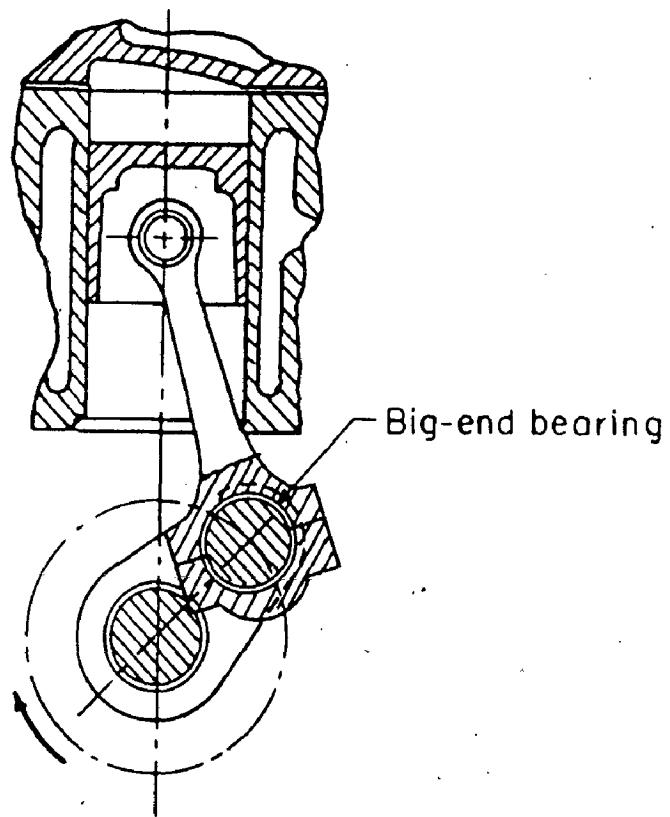


Fig. 1.1 Sectional view of a connecting-rod and piston assembly

In the big-end bearing design, due consideration is given to the existence of the fluid-film in the clearance space between the bearing and the crank pin surface. The possibility of metal to metal contact between the pin and the bearing surfaces in the running condition should be minimized by suitably designing the bearing.

The minimum fluid-film thickness in the hydrodynamic bearings depends on the following parameters.

(i) Hydrodynamic parameters: Load, speed, constitutive behaviour of lubricant, oil film history, dilution of fuel in lubricant, contamination of lubricant and flow condition etc.

(ii) Geometrical parameters : Bearing shape, clearance geometry, oil holes and grooves, oil drain system, misalignment between bearing and journal axes, aspect ratio etc.

(iii) Elastohydrodynamic parameters: Bearing liner material, rigidity of housing structure, etc..

The performance of a journal bearing subjected to a load which varies both in magnitude and direction with time, was first investigated in 1920 by Harrison [36] and was later studied by Swift [58] in 1937. Harrison and Swift showed that the load capacity of bearing may vary considerably in dynamic condition in comparison to that in the static condition. In 1947, Burwell [1] discussed in detail, the equations for the film pressure and load capacity of a dynamically loaded bearing. In deriving the equation for pressure, the usual assumptions of the hydrodynamic theory were considered and the results were obtained for a diesel-engine connecting-rod big-end bearing, and a radial-aircraft-engine master-rod bearing. In the case of the diesel-engine big-end bearing, the maximum eccentricity ratio = 0.989 was calculated which is equivalent to a

minimum film thickness of 0.000011in during the cycle and in the case of radial- aircraft engine master-rod bearing, the maximum eccentricity ratio was 0.88.

In ASME-ASLE Lubrication Conference, 1956, three papers were presented on the experimental work on big-end bearings. Pigott and Walsh [48] described their Universal Bearing Tester; Hersay, and Snapp [27,59] presented two papers in which Bearing Test Machines with dynamic loading or non uniform motion were described and classified according to the type of loading employed. In these three studies [27,48,59] the engine bearings were tested for wear and fatigue failure.

Russell [52] developed a machine for testing the bearings subjected to the impulsive type of load produced in compression-ignition-engines. The procedure for assessing the load capacity of bearings were described and the maximum impulsive pressure to cause failure in bearings of different materials were given in tabular form. After conducting a large number of experiments on an engine big-end bearing, the following conclusions were drawn. (i) with the tin-base and lead-base linings the reduction of the thickness of the linings from 0.508 mm (0.02in) to 0.1524mm (0.006in) increases the load capacity, (ii) the copper-lead linings produced by the sintering process have higher-load-carrying capacity than the cast copper-lead lining, (iii) the use of low viscosity oil reduces the running temperature of bearings .

In 1961, Blount [2] studied the effects of some design parameters on the fatigue resistance of big-end bearing experimentally. He used various combinations of bearing materials and measured the fatigue strength under static and dynamic load. In

'the case of big-end bearings, he studied the influence of housing rigidity, effect of shell thickness, oil groove and bearing clearance. He concluded that it was common place to blame fatigue failures of the bearing shell whereas the bearings might well be blameless and suffering might come only from the weaknesses of its companion housing. He also concluded that (i) ungrooved bearing have a higher fatigue strength, (ii) during the firing load, an oil groove in the engine bearing does not reduce its temperature, (iii) variations in diametral clearance affect the fatigue life, and (iv) the aluminium-tin shell bearings appeared to have quite high fatigue strength.

Horsnell and McCallion [28] made an attempt to take into account more accurately the effects of oil film disruption in a finite width journal bearing and to estimate their importance by comparison with an evaluation ignoring such disruptions. It was assumed that in the cavitation region, the lowest possible pressure was constant and equal to the vapour pressure. The solution of the governing equations was obtained by a relaxation technique and the method was applied to the main bearings of a diesel engine subjected to dynamic load.

Carl [9] and Radermacher [53] presented their experimental work which was done on bearings subjected to sinusoidal loading or loads varying in magnitude and direction.

For the analysis of dynamically loaded bearings, a graphical method called Mobility Method which can also be applied for big-end bearings, was presented by Booker [3]. The limitation of the mobility method is that it is only applicable for bearings with circumferential symmetry and axially straight profile (ideal

bearings).

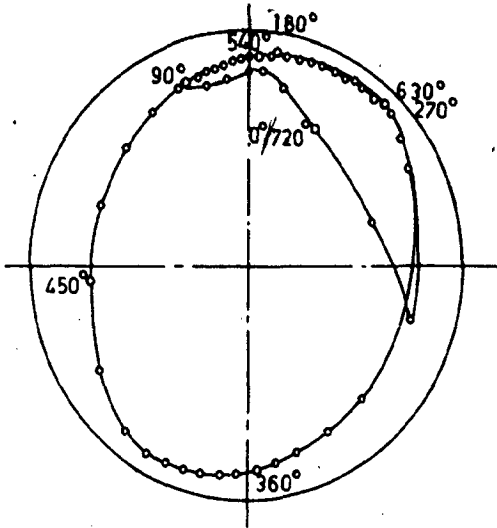
Lloyd, Horsnell and McCallion [38,39] investigated the performance of dynamically loaded finite bearings using a high speed digital computer. In the first paper [38], they presented the theory of the method used. The method rests on the assumptions that the oil film is isothermal and the inertia forces associated with the bearing accelerations are not important. Numerical solutions of the Reynolds equation were obtained and stored for both wedge and squeeze film terms, at a number of bearing eccentricities which require a large storage in the computer. At intermediate eccentricities, the required pressures were obtained by interpolation. Finite difference method was used to solve the finite bearing problem. In the second paper [39] they demonstrated the use of the method described in [38] by studying the main and big-end bearing of a diesel engine and drew some useful conclusions; (i) an increase in the minimum film thickness by 14% and a decrease in the peak pressure by 3% was noticed when the effect of connecting-rod obliquity was neglected, (ii) the minimum oil film thickness decreased with the increase of inertia load, since the maximum load is caused principally by the gas load, which the inertia load opposes. The result was that the maximum cycle load decreases with the increase of inertia load, (iii) the most striking change affected by the increase of bearing clearance was the reduction in the temperature rise across the bearing.

McCallion, H., et al [43] also developed a test rig to verify their theoretical results [38]. Two perpendicular load components were applied mechanically through cam driven spring levers. Load records and journal loci were obtained and compared with the results

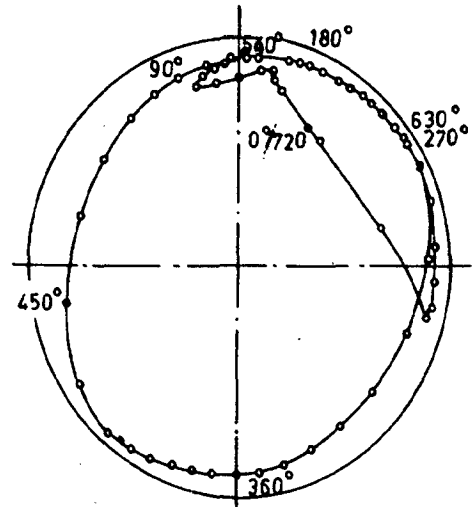
from computer program described in [38]. Correlation between the theoretical and experimental results was good. The measured load carrying capacity was, however, found to be lower than that predicted. This may be accounted for by the variation of oil viscosity with temperature.

Martin and Booker [44], have studied the influence of engine inertia forces on the minimum film thickness in the big-end bearing using the engine data from Ref. [38]. The effects of connecting-rod obliquity and clearance on the minimum film thickness were studied using the numerical mobility method with π -film and short bearing approximations. They concluded that the eccentricity ratio in the big-end bearing due to peak firing load seldom exceeds that due to the inertia load alone, although this load was smaller than the peak firing load. Therefore, as an approximation, the gas force was neglected in the study. The effect of a reasonable change in crank throw to connecting-rod length ratio on minimum film thickness was found to be small. For a more practical range of eccentricity ratios encountered (above 0.80), the oil film thickness was found to increase with decrease in clearance.

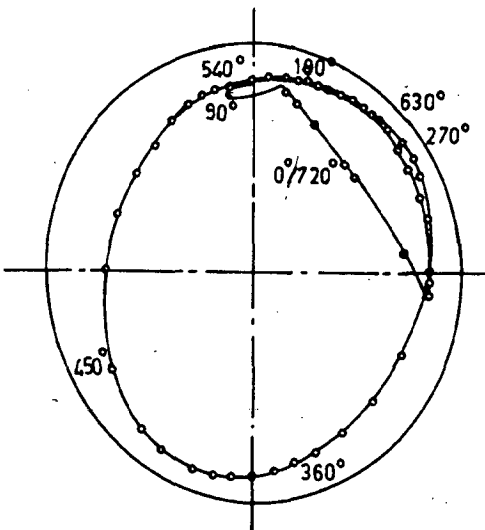
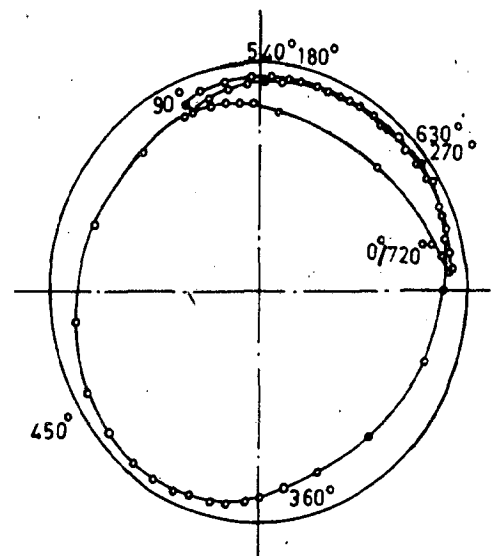
Campbell et al [10], compiled the research work which was carried out before 1967-68 and presented the methods of solution and the results for big-end bearings in a very systematic way. This review paper has proved very helpful to the big-end bearing design engineers and investigators. To analyze the big-end bearing, most of the investigators have selected the Ruston-Hornsby 6 VEB-X Mk-III engine as an example. In this review, the results for the 6 VEB-X engine big-end bearing were presented with greater emphasis. The journal centre cyclic paths, Fig.1.2, and variation of the minimum



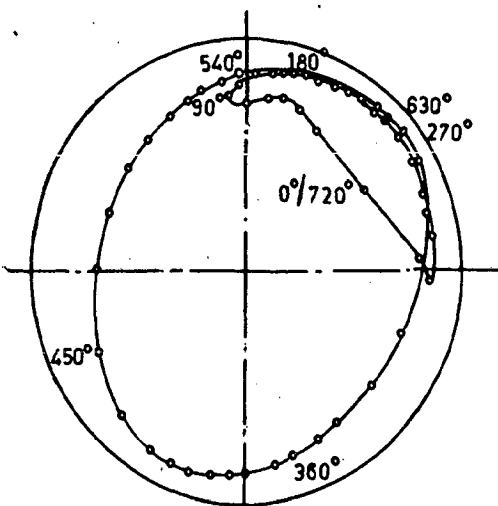
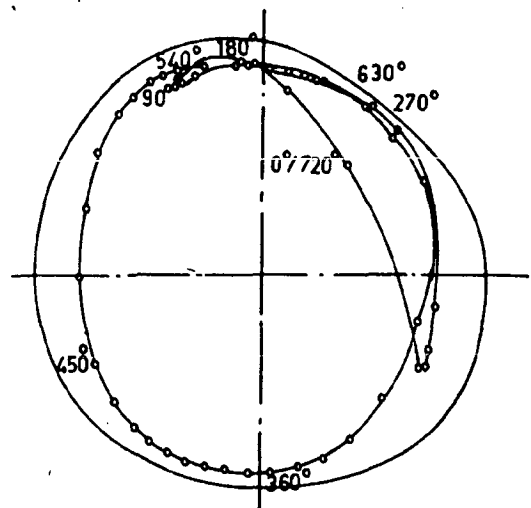
(g) Cyclic path computed by Horsnell



(h) Cyclic path computed by Lloyd

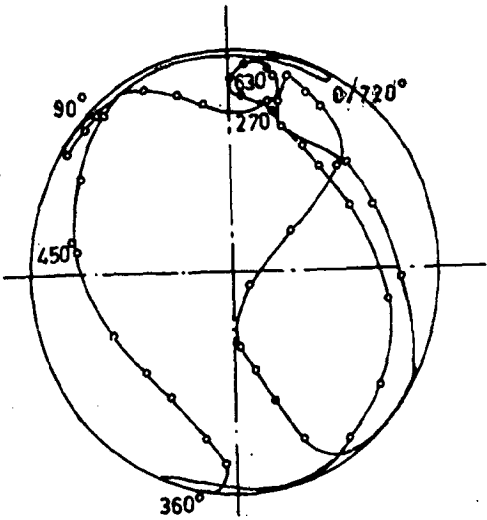
(j) Cyclic path based on Hahn Someya solution, computed by Karlsruhe Technical University (N.B. $b/d=0.5$ instead of 0.282)

(k) Cyclic path based on modified Holland solution, computed by Rheinstahl Hanomag Programme

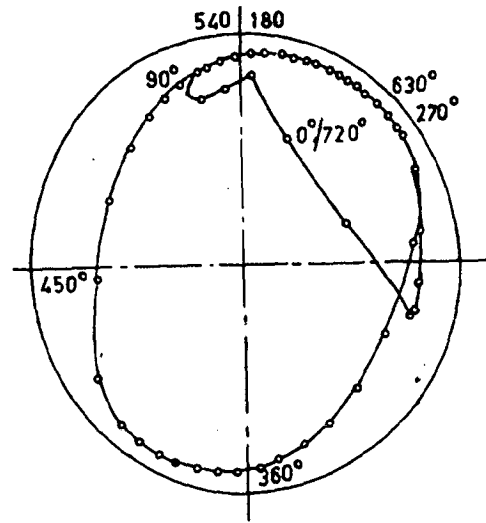
(l) Cyclic path based on Hahn-Someya solution, computed by Rheinstahl Hanomag Programme 2 (N.B. $b/d=0.5$ instead of 0.282)

(m) Cyclic path from the dynamic similarity machine at Glacier Metal Co. Ltd.

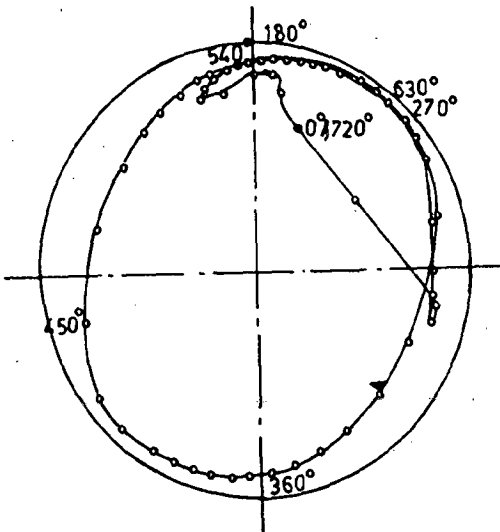
Fig.1.2. Predicted journal centre cyclic paths for the Ruston-Hornsby 6 VEB-X Mk-III connecting-rod bearing [10]



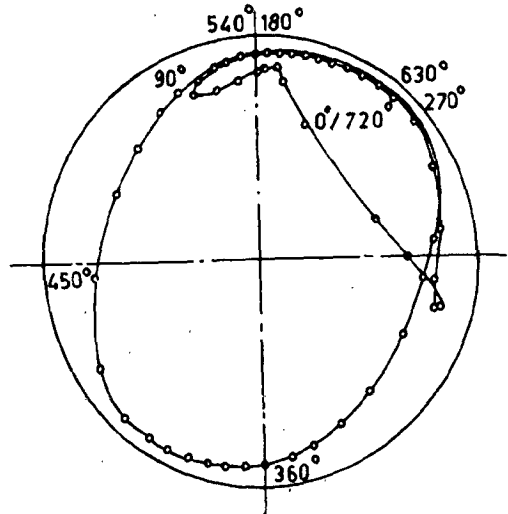
(a) Cyclic path using equivalent speed concept.



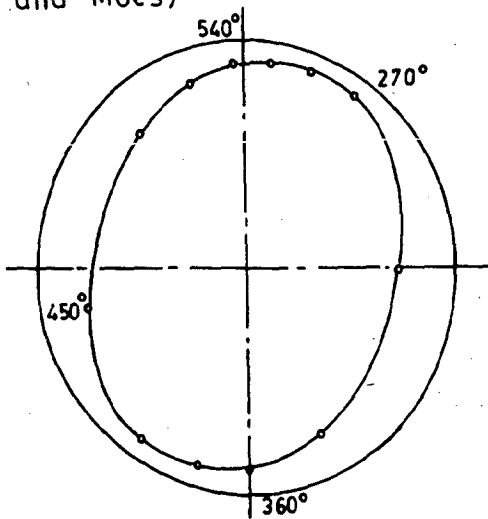
(b) Cyclic path based on Booker (short bearing theory) (author's graphical method)



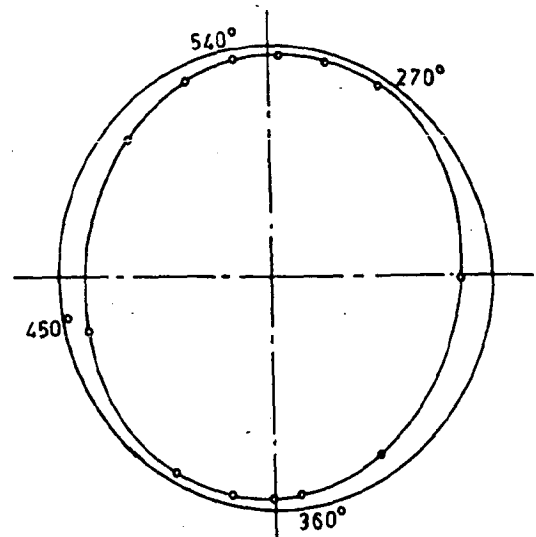
(c) Cyclic path by Blok's graphical method as carried out by the authors (using iso-impulse map based on Herrebrugh and Moes)



(d) Computed cyclic path as computed and carried out by Herrebrugh and Moes



(e) Cyclic path computed by Booker (using short bearing theory and inertia loading only)



(f) Cyclic path computed by Booker (using Warner finite bearing theory and inertia loading only)

film thickness, Fig.1.3, obtained by other investigators using constant viscosity and different techniques were reviewed. These techniques vary in their approximating assumptions, computation time, and method of solution.

Butcher [4] conducted the experiment on the same 6 VEB-X engine in 1967-68 and measured the oil film thickness in one complete cycle with the help of capacitance transducers. He plotted the variation of the minimum film thickness against crank angle and found the value of the minimum film thickness as $3.17\mu\text{m}$ (0.000125in).

Lloyd and McCallion [40] presented another computer program with modifications for the design of the big-end and the main bearings of the diesel engine. They claimed that their computer program has the capability to solve bearing problems of (i) two or four strokes cycle engine, (ii) multi-cylinder engine, (iii) Vee engines having different firing orders in two cylinders, (IV) different gas load cycles in the cylinders, and (V) articulated connecting-rod configuration. The computer program can also analyze the main bearings. The oscillation of the big-end bearing was included in the analysis. The program can accommodate one or two lands in the bearing but it can not handle bearing deformation, axial grooving, non-circular bearings, partial circumferential grooving or oil holes.

The viscosity of the lubricating oils significantly varies with temperature. Hence it is necessary to know the temperature rise in the fluid-film of the big-end bearing accurately. Furuhamu [15] attempted to measure temperature variations in the big-end bearing with thermocouples. He developed a system to measure the temperature in various parts such as piston, small-end, connecting-rod, big-end

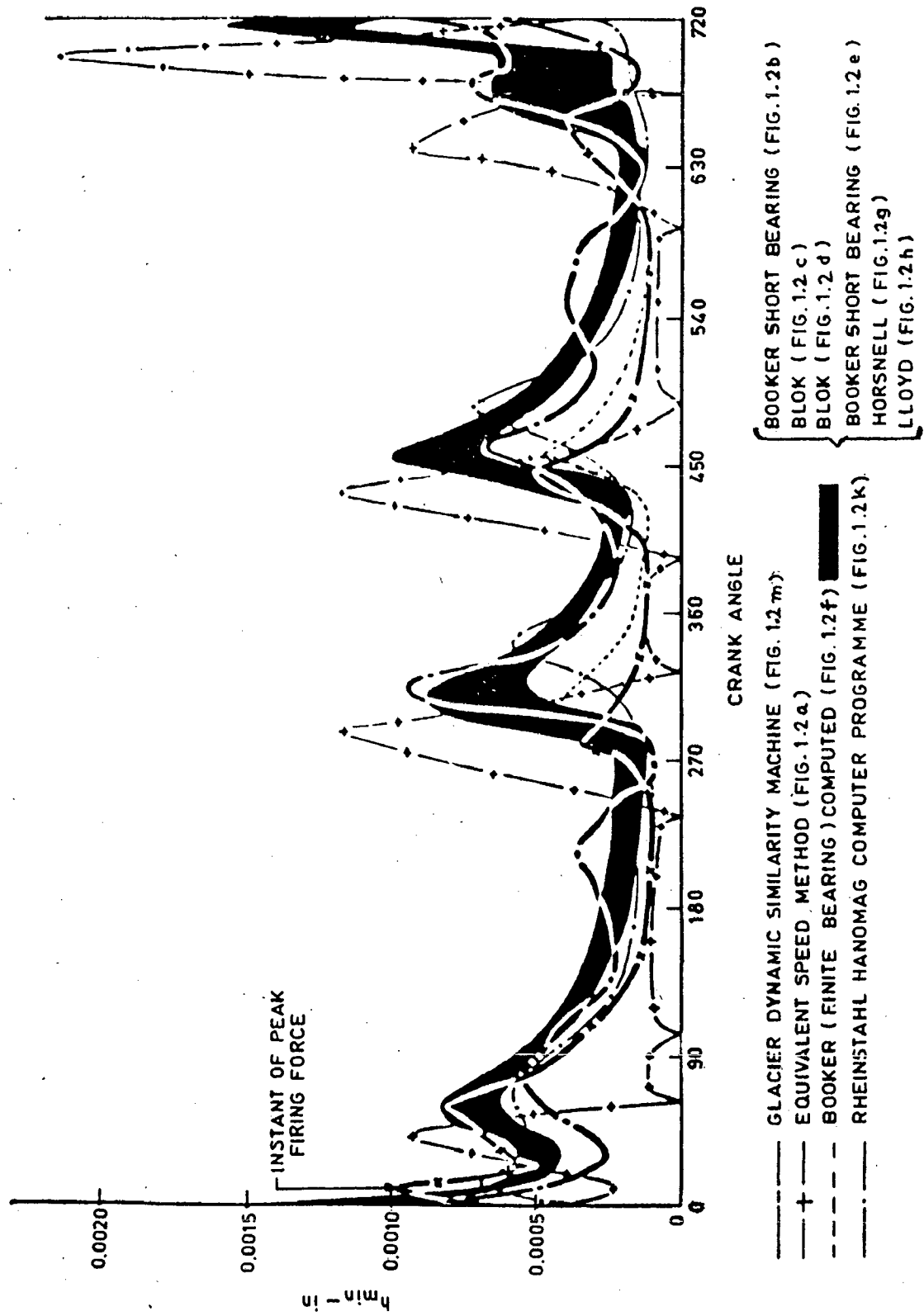


Fig.1.3. Minimum oil film thickness comparison (results from engine similarity machine and theoretical methods) [10]

and main bearings, directly using a running engine. He graphically showed, how the temperature varies from piston to main bearing and to the sump in a running diesel engine. In the case of big-end bearing, the results indicated that there was a very small variation in the temperature.

In 1968, Lloyd and McCallion [41] modified their computer program of Ref. [40] to accommodate the effect of groove or oil holes. They presented some curves to show the effect of half-groove (180°) and full-groove in the big-end bearing. For the bearing in the example, they found that the maximum eccentricity ratio reduced from 0.970 to 0.960 due to changing a full groove to half groove, but suggested that the temperature rise and the peak oil film pressure are likely to be substantially smaller in the case of the full-groove bearing.

Ross and Slaymaker [54] developed a computer program to analyze the bearings subjected to the dynamic loadings and used particularly for engine main, big-end, and small-end bearings. They used the short bearing approximation with an equivalent speed criteria. The positive pressure was assumed up to 180° of the circumference (π -film approximation). They studied three cases. The first case deals with an evaluation of the journal path within a bushing subjected to a constant, unidirectional load starting from an arbitrary position. The second case traces the path of crank pin in a 6 cylinder-in-line diesel engine and compares the minimum film thickness with experimental results. Finally, the third of these studies pertains to the paths taken by the crank pin and the journal of crank shaft in a V-8 diesel engine and relate them to the wear pattern observed in an associated bearing subjected to dynamometer

testing.

Dehart and Harwick [12] presented design considerations for the automotive engine bearings and emphasized the importance of the following factors in their design; size of bearing, load, speed, friction, oil flow, heat generated, and film thickness. There are many factors other than those normally considered in a purely analytical program which have enormous effects on the bearing performance. Some of the more important considerations are those of lubrication system, geometry, distortion and bearing material selection.

Booker [5] later developed a new approach to find the maximum film pressure in the oil film under dynamic loading. He suggested a conceptually simple method for calculating film pressure from journal orbit computation which is also applicable to the big-end bearing. In the paper, the data maps were presented for short bearings.

Wear and fatigue in a bearing are directly related to the film thickness and pressure in the lubricant film. Again by using the short bearing approximation and equivalent speed criteria, Ross [55] found how the film pressure varies with load rating, bearing angular coordinate, crank angle, shaft angle and the variation of minimum film thickness.

The graphical mobility method has been converted into a numerical approach [6] by Booker himself. He reviewed the mobility method and given details for its numerical handling, with an example of reciprocating machinery. For a 6 VEB-X Mk-III engine bearing, he computed that the maximum eccentricity ratio 0.960 (corresponding to the minimum film thickness of 130×10^{-6} in) occurs at 275° after

the top-dead-centre (TDC).

Direct measurement of bearing centre locus in the big-end bearing is a very tedious job. But a successful endeavour was made by Hiruma and Furuhamu [29] in their work. They developed a special new device to measure the film thickness or the bearing centre locus in the big-end bearing directly in the running condition of engine. By means of their technique using inductance transducers, the measurement could be made with stable results at 5000 rpm upto full load. They have presented various loci and concluded that (i) the crank pin centre makes a tour along the vicinity of the bearing surface due to the inertia force. In the combustion period, however, the crank pin centre passes near the centre point of bearing, (ii) increasing the speed and the oil temperature brings the locus of the pin closer to bearing surface, i.e., the minimum oil film thickness decreases.

During the late sixties, the finite element method also appeared in the lubrication field. In 1973, Shelly and Ettles [60] used the FEM technique for the calculation of locus paths in dynamically loaded bearings. In this approach, the special properties of an exponentially shaped element were used together with a satisfactory approximation for the axial pressure profile. This approach was claimed one hundred times faster than a conventional finite difference solution of equivalent accuracy. The predictor-corrector method, to march out a locus path were briefly outlined by Shelly and Ettles and several typical loci were presented as examples. The main problem encountered in the analysis was the unstable tendency for the high-order predictor-corrector

method in certain loading conditions, for example at the gas ignition point during the loading cycle of a big-end bearing.

Blok [7], using the mobility method, developed a different approach called Impulsive Method and claimed that this method carries integration one step farther than the mobility method and can be applied to the bearings under dynamically loading. No particular example was, however, solved by him.

Ritchie [56] used a semi-analytical method of predicting bearing centre loci in diesel engine bearings. A somewhat original feature of the method was the use of an approximate solution of the Reynolds equation which is similar to, but more accurate than, the short bearing solution.

Selection of materials for the bearings of high speed diesel engine is a difficult task. Bearing materials are selected on the basis of load carrying capacity, strength, temperature, coefficient of friction, dirt embeded ability, corrosion resistance and ability to accept misalignment. Unfortunately no one material possesses all the desirable properties and for this reason, the bimetal and trimetal bearings having steel back have been evolved. Davison [13], in his paper, outlined many such combinations of the bimetal and trimetal bearing having steel back. He claimed that the material 'A' (as designated in the paper) containing 14% to 20% lead, 4% to 6% tin and remainder copper have the rating 62.1 MN/m^2 (i.e., load 62.1 MN per unit area of the bearing) which is the highest among other materials 'B' and 'C'. He also explained the manufacturing method of these bearings.

Goodwin and Holmes [20,21] have also made a successful attempt to obtain the continuous monitoring of oil film thickness [20] and

temperature [21] in an engine bearing. The measurements of oil film thickness were successfully carried out using an inductive method. They presented the variation of minimum film thickness for plain model, half-grooved model, grooved-model bearing under full load, no load, no firing conditions at 750 rpm, 850 rpm and 920 rpm speed. The temperature measurements were made in a big-end bearing of marine diesel engine. For this bearing, they studied the effects of dilution of lubrication oil by fuel, effect of priming the lubrication system on the big-end bearing temperature distribution. No adverse effects were produced even by a short period of running with the oil diluted by 13% fuel. With regard to priming, their results suggested that when an engine was to be brought to full speed and put on load in a very short time after starting, priming was a very worthwhile safeguard even after a brief shut-down period.

Fantino et al [16,17] considered the deformation of the body of the big-end bearing to obtain the minimum film thickness. In the first paper [16], the elastic deformation and pressure distribution were obtained by iterative method in the steady state condition under realistic speeds and loads (5500 rpm, 25000N). Plane elasticity relations were used in the study. The effects of the following parameters were investigated; (i) bearing thickness (t_b) and bearing clearance (c), (ii) journal speed (N_j) and applied load (W), (iii) viscosity (μ_o) and piezoviscous coefficient (α_p).

It was found that as a result of the bearing body deformation, the maximum pressure and the attitude angle both decrease and the relative eccentricity greatly increased. An empirical dimensional equation for the minimum oil film thickness (h_m) was derived numerically for the bearing under study [16] and the expression of

the minimum film thickness was found as,

$$h_m \approx \left(\frac{\mu_0 N_{e-0.5}}{W} \right) (1 + 0.06 \times 10^8 \alpha_p) \left(\frac{t_n}{C^{0.09}} \right)^{0.12}$$

In the second paper [17], they verified their theoretical results by experiments. A speckle image of the rough surface of the big-end bearing was formed and recorded on a holographic plate both before and after the load was applied. This plate was then examined point by point in a diffractometer.

Generally, in heavy duty diesel engines trimetallic bearings are used. The bearing construction consists of lead-iridium overlay, copper-lead-tin bearing lining and a low carbon steel back. A nickel barrier is also plated between the overlay and the bearing lining to prevent tin diffusion from the overlay to the lining. When the big-end bearing overlay was examined of various field returned diesel trucks with the help of Scanning Electron Microscope (SEM), Patel [49] found a premature overlay removal of such bearings. He concluded that the oil balls, (discrete spherical particles) composed of oil additive elements, were the contributing factors to premature overlay removal.

After monitoring the temperature and film thickness in their previous work, Goodwin and Holmes [22] tried to measure the deformation of the housing and the temperature variation across the film. They presented the distorted clearance circles at 3000 rpm and also the temperature variations for different loadings. The maximum variation of temperature was of the order of 6°C-7°C for the majority of the load cases studied.

In 1983, a second review work on engine bearings was presented by Martin [45]. In this paper, some of the important recent developments in the engine bearings design techniques were highlighted. The availability of increased computing power has enabled considerations of more realistic assumptions regarding bearing behaviour; these include, among others, oil feed features, oil film history, non-circular bearings, improved prediction of main bearing load, flexible housing and special bearings. References to these advances are made in the review together with illustrations of how they affect the bearing performance. Experimental investigations were also presented which help to verify and give confidence to the analytical predictions. Ultimately, this paper [45] is useful to the designers and researchers of engine bearings.

The curve-fits [23] for journal bearing systems were used by Goenka and a set of analytical curve-fits were presented. The set includes the two components of mobility vectors, location and magnitude of the maximum film pressure, and the starting and finishing angles of the pressure curve. For an ideal journal bearing system, the curve-fits of Goenka [23] give results with an accuracy, comparable to that of an expensive finite element analysis. With the help of the curve fits for the case study of a big-end bearing, the minimum film thickness was calculated as $3.50 \mu\text{m}$ and the maximum film pressure as 34.57 MPa . It was concluded that the CPU time requirement was very small in comparison to that of FEM. But the curve-fit method is also only applicable to ideal bearings. Goenka [24], in his further work solved the same problem [23] with finite element method. An important feature of his analysis was relatively low computing cost. He solved an illustrative example with a total

of 17 different cases of a connecting-rod big-end bearing, 5 of ideal bearings, 6 of various groove/hole configurations and the remaining with different geometric variations of the bearings.

Fantino, Godet and Frene [18] have studied the dynamic behaviour of an elastic connecting-rod big-end bearing using an iterative method. Reynolds equation was solved using short bearing approximation and deformations in the bearing housing were obtained with plane elasticity relations. They calculated the locus of the bearing centre for the dynamic loading conditions of a big-end bearing. Instantaneous elastic deformations and pressure distributions were obtained for different values of the load.

Variation of the minimum film thickness, torque and flow rate with respect to crank rotation were compared with those obtained for a rigid bearing housing under the same dynamic conditions. Results show that with respect to the rigid bearing case, instantaneous radial and tangential deformations and also radial rates of deformation, (i) increase significantly the eccentricity ratio which can vary between 0.5 and 3.8 over two crank rotations, (ii) increase slightly the friction torque but significantly the axial flow, and (III) decrease the minimum film thickness by up to 15% only.

Fantino and Frene [19] used the earlier work [18] to compare the performance (minimum film thickness, torque and flow rate) of two different bearings of petrol and diesel engines. Their results show that of all the mechanical factors considered (load, speed, viscosity,...), the most significant was the load which together with the elastic deformation of bearing body governs the film thickness distribution. The results calculated for each respective load diagram and speed condition show that, (i) the eccentricity

ratio, which varies between 0.5 and 3.8 for the petrol engine, varies only between 0.6 and 1.0 in the diesel engine, (ii) torque increases slightly in both cases, (iii) flow increases significantly in the petrol engine but does not vary for the diesel engine, and (iv) the minimum film thickness decrease by 15% for the petrol engine and increases by 20% for diesel.

The difference between petrol and diesel engine bearings performance was attributed to the difference in their load diagrams and particularly to the fact that the very high loads obtained with the diesel occur only over a short arc situated on both sides of the connecting-rod axis where under compression the connecting-rod is a very rigid structure.

Oh and Goenka [47] also studied the elastohydrodynamic (EHD) lubrication of journal bearings under dynamic loadings. The Newton-Raphson algorithm was used in conjunction with Murty's algorithm [46] and the finite element method to analyze the EHD lubrication of a journal bearing system under dynamic loading condition including cavitation boundary conditions to establish the positive pressure zone. Solution for the film pressure, the film thickness and its rate of change with time were obtained as functions of the crank angles.

A numerical method was proposed by Tempel, Moes and Bosma [64,65] in their recent study for calculating the film thickness in flexible short journal bearings under dynamic loading. The system of elastohydrodynamic integro-differential equations were discretized directly and solved by a two step Newton-Raphson method. The results for the big-end bearings of medium and high-speed combustion engines were compared. In their second paper [65], a starvation model was

incorporated to their previous work [64]. The system of EHD integro-differential equations were coupled with continuity equation for the lubricants, considering central circumferential oil grooves and a constant supply pressure. Results for several groove geometries were compared with those for a fully flooded bearing.

LaBouff and Booker [42] studied the 6VEB-X engine bearing including elastic deformation of the bearing body. Due to a large requirement of computer time, the results were obtained only for a finite crank rotations. The minimization of the functional was used for hydrodynamic solution and a two dimensional model for deformation computation.

The literature indicates a considerable scope for further studies on the big-end bearings considering such aspects as pressure and temperature dependence of viscosity, non-Newtonian characteristics of lubricants, misalignment between the crank pin and the bearing, and deformation of the bearing body. This thesis presents the solutions of the following problems of a big-end bearing.

1. Rigid bearing with isoviscous lubricants,
2. Rigid bearing with piezoviscous lubricants,
3. Rigid bearing with lubricants having viscosity variation due to pressure and temperature, both (piezo-thermal effects),
4. Rigid bearing with non-Newtonian lubricants,
5. Ungrooved bearing with parallel and skewed axes,
6. Elastothermohydrodynamic (ETHD) effects (i.e., solution of bearing considering the flexibility of the bearing body and viscosity variations with temperature and pressure, both).

A general solution procedure evolved in a modular form and

briefly outlined here, is used to solve all the six problems. The clearance space between the bearing and the crank pin is discretized into a mesh of $12 \times 4 \times 1$ three dimensional isoparametric elements, each containing 20 nodes. Full Sommerfeld boundary condition is used to solve the Navier-Stokes equations which are used in the analysis, instead of the traditional Reynolds equation, to account for the variation of viscosity. The cavitation effect is accounted by replacing the negative values of nodal pressure by zero values. At each crank angle interval, the pressure and velocity fields are established by solving the momentum and continuity equations in cylindrical coordinates. The finite element formulation is based on Galerkin's method and a direct iterative technique is used for the solution of global system equations. The boundary conditions are introduced at the element stage to minimize the computer storage requirements. The global system equations are solved for the columns of the right hand side simultaneously to evaluate the pressure fields due to wedge, squeeze and whirling actions of the fluid-film. For the time marching scheme, Euler-Cauchy's predictor-corrector method is employed which is found more stable and computationally economical in comparison to Runge-Kutta or any higher-order predictor-corrector methods for this problem. An emphasis is given to calculate the time history of the bearing centre with respect to the crank pin centre for one duty cycle, hereafter called as bearing centre orbit.

To obtain the bearing centre orbit for a rigid bearing with isoviscous lubricants, the solution is started from an arbitrarily selected crank angle 110° with suitable time steps.

The solution is continued even beyond two revolutions (720°)

unless the orbit repeated itself. In this case the computed minimum film thickness in the orbit is very close to the reported values [10] which supports the validity of the algorithm.

A circumferential groove to supply the lubricant in the bearing is considered as a typical example, Fig.1.4. This groove is accounted in the analysis by considering the resulting symmetry and solving for only one land of the bearing which shares half of the load on the bearing. The pressure in the groove is taken as ambient pressure. Grooves in the bearings significantly alter the peak film pressure. Fig.1.5 shows the effects of introducing a groove into a bearing while maintaining the same projected area. The variations of the maximum film pressure and the minimum film thickness are also presented as a function of crank angle in the results.

In the case of rigid bearing with piezoviscous lubricant, the viscosity is modified using the pressure viscosity relation ($\mu = e^{\alpha_p p}$) where α_p is the piezoviscous coefficient and p is the fluid-film pressure. Using this relation with a suitable value of α_p , the results (bearing centre orbit, the minimum film thickness, the maximum pressure, and the power loss) are calculated. A comparison of these results is also made with those of isoviscous case.

It is a well known fact that the viscosity of lubricant is sensitive to temperature variations. Although according to the experimental data available, the temperature rise in connecting-rod big-end bearings is not high (only of the order of 10° to 25° C), this rise of temperature reduces the viscosity of lubricants enough to affect the performance of the bearing. The literature on the

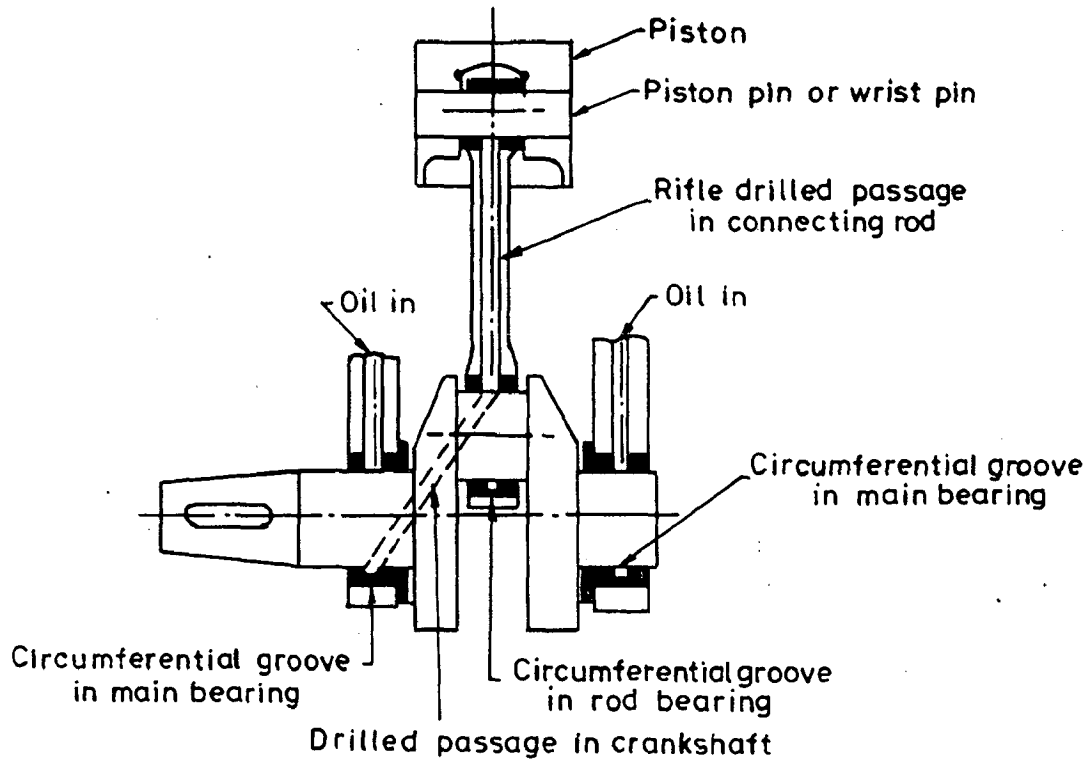


Fig.1-4 Oil passages for lubrication of engine bearings

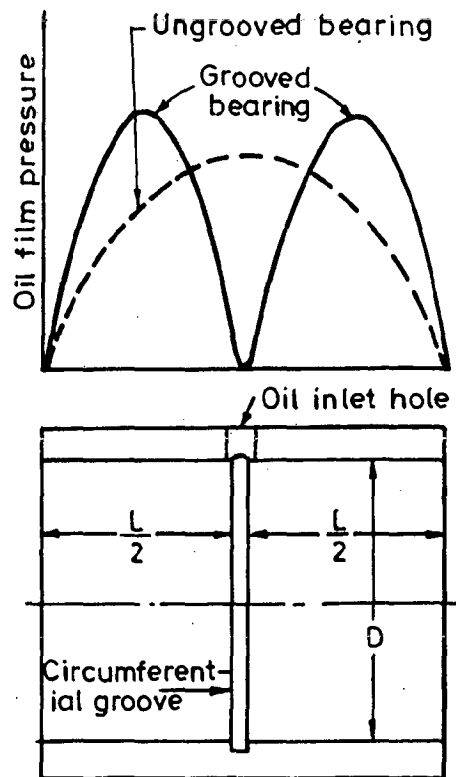


Fig.1-5 Circumferential grooved bearing showing effect on pressure distribution

solution of the big-end bearing with lubricants having variable viscosity is scant. A truly general and realistic solution of the connecting-rod big-end bearing problem should include piezo-thermal effects. These effects are included in this thesis for both , for rigid bearing and for flexible bearing. For a rigid bearing with piezo-thermal effects , the bearing centre orbit, the minimum film thickness, the maximum peak pressure, the maximum temperature rise and the power loss are calculated.

For the rigid bearing, the effect of non-Newtonian behaviour of lubricants is also studied. In the case of non-Newtonian lubricants, the relation between shear stress (Γ) and shear strain rate (Υ) is non-linear. For example, Hsu and Saibel [30] expressed shear strain rate in terms of powers of shear stress ($\Gamma + k \Gamma^3 = \Upsilon$) for the analysis of infinite width slider bearings. This relation was claimed to be more representative over a wide range of shear rate. There are several other models available for non-Newtonian behaviour of the lubricants. In the algorithm used by the author, any non-Newtonian model [35] can be accommodated, but in this thesis, bearing centre orbit is calculated using the cubic shear stress law model stress law model ($\bar{\Gamma} + k\bar{\Gamma}^3 = \bar{\Upsilon}$) by taking a suitable value of constant K . The square root of the second invariant of shear strain tensor is taken in place of Υ and the corresponding equivalent shear stress (Γ) is calculated using Newton-Raphson method. The apparent viscosity at each Gaussian integration point is calculated as $\mu_a = (\Gamma / \Upsilon)$ and the solution is upgraded using these apparent viscosities in each iteration. The variations of the minimum film thickness and the maximum film pressure as a function of crank angle are found and compared with those of the Newtonian lubricant case.

The bearing centre locus, values of the minimum film thickness, and the maximum film pressure are also obtained at 10° interval for a finite crank rotation using the curve-fit model. In this model, a fourth degree polynomial is fitted, using the least square method, on the available experimental data of μ_a and γ for a non-Newtonian oil. By using the computed velocity field in the bearing at each crank angle, the values of strain rate ($\dot{\gamma}$) are calculated at each Gaussian point and by introducing these values in the polynomial expression (non-dimensional form), the values of apparent viscosity ($\bar{\mu}_a$) are calculated and the solution is then upgraded in an iterative manner. The results obtained by the curve-fit model and by cubic shear stress law model are found to be almost identical.

The big-end bearing in the example has a circumferential groove inside. This bearing is also studied assuming it to be without groove for the cases of parallel and skewed axes. In both the cases, the bearing centre orbits, the variations of the minimum film thickness and the maximum film pressure as a function of crank angle are calculated.

It is established that in a heavily loaded bearing, the fluid-film pressure deforms the bearing liner significantly even when the outer surface of the bearing liner is encased in a fixed housing. It has been observed that the big-end bearing behaves as a flexible bearing and its elastic distortion due to hydrodynamic pressure is often larger than the nominal radial clearance. This deformation changes the film geometry and in turn the performance characteristics of the big-end bearing significantly. In this thesis, the work is extended to study the effect of ETHD. In the ETHD case, to start with, the pressure and velocity fields are obtained considering the

bearing as rigid and the lubricant as isoviscous. Using the 8 noded isoparametric elements and elasticity relations, the nodal displacement components at inner and outer surfaces of the bearing body are obtained. The nodes on that portion of the bearing body which is integrated with the connecting-rod are considered as fixed. The radial displacement components dominate the displacement field, therefore, the other two components (axial and circumferential) are neglected. The fluid-film thickness is then modified by adding algebraically the radial displacement components to the corresponding radial coordinates of the nodes which lie at the inner surface of the bearing body. Using the computed velocity field, the energy equation is solved to obtain the temperature field. The relation $\mu_a = e^{(\alpha_p p - \beta_T (T-1))}$ is used to calculate the values of apparent viscosity at Gaussian points. Using these upgraded values of viscosity and the modified film geometry due to deformation, the modified pressure field is obtained which yields the fluid-film force components. These modified film force components are substituted in the time marching scheme, and the bearing centre orbit points are then obtained. A large computation time is required for convergence at each time interval, therefore, the ETHE effect on the bearing performance is studied for only a finite crank rotation using 20 interval.

The algorithm evolved in this work is quite general and can be implemented for the solution of connecting-rod big-end bearing with isoviscous/piezoviscous/non-Newtonian lubricants. It can be used to study the effects of elastothermohydrodynamic lubrication and piezo-thermal viscosity behaviour of lubricants on the performance of the big-end bearing. The computer program can also handle the solution of

big-end bearing without groove and with misalignment of the axes. From the results obtained for the rigid bearing cases, it can be concluded that non-Newtonian and piezo-thermal effects yield smaller value of the minimum film thickness in comparison to that in the isoviscous case. The piezoviscous effect slightly improves the value of the minimum film thickness. In the case of the ungrooved bearing with parallel axes, the minimum film thickness is appreciably larger in comparison to that in the grooved bearing. The effect of misalignment is also noticeable in the ungrooved big-end bearing.

For accurate analysis and design it would be necessary to consider EHD effects, it, however, requires a large CPU time. From a practical point of view, therefore, one may analyze or design the connecting-rod big-end bearing considering it as a rigid bearing with non-Newtonian lubricants or the lubricants having piezo-thermal viscosity characteristics.

CHAPTER 2

FLOW-FIELD

The flow-field description in the clearance space of a journal bearing, when expressed by Reynolds equation, implies several assumptions. In addition to the assumption of negligible body and fluid inertia forces, Reynolds equation assumes that the viscosity of the fluid in the clearance space is also constant which is not always true. It is difficult to accommodate the variation of viscosity across the film thickness whether due to piezoviscous effect, non-Newtonian fluid characteristics and or by thermal effect in the analysis through Reynolds equation. Therefore, in this analysis, the momentum and continuity equations in the cylindrical coordinates, which conform to the actual geometry of the fluid-film profile in the clearance space of a journal bearing, are solved numerically by finite element method using Galerkin's technique and the variation of viscosity is incorporated by upgrading the solution vector iteratively.

2.1.1 Navier-Stokes Equations (cylindrical coordinates)

The nondimensional momentum equations in cylindrical coordinates governing the flow-field in the clearance space of a finite journal bearing are given as

$$\text{Re} \left[\frac{D\bar{u}}{D\bar{t}} + \frac{\bar{u}\bar{v}}{\bar{r}} \right] + \frac{\bar{R}}{\bar{r}} \frac{\delta\bar{p}}{\delta\theta} = \bar{\mu}_a \left[\nabla^2 \bar{u} + \frac{2}{\bar{r}^2} \frac{\delta\bar{v}}{\delta\theta} - \frac{\bar{u}}{\bar{r}^2} \right] \quad (2.1a)$$

$$\text{Re} \left[\frac{D\bar{v}}{D\bar{t}} + \frac{\bar{u}^2}{\bar{r}} \right] + \bar{R} \frac{\delta\bar{p}}{\delta\bar{r}} = \bar{\mu}_a \left[\nabla^2 \bar{v} - \frac{2}{\bar{r}^2} \frac{\delta\bar{u}}{\delta\theta} - \frac{\bar{v}}{\bar{r}^2} \right] \quad (2.1b)$$

$$\text{Re} \left[\frac{D\bar{w}}{D\bar{t}} \right] + \frac{\delta\bar{p}}{\delta\bar{z}} = \bar{\mu}_a \left[\nabla^2 \bar{w} \right] \quad (2.1c)$$

where,

$$\frac{D}{D\bar{t}} = \left(\frac{1}{\bar{R}} \frac{\delta}{\delta\bar{t}} + \frac{\bar{u}}{\bar{r}} \frac{\delta}{\delta\theta} + \bar{v} \frac{\delta}{\delta\bar{r}} + \frac{\bar{w}}{\bar{R}} \frac{\delta}{\delta\bar{z}} \right)$$

and

$$\nabla^2 = \left(\frac{\delta^2}{\delta\bar{r}^2} + \frac{1}{\bar{r}} \frac{\delta}{\delta\bar{r}} + \frac{1}{\bar{r}^2} \frac{\delta^2}{\delta\theta^2} + \frac{1}{\bar{R}^2} \frac{\delta^2}{\delta\bar{z}^2} \right)$$

In the present analysis, the fluid inertia is not included. So, neglecting the terms representing the local and convective fluid inertia, Eqs.(2.1a-2.1c) reduce to

$$\frac{\bar{R}}{\bar{r}} \frac{\delta\bar{p}}{\delta\theta} = \bar{\mu}_m \left[\nabla^2 \bar{u} + \frac{2}{\bar{r}^2} \frac{\delta\bar{v}}{\delta\theta} - \frac{\bar{u}}{\bar{r}^2} \right] \quad (2.2a)$$

$$\bar{R} \frac{\delta\bar{p}}{\delta\bar{r}} = \bar{\mu}_m \left[\nabla^2 \bar{v} - \frac{2}{\bar{r}^2} \frac{\delta\bar{u}}{\delta\theta} - \frac{\bar{v}}{\bar{r}^2} \right] \quad (2.2b)$$

$$\frac{\delta\bar{p}}{\delta\bar{z}} = \bar{\mu}_m \left[\nabla^2 \bar{w} \right] \quad (2.2c)$$

2.1.2 Continuity Equation:

The continuity equation for a source free control volume is

$$\frac{\delta\bar{\theta}}{\delta\bar{t}} + \frac{1}{\bar{r}} \frac{\delta(\bar{\theta}\bar{u})}{\delta\theta} + \frac{\delta(\bar{\theta}\bar{v})}{\delta\bar{r}} + \frac{\bar{\theta}\bar{v}}{\bar{r}} + \frac{1}{\bar{R}} \frac{\delta(\bar{\theta}\bar{w})}{\delta\bar{z}} = 0 \quad (2.3)$$

If the fluid is homogenous and incompressible, as in the case of lubricants, the density is constant which simplifies Eq.(2.3) to,

$$\frac{1}{\bar{r}} \frac{\delta\bar{u}}{\delta\theta} + \left(\frac{\delta\bar{v}}{\delta\bar{r}} + \frac{\bar{v}}{\bar{r}} \right) + \frac{1}{\bar{R}} \frac{\delta\bar{w}}{\delta\bar{z}} = 0 \quad (2.4)$$

2.2 BOUNDARY CONDITIONS:

The boundary conditions which can be applied to the flow-field are either in terms of pressure or in terms of velocity components. For the bearing, used as an example [10], there is a circumferential groove all around in the middle of the inner surface of the bearing ,

hence, the following boundary conditions are applied at the element equation stage to minimize the computer storage required for the global fluidity matrix.

$$\bar{p}(\theta, \bar{z}) = 0 \quad \text{at} \quad \bar{z} = \pm \bar{B} \quad (2.5a)$$

$$\bar{u} = \left(1 + \frac{1}{\bar{R}}\right) \left(1 + \frac{\cos\theta_1}{\sqrt{q^2 - \sin^2\theta_1}}\right) - \frac{\dot{\epsilon}}{\bar{R}} \sin\theta + \frac{\dot{\epsilon}\beta}{\bar{R}} \cos\theta, \quad \bar{r} = \bar{R} + \bar{h} \quad (2.5b)$$

$$\bar{v} = (\dot{\epsilon} / \bar{R}) \cos\theta + (\dot{\epsilon}\beta / \bar{R}) \sin\theta, \quad \bar{r} = \bar{R} + \bar{h} \quad (2.5c)$$

$$\bar{w} = 0, \quad \bar{r} = \bar{R}, \quad (\bar{R} + \bar{h}) \quad (2.5d)$$

$$\bar{u} = 0, \quad \bar{r} = \bar{R} \quad (2.5e)$$

$$\bar{v} = 0, \quad \bar{r} = \bar{R} \quad (2.5f)$$

where, $\bar{h} = 1 + \epsilon \cos\theta$.

2.3 FINITE ELEMENT FORMULATION:

The complete circumference of the bearing is divided into 48 isoparametric elements. The discretization has been done by twelve divisions circumferentially, four axially. In the circumferential direction the grid is non-uniform, having finer spacings in the zone of maximum pressure. In each element, velocity components are approximated by a quadratic variation (20-nodes) and the pressure by a linear variation (8-nodes). This mixed type of formulation is favoured by Zienkiewicz [69] and other [33].

Applying the orthogonality condition of Galerkin's finite element method [33,69] to the momentum (Eqs.(2.2a)-(2.2c)) and continuity (Eq.2.4) equations, the following equations are obtained for an element in the clearance space of a journal bearing system.

$$\iiint_e N_i \left[\frac{\bar{R}}{r} \frac{\delta \bar{p}}{\delta \theta} - \bar{\mu}_m (\sqrt{z} \bar{u}) + \frac{2}{r^2} \frac{\delta \bar{v}}{\delta \theta} - \frac{\bar{u}}{r^2} \frac{\bar{r}}{\bar{R}} \right] \frac{r}{\bar{R}} d\theta dr dz = 0 \quad (2.6a)$$

$$\iiint_e N_i \left[\frac{\bar{R}}{r} \frac{\delta \bar{p}}{\delta r} - \bar{\mu}_m (\sqrt{z} \bar{v}) - \frac{2}{r^2} \frac{\delta \bar{u}}{\delta \theta} - \frac{\bar{v}}{r^2} \frac{\bar{r}}{\bar{R}} \right] \frac{r}{\bar{R}} d\theta dr dz = 0 \quad (2.6b)$$

$$\iiint_e N_i \left[\frac{\delta \bar{p}}{\delta z} - \bar{\mu}_m (\sqrt{z} \bar{w}) \right] \frac{r}{\bar{R}} d\theta dr dz = 0 \quad (2.6c)$$

$$\iiint_e M_j \left[\frac{1}{r} \frac{\delta \bar{u}}{\delta \theta} + \frac{\bar{v}}{r} + \frac{\delta \bar{v}}{\delta r} + \frac{1}{\bar{R}} \frac{\delta \bar{w}}{\delta z} \right] \frac{r}{\bar{R}} d\theta dr dz = 0 \quad (2.6d)$$

where $i = 1, \dots, 20$ velocity nodes,

$j = 1, \dots, 8$ pressure nodes,

and

$$\bar{u} = \sum_{i=1}^{20} N_i \bar{u}_i, \quad \bar{v} = \sum_{i=1}^{20} N_i \bar{v}_i, \quad \bar{w} = \sum_{i=1}^{20} N_i \bar{w}_i, \quad \bar{p} = \sum_{j=1}^8 M_j \bar{p}_j.$$

The shape functions for velocities ($N_i, i=1,2,3,\dots,20$) and pressures ($M_j, j=1,2,3,\dots,8$), in terms of local coordinates (ξ, η, ζ), are given below.

For corner nodes,

$$N_i = \frac{1}{8} (1 + \xi_0) (1 + \eta_0) (1 + \zeta_0) (\xi_0 + \eta_0 + \zeta_0 - 2) \quad (2.7)$$

For mid sides nodes ($\xi_i = 0$),

$$N_i = \frac{1}{4} (1 - \xi^2) (1 + \eta_0) (1 + \zeta_0) \quad (2.8)$$

For mid sides nodes ($\eta_i = 0$),

$$N_i = \frac{1}{4} (1 + \xi_0) (1 - \eta^2) (1 + \zeta_0) \quad (2.9)$$

For mid sides nodes ($\zeta_i = 0$)

$$N_i = \frac{1}{4} (1 + \xi_0) (1 + \eta_0) (1 - \zeta^2) \quad (2.10)$$

$$= \iiint \bar{\mu}_m \left[-\frac{2}{\bar{r}^2} N_1 \frac{\delta N_3}{\delta \theta} \frac{\bar{r}}{\bar{R}} \right] d\theta d\bar{r} d\bar{z}$$

$$\text{for } m = 1, 4, 7, \dots, 58; i = (m+2)/3 \text{ so } i = 1, \dots, 20$$

$$n = 2, 5, 8, \dots, 59; j = (n+1)/3 \quad j = 1, \dots, 20$$

$$= 0$$

$$\text{for } m = 1, 4, 7, \dots, 58; i = (m+2)/3 \text{ so } i = 1, \dots, 20$$

$$n = 3, 6, 9, \dots, 60; j = n/3 \quad j = 1, \dots, 20$$

$$m = 3, 6, 9, \dots, 60; i = m/3 \text{ so } i = 1, \dots, 20$$

$$n = 1, 4, 7, \dots, 58; j = (n+2)/3 \quad j = 1, \dots, 20$$

$$= \iiint_e [\bar{\mu}_m \frac{2N_1}{\bar{r}^2} \frac{\delta N_3}{\delta \theta} \frac{\bar{r}}{\bar{R}}] d\theta d\bar{r} d\bar{z}$$

$$\text{for } m = 2, 5, 8, \dots, 59; i = (m+1)/3 \text{ so } i = 1, \dots, 20$$

$$n = 1, 4, 5, \dots, 58; j = (n+2)/3 \quad j = 1, \dots, 20$$

$$= \iiint_e \bar{\mu}_m \left[\frac{\delta N_1}{\delta \bar{r}} \frac{\delta N_3}{\delta \bar{r}} - \frac{N_1}{\bar{r}} \frac{\delta N_3}{\bar{r}} + \frac{1}{\bar{r}^2} \frac{\delta N_1}{\delta \theta} \frac{\delta N_3}{\delta \theta} + \frac{1}{\bar{R}^2} \frac{\delta N_1}{\delta \bar{z}} \frac{\bar{r}}{\bar{R}} \right] d\theta d\bar{r} d\bar{z}$$

$$\text{for } m = n = 3, 6, 9, \dots, 60; i = m/3 \text{ so } i = 1, \dots, 20$$

$$j = n/3 \quad j = 1, \dots, 20$$

$$\bar{K}_P = \iiint_{mn} \left[-\frac{\bar{R}}{\bar{r}} \frac{\delta N_1}{\delta \theta} M_3 \right] \frac{\bar{r}}{\bar{R}} d\theta d\bar{r} d\bar{z}$$

$$\text{for } m = 1, 4, 7, \dots, 58; i = (m+2)/3 \text{ so } i = 1, \dots, 20$$

$$n = 61, 62, \dots, 68; j = (n-60) \quad j = 1, \dots, 8$$

$$= \iiint_e \left[-\bar{R} \frac{\delta N_1}{\delta \bar{r}} M_3 \right] \frac{\bar{r}}{\bar{R}} d\theta d\bar{r} d\bar{z}$$

for $m = 2, 5, 8, \dots, 59$; $i = (m+1)/3$ so $i = 1, \dots, 20$

$n = 61, 62, \dots, 68$; $j = (n-60)$ $j = 1, \dots, 8$

$$= \iiint_e \left[- \frac{\delta N_1}{\delta \bar{z}} M_3 \right] \frac{\bar{r}}{\bar{R}} d\theta d\bar{r} d\bar{z}$$

for $m = 3, 6, 9, \dots, 60$; $i = m/3$ so $i = 1, \dots, 20$

$n = 61, 62, \dots, 68$; $j = (n-60)$ $j = 1, \dots, 8$

$$\bar{K}'^{\mathcal{P}} = \iiint_{mn} \frac{1}{e} \left[\frac{\delta N_1}{\bar{r} \delta \theta} M_3 \right] \frac{\bar{r}}{\bar{R}} d\theta d\bar{r} d\bar{z}$$

for $m = 61, 62, \dots, 68$; $j = (m-60)$ so $j = 1, \dots, 8$

$n = 1, 4, 7, \dots, 58$; $i = (n+2)/3$ $i = 1, \dots, 20$

$$= \iiint_e \left[\frac{\delta N_1}{\delta \bar{r}} M_3 + \frac{N_1}{\bar{r}} M_3 \right] \frac{\bar{r}}{\bar{R}} d\theta d\bar{r} d\bar{z}$$

for $m = 61, 62, \dots, 68$; $j = (m-60)$ so $j = 1, \dots, 8$

$n = 2, 5, 8, \dots, 59$; $i = (n+1)/3$ $i = 1, \dots, 20$

$$= \iiint_e \left[\frac{1}{\bar{R}} \frac{\delta N_1}{\delta \bar{z}} M_3 \right] \frac{\bar{r}}{\bar{R}} d\theta d\bar{r} d\bar{z}$$

for $m = 61, 62, \dots, 68$; $j = (m-60)$ so $j = 1, \dots, 8$

$n = 3, 6, 9, \dots, 60$; $i = n/3$ $i = 1, \dots, 20$

The derivatives $\frac{\delta N_1}{\delta \theta}$, $\frac{\delta N_1}{\delta \bar{r}}$, and $\frac{\delta N_1}{\delta \bar{z}}$ used for defining the

coefficients of submatrices (\bar{K}^u) , $(\bar{K}^{\mathcal{P}})$ and $(\bar{K}'^{\mathcal{P}})$, are obtained from the

derivatives $\frac{\delta N_1}{\delta \xi}$, $\frac{\delta N_1}{\delta \gamma}$, and $\frac{\delta N_1}{\delta \zeta}$ using the following transformation

[69].

$$\begin{bmatrix} \frac{\delta N_1}{\delta \theta} \\ \frac{\delta N_1}{\delta \bar{r}} \\ \frac{\delta N_1}{\delta \bar{z}} \end{bmatrix} = [J]^{-1} \begin{bmatrix} \frac{\delta N_1}{\delta \xi} \\ \frac{\delta N_1}{\delta \gamma} \\ \frac{\delta N_1}{\delta \zeta} \end{bmatrix} \quad (2.13)$$

where, [J] is a Jacobian matrix and is defined [69] as

$$[J] = \begin{bmatrix} \frac{\delta\theta}{\delta\xi} & \frac{\delta\bar{r}}{\delta\xi} & \frac{\delta\bar{z}}{\delta\xi} \\ \frac{\delta\theta}{\delta\eta} & \frac{\delta\bar{r}}{\delta\eta} & \frac{\delta\bar{z}}{\delta\eta} \\ \frac{\delta\theta}{\delta\zeta} & \frac{\delta\bar{r}}{\delta\zeta} & \frac{\delta\bar{z}}{\delta\zeta} \end{bmatrix} \quad (2.14)$$

To transform the variables to define the integrals in terms of curvilinear coordinates, the following relations are used [69].

$$d\theta \, d\bar{r} \, d\bar{z} = |J| \, d\xi \, d\eta \, d\zeta \quad (2.15a)$$

$$\iiint_e \frac{\bar{r}}{\bar{R}} \, d\theta \, d\bar{r} \, d\bar{z} = \int_{-1}^{+1} \int_{-1}^{+1} \int_{-1}^{+1} \frac{\bar{r}}{\bar{R}} |J| \, d\xi \, d\eta \, d\zeta \quad (2.15b)$$

After the element equations (2.12) are modified for the boundary conditions (Eqs.(2.5a)-(2.5f)), the element contributions are assembled as usual for all the elements of the flow-field and the following global system equation is obtained:

$$[\bar{K}] \{\bar{\theta}\} = \{\bar{R}_A\} + \bar{\epsilon} \{\bar{R}_S\} + \bar{\beta} \{\bar{R}_W\} \quad (2.16)$$

2.4 NON-NEWTONIAN LUBRICANT MODEL-ANALYSIS

Engine bearings are recognized to be of major importance in relation to the overall engine performance. The specific engine performance factors and associated variables are wear, oil consumption, fuel economy, hot starting, cold starting, noise and shear stability. The bearing performance depends on the oil used for lubrication. Engine oils are defined by both a viscosity classification system (SAE J300C) and by a test performance and service classification (SAE J183a) [37]. Bearings are believed to operate under hydrodynamic mixed and or boundary lubrication regimes. The performance of bearings in hydrodynamic lubrication regimes

depends on the viscosity of the oil used. For most of the oils, measurements of shear stress and shear rate (at various magnitudes of both) indicate a linear relationship between the two. However, this simple relationship becomes complicated when mixed lubrication, boundary lubrication, pressure viscosity effects, shock loading and high shear rate effects are combined with engine oils modified by viscosity index (VI) improver additives. The polymer additives, in addition make the thickened oil non-Newtonian in shear behaviour. Many complex non-Newtonian fluids are not purely viscous (especially polymeric fluids used for engine lubrication). However, measurements of shear stress and shear rate may be made for these materials in steady shearing flows, and the ratio of these quantities may be defined as rheological characteristic. Since this ratio is not constant (as in the case of Newtonian fluids), it defines a function which is called the apparent viscosity (μ_a).

2.4.1 NON-NEWTONIAN LUBRICANT MODELS:

The non-Newtonian fluids may be classified in terms of the variation of apparent viscosity (μ_a) with shear stress (Γ) or shear rate ($\dot{\gamma}$). The most successful attempts at describing the steady shear stress-shear rate behaviour of non-Newtonian fluids are largely empirical. The following represents some of the more common empirical models in non-dimensional form [35].

1. Cubic shear stress law model

$$\bar{\Gamma} + K\bar{\Gamma}^3 = \dot{\bar{\gamma}} \quad (2.17a)$$

where, K is a non-linear factor

2. Power law model

$$\bar{\Gamma} = C_1 \dot{\bar{\gamma}}^{C_2} \quad (2.17b)$$

3. Prandtl model

$$\bar{\Gamma} = C_1 \sin^{-1} (\dot{\bar{\gamma}}/C_2) \quad (2.17c)$$

4. Eyring model

$$\bar{\Gamma} = \dot{\bar{\gamma}}/C_1 + C_2 \sin (\bar{\Gamma}/C_3) \quad (2.17d)$$

5. Power-Eyring model

$$\bar{\Gamma} = C_1 \dot{\bar{\gamma}} + C_2 \sinh^{-1} (C_3 \dot{\bar{\gamma}}) \quad (2.17e)$$

6. Williamson model

$$\bar{\Gamma} = \left[\frac{C_1}{C_2 + \dot{\bar{\gamma}}} + \bar{\mu}_\infty \right] \dot{\bar{\gamma}} \quad (2.17f)$$

7. Reinier-Philippoff model

$$\dot{\bar{\gamma}} = \frac{\bar{\Gamma} (1 + C_1 \bar{\Gamma}^2)}{1 + C_2 C_1 \bar{\Gamma}^2} \quad (2.17g)$$

where, C_1 , C_2 , and C_3 are the constants (Eqs.(2.17b)-(2.17g)) and $\bar{\mu}_\infty$ (Eq.2.17f) is the viscosity at infinite shear strain rate. In Eqs.(2.17a-2.17g), $\dot{\bar{\gamma}}$ is made independent of the shear strain rate for three dimensional (θ, r, z) flow and is given by [14].

$$\begin{aligned} \dot{\bar{\gamma}} = & \left[2 \left\{ \left(\frac{\delta \bar{v}}{\delta \bar{r}} \right)^2 + \left(\frac{1}{\bar{r}} \frac{\delta \bar{u}}{\delta \theta} + \frac{\bar{v}}{\bar{r}} \right)^2 + \left(\frac{1}{\bar{R}} \frac{\delta \bar{w}}{\delta \bar{z}} \right)^2 \right\} + \left\{ \frac{\delta \bar{u}}{\delta \bar{r}} - \frac{\bar{u}}{\bar{r}} + \frac{1}{\bar{r}} \frac{\delta \bar{v}}{\delta \theta} \right\}^2 \right. \\ & \left. + \left\{ \frac{1}{\bar{r}} \frac{\delta \bar{w}}{\delta \theta} + \frac{1}{\bar{R}} \frac{\delta \bar{u}}{\delta \bar{z}} \right\}^2 + \left\{ \frac{1}{\bar{R}} \frac{\delta \bar{v}}{\delta \bar{z}} + \frac{\delta \bar{w}}{\delta \bar{r}} \right\}^2 \right]^{1/2} \quad (2.18) \end{aligned}$$

The above expression (Eq.2.18) is written in non-dimensional form using the usual normalizing factors. For the value of $\dot{\bar{\gamma}}$ calculated from Eq.2.18 at every Gaussian intergration point, $\bar{\Gamma}$ can be calculated using any model (Eq.2.17a-2.17g), with the help of Newton-Raphson method. The apparent viscosity ($\bar{\mu}_a$) in non-dimensional form is then defined as

$$\bar{\mu}_a = \bar{\tau} / \dot{\gamma} \quad (2.19)$$

All the models (Eqs.2.17a-2.17g) are not applicable to the oils which are generally used for the lubrication of bearings. In this dissertation, the general relation (i.e., the pseudoplastic behaviour) which is represented by cubic shear stress law (Eq.2.17a) and is applicable to most of the practical engine oil lubricants [66], is used to obtain the bearing centre orbit. The algorithm used for this purpose is quite general and can be used for any non-Newtonian lubricant models (Eqs.2.17a-2.17g).

2.4.2 Non-Newtonian Model Using Curve Fit (Curve-Fit-Model)

The empirical models described in Section (2.4.1) for non-Newtonian fluid are hypothetical models. In real practice, the oil apparent viscosity, which varies with temperature and shear rate, can only be found out by actual measurements. These measurements have been made by, among others, Johnson and O'Shaughnessy [37] in their extensive experimental work and the apparent viscosity (μ_a) at different temperatures ($^{\circ}\text{F}$) 100, 150, 210, 280 and 320 and at shear rate (sec^{-1}) low, 2.5×10^5 , 5×10^5 and 10×10^5 was measured for different kinds of commercial and experimental oils.

Using the given values of apparent viscosity and shear rate from Table-2.1 (reproduced from Ref.[37]) at 210°F temperature, the viscosity of one kind of oil SAE 10W-40 (C-2) with stryene-ester as VI improver is plotted, Fig.2.1, as a function of shear rate. Using the least-square method, a polynomial of fourth degree was found to represent the viscosity curve of Fig.2.1 and is used to calculate the apparent viscosity (μ_a) corresponding to shear rate ($\dot{\gamma}$) occurring in the big-end bearing clearance space at any crank angle. The

Table-2.1

Apparent viscosities of non-Newtonian oils [37] as function of shear rate at 99°C (210°F)

Shear Rate x 10 ⁻⁵	Low	2.5	5	10
-----> (sec ⁻¹)				
Code no.	Apparent Viscosity (m Pa.S)			
C-1	12.5	10.4	10.0	9.3
C-2	12.6	9.7	9.2	8.7
C-3	13.0	10.5	9.7	9.2
C-4	12.3	10.2	10.0	9.4
C-5	11.9	9.5	9.2	8.8
C-6	11.8	9.6	9.3	9.0
E-1	12.1	11.4	10.9	10.5
E-2	11.9	9.5	9.0	8.7
E-3	11.0	9.3	8.9	8.6
E-4	11.5	8.8	8.5	8.3
E-5	11.9	10.0	9.4	9.0

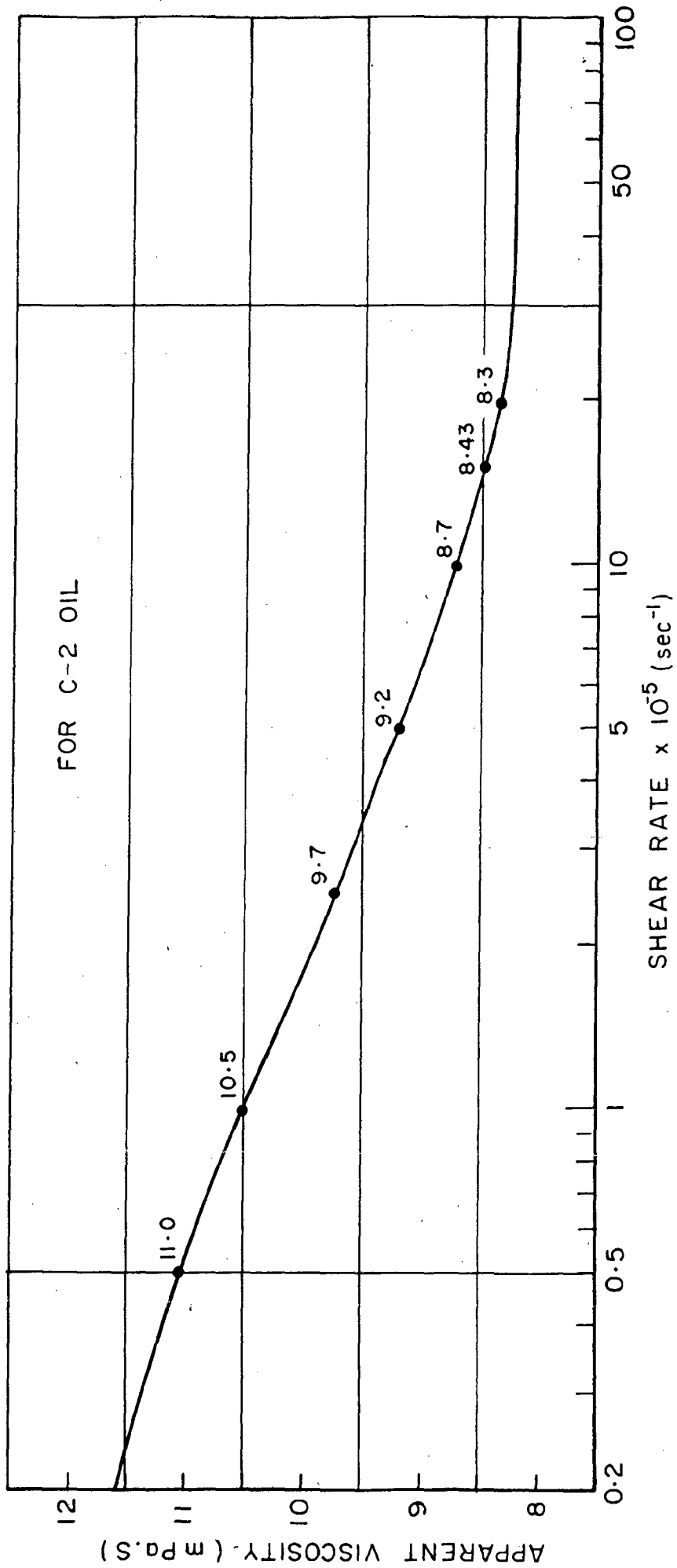


FIG.2.1 Apparent viscosity as a function of shear rate for commercial oil (C-2) at 210°F

dimensional coefficients of the polynomial are given in Table-2.2 for various oils; the polynomial is of the following form,

$$\mu_{\text{a}} = a_0 + a_1\dot{\gamma} + a_2\dot{\gamma}^2 + a_3\dot{\gamma}^3 + a_4\dot{\gamma}^4 \quad (2.20)$$

The orbit (for a finite crank rotation) of the motion of the big-end bearing centre is calculated only for one oil, SAE 10W-40, code C-2 (Appendix A-1), as an example. However the computer program can handle any lubricating oil with any non-Newtonian model.

2.5 PIEZO-THERMAL VISCOSITY CHARACTERISTICS (Piezo-Thermal Effects)

The importance of thermal effects (i.e. viscosity variation across the film thickness due to temperature rise of bearing) on the bearing performance is now well recognized. The temperature rise and its distribution in the bearing has been studied by a number of investigators and Huebner [31] has presented a summary of the work of the investigators on the studies of thermal effects on bearing behaviour for stationary condition. In this dissertation, not only the thermal effect but a combine effect of temperature and pressure on viscosity and in turn on the performance of big-end bearing is studied. The energy equation and its boundary conditions are discussed in the following sections.

2.5.1 Energy Equation:

The equation used to determine the distribution of temperature within the fluid is a mathematical statement of the principle of energy conservation. Pai (1956) has presented a derivation of the energy equation for a fluid, and the full equation in cylindrical coordinates can be written as

Table-2.2

Values of the coefficients (a_0, a_1, a_2, a_3, a_4) for the polynomial, Eq.(2.20), representing the non-linear relation between the apparent viscosity (μ_a) and shear rate ($\dot{\gamma}$) for different non-Newtonian oils

Oil code	Eq.(2.20) $\mu_a = a_0 + a_1\dot{\gamma} + a_2\dot{\gamma}^2 + a_3\dot{\gamma}^3 + a_4\dot{\gamma}^4$				
	a_0	a_1	a_2	a_3	a_4
C-1	11.96	-0.78	0.096	-0.0055	0.11×10^{-3}
C-2	11.31	-0.85	0.111	-0.0065	0.13×10^{-3}
C-3	11.94	-0.88	0.114	-0.0066	0.13×10^{-3}
C-4	10.37	-0.03	-0.017	+0.0012	-0.02×10^{-3}
C-5	10.10	-0.30	0.029	-0.0015	0.03×10^{-3}
C-6	10.22	-0.33	0.039	-0.0022	0.04×10^{-3}
E-1	12.80	-0.76	0.100	-0.0059	0.12×10^{-3}
E-2	10.91	-0.77	0.102	-0.0059	0.12×10^{-3}
E-3	10.60	-0.68	0.089	-0.0051	0.10×10^{-3}
E-4	9.71	-0.48	0.062	-0.0034	0.06×10^{-3}
E-5	11.38	-0.72	0.089	-0.0050	0.10×10^{-3}

2.5.2 The Boundary Conditions for Solution of Energy Equation:

Isoparametric elements with 20 nodes are taken to discretize and analyze the temperature field. The following boundary conditions are applied to solve the energy equation (2.24).

The crank pin surface temperature are specified as constant, i.e. $\bar{T}_i = \bar{T}_c$ and $\delta\bar{T}/\delta n = 0$ at pin surface.

2.5.3 Viscosity Relation with Temperature and Pressure

The following relation is used to calculate the apparent viscosity at each Gaussian integration point of each element to include the effects of temperature and pressure both.

$$\bar{\mu}_{ijk} = \exp \{ \bar{\alpha}_p \bar{p}_{ijk} - \bar{\beta}_T (\bar{T}_{ijk} - 1) \} \quad (2.25)$$

where, $\bar{\beta}_T$ is the viscosity exponent or viscosity temperature coefficient and \bar{T}_{ijk} is the temperature at k^{th} Gaussian point of j^{th} element.

2.5.4 Finite Element Formulation for Energy Equation

Assuming that the unknown temperature distribution within a typical three-dimensional element can be approximated by

$$\bar{T}^e = \sum_{i=1}^s N_i \bar{T}_i^e \quad \text{and} \quad \frac{\delta \bar{T}^e}{\delta \bar{t}} = \dot{\bar{T}}^e = \sum_{i=1}^s N_i \dot{\bar{T}}_i^e$$

where the N_i are approximating functions defined over individual elements, s is the number of nodes per element and \bar{T}_i are the unknown nodal temperatures.

Applying Galerkin's technique, the error distribution principle to be satisfied for an element if

$$\iiint_e N_i \left\{ \bar{K}_v \left[\frac{1}{\bar{R}} \frac{\delta \bar{T}^e}{\delta \bar{t}} + \bar{v} \frac{\delta \bar{T}^e}{\delta \bar{r}} + \frac{\bar{u}}{\bar{r}} \frac{\delta \bar{T}^e}{\delta \theta} + \frac{\bar{w}}{\bar{R}} \frac{\delta \bar{T}^e}{\delta \bar{z}} \right] - \left[\frac{\delta^2 \bar{T}^e}{\delta \bar{r}^2} + \frac{1}{\bar{r}} \frac{\delta \bar{T}^e}{\delta \bar{r}} + \frac{1}{\bar{r}^2} \frac{\delta^2 \bar{T}^e}{\delta \theta^2} + \frac{1}{\bar{R}^2} \frac{\delta^2 \bar{T}^e}{\delta \bar{z}^2} \right] - \bar{K}_p \bar{p} \right\} \frac{\bar{r}}{\bar{R}} d\theta d\bar{r} d\bar{z} = 0 \quad (2.26)$$

The second order terms are converted in first order terms using integration by parts as

$$\iiint_{\text{vol}} N_1 \frac{\delta^2 \bar{T}^e}{\delta \bar{r}^2} d\bar{V} = \iint_{\text{sur}} N_1 \frac{\delta \bar{T}^e}{\delta \bar{r}} \frac{\bar{r}}{\bar{R}} d\theta \cdot d\bar{z} - \iiint_{\text{vol}} \frac{\delta N_1}{\delta \bar{r}} \frac{\delta \bar{T}^e}{\delta \bar{r}} \frac{\bar{r}}{\bar{R}} d\theta \cdot d\bar{r} \cdot d\bar{z} \quad (2.27)$$

Similarly, other second order derivative terms are also integrated by parts.

In view of the adiabatic boundary conditions, the surface integrals vanish on parts (where, $\delta \bar{T} / \delta n = 0$) of the boundary surface, hence the equation (2.26) can be written now as

$$\iiint \left\{ \left\{ N_1 \bar{K}_v \left(\frac{1}{\bar{R}} \frac{\delta \bar{T}}{\delta \bar{r}} + \bar{v} \frac{\delta \bar{T}}{\delta \theta} + \frac{\bar{u}}{\bar{r}} \frac{\delta \bar{T}}{\delta \theta} + \frac{\bar{w}}{\bar{R}} \frac{\delta \bar{T}}{\delta \bar{z}} \right) \right\} - \left\{ \frac{\delta N_1}{\delta \bar{r}} \frac{\delta \bar{T}}{\delta \bar{r}} \right. \right. \\ \left. \left. + \frac{N_1}{\bar{r}} \frac{\delta \bar{T}}{\delta \bar{r}} - \frac{1}{\bar{r}^2} \frac{\delta N_1}{\delta \theta} \frac{\delta \bar{T}}{\delta \theta} - \frac{1}{\bar{R}^2} \frac{\delta N_1}{\delta \bar{z}} \frac{\delta \bar{T}}{\delta \bar{z}} \right\} - N_1 \bar{K}_v \bar{\theta}_v \right\} \frac{\bar{r}}{\bar{R}} d\theta \cdot d\bar{r} \cdot d\bar{z} = 0$$

Eq.(2.28) is rewritten as

$$\iiint \left[\frac{N_1 \bar{K}_v}{\bar{R}} \frac{\delta \bar{T}}{\delta \bar{r}} + \left(N_1 \bar{K}_v \bar{v} + \frac{\delta N_1}{\delta \bar{r}} \frac{N_1}{\bar{r}} \frac{\delta \bar{T}}{\delta \bar{r}} \right) \frac{\delta \bar{T}}{\delta \theta} + \left(\frac{N_1 \bar{K}_v \bar{u}}{\bar{r}} + \frac{1}{\bar{r}^2} \frac{\delta N_1}{\delta \theta} \right) \frac{\delta \bar{T}}{\delta \theta} \right. \\ \left. + \left(\frac{N_1 \bar{K}_v \bar{w}}{\bar{R}} + \frac{1}{\bar{R}^2} \frac{\delta N_1}{\delta \bar{z}} \right) \frac{\delta \bar{T}}{\delta \bar{z}} \right] \frac{\bar{r}}{\bar{R}} d\theta d\bar{r} d\bar{z} = \iiint N_1 \bar{K}_v \bar{\theta}_v \frac{\bar{r}}{\bar{R}} d\theta d\bar{r} d\bar{z} \quad (2.29)$$

The element equation (2.29) in matrix form is written as

$$[\bar{K}_T]^e \cdot \{\bar{T}\}^e_{\bar{t}+\delta \bar{t}} + [\bar{K}_R]^e \cdot \{\bar{T}\}^e_{\bar{t}+\delta \bar{t}} = \{\bar{F}_T\}^e_{\bar{t}+\delta \bar{t}} \quad [\bar{K}_R]^e \cdot \{\bar{T}\}^e_{\bar{t}} \quad (2.30)$$

It is stipulated that once the bearing centre starts to move in a limit cycle in uniform bearing running condition, the temperature of the bearing also become stationary and there is no temperature fluctuation with time: the transient term from Eq.(2.30) can be neglected and Eq.(2.30) reduces to

$$[\bar{K}_T]^e \cdot \{\bar{T}\}^e = \{\bar{F}_T\}^e \quad (2.31)$$

where, the coefficients of matrix $[\bar{K}_T]^e$ and $\{\bar{F}_T\}^e$ are given as

$$\begin{aligned} \bar{K}_{T13}^e = & \iiint_e (\bar{K}_v N_1 \frac{\delta N_3}{\delta \bar{r}} - \frac{20}{k=1} (\sum N_k \bar{v}_k) + \frac{\delta N_1}{\delta \bar{r}} \frac{\delta N_3}{\delta \bar{r}} - \frac{N_1}{\bar{r}} \frac{\delta N_3}{\delta \bar{r}}) \\ & + (\bar{K}_v \frac{N_1}{\bar{r}} \frac{\delta N_3}{\delta \theta} - \frac{20}{k=1} (\sum N_k \bar{u}_k) + \frac{1}{\bar{r}^2} \frac{\delta N_1}{\delta \theta} \frac{\delta N_3}{\delta \theta}) + (\bar{K}_v \frac{N_1}{\bar{R}} \frac{\delta N_3}{\delta \bar{z}} \\ & - \frac{20}{k=1} (\sum N_k \bar{w}_k) + \frac{1}{\bar{R}^2} \frac{\delta N_1}{\delta \bar{z}} \frac{\delta N_3}{\delta \bar{z}}) \frac{\bar{r}}{\bar{R}} d\theta d\bar{r} d\bar{z} \end{aligned}$$

and

$$\bar{F}_{T1}^e = \iiint_e N_1 \bar{K}_v \bar{\theta}_v \frac{\bar{r}}{\bar{R}} d\theta d\bar{r} d\bar{z}$$

$$\{\bar{T}\}^e = \{\bar{T}_1 \bar{T}_2 \bar{T}_3 \dots \bar{T}_{20}\}^T \tag{2.32}$$

$$\begin{aligned} \bar{\theta}_v = & 2\bar{\mu}_m [(\frac{\delta \bar{v}}{\delta \bar{r}})^2 + (\frac{1}{\bar{r}} \frac{\delta \bar{u}}{\delta \theta})^2 + \frac{\bar{v}}{\bar{r}}^2 + (\frac{1}{\bar{R}} \frac{\delta \bar{w}}{\delta \bar{z}})^2 + \frac{1}{2} (\frac{\delta \bar{u}}{\delta \bar{r}} - \frac{\bar{u}}{\bar{r}} \frac{1}{\bar{r}} \frac{\delta \bar{v}}{\delta \theta})^2 \\ & + \frac{1}{2} (\frac{1}{\bar{r}} \frac{\delta \bar{w}}{\delta \theta} + \frac{1}{\bar{R}} \frac{\delta \bar{u}}{\delta \bar{z}})^2 + \frac{1}{2} (\frac{1}{\bar{R}} \frac{\delta \bar{v}}{\delta \bar{z}} + \frac{\delta \bar{w}}{\delta \bar{r}})^2] \end{aligned} \tag{2.33}$$

After the element equation (2.31) are modified for the boundary conditions (Sec.2.5.2), the element contributions are assembled for all the elements and the following system equation is obtained

$$[\bar{K}_T] \{\bar{T}\} = \{\bar{F}_T\} \tag{2.34}$$

CHAPTER - 3

ELASTIC DEFORMATION

It is well known that the elastohydrodynamic (EHD) lubrication plays a significant role in controlling the performance of rolling element bearings. It is also recognised that the deformations also occur in the hydrodynamic journal bearings and the EHD effects are often quite significant. Since the runner and the bearing shell in practice are elastic and deform under hydrodynamic pressure, the correct film geometry, on which hydrodynamic pressure depends, can not be established without taking into account their elastic deformations. The deformation of the bearing can be of the order of the fluid-film thickness (defined for rigid bearing system) when the bearing operates at high eccentricities with heavy loads. The deformation of the bearing appreciably modifies the fluid-film geometry and in turn, may significantly change the pressure distribution in the fluid-film and the performance characteristics of the bearing. The big-end bearing generally operates at high eccentricities and under dynamic loads, so a study of the big-end bearing under EHD lubrication condition, will give a better understanding of its performance.

Mathematically, EHD studies involve simultaneous solutions of hydrodynamic equations for lubricant flow and the elasticity equations for bearing deformations.

3.1 BIG-END BEARING MATERIAL

The bearing materials used in dynamic load service are fairly well standardized. For moderate duty automotive service, strip

bearings containing a babbitt layer of 0.05 mm (0.002in) to 0.127mm (0.005in) thickness over a steel backing are used [68]. For heavier duty service, lead babbitt from 0.025mm(0.001in) to 0.05mm (0.002in) thick is plated over a lead-copper alloy. The lead copper in turn is laid down on a steel base strip. This type of bearings (called trimetal bearings) are normally used in diesel engine service. The thickness of the liner is provided very small hence in the big-end bearing case not only the liner deforms but here complete body of the bearing deform freely so, in the big-end bearing, the deformation of complete body is considered and the material of the body was taken as Iron [42]

3.2 DEFORMATION IN BEARING BODY- FINITE ELEMENT FORMULATION

The analysis of hydrodynamic flow-field is discussed in the Chapter-2. The present Chapter-3 deals with the elastic deformation of the bearing body.

The bearing body is discretized using eight noded hexahedral isoparameteric elements. The displacement components in the elements are considered to vary linearly and are represented by

$$\{\bar{\delta}\} = \begin{Bmatrix} \bar{d}_x \\ \bar{d}_y \\ \bar{d}_z \\ \bar{d}_e \end{Bmatrix} = [M^e] \{d\} \quad (3.1)$$

Within the realm of linear elastic theory, the expression for the potential energy for an element in the discretized elastic domain when the bearing is subjected only to surface traction force $[T_x]$, is given by [69]

$$\bar{U}^e = 1/2 \iiint \{\bar{y}\}^T \{\bar{\sigma}\} dV^e - \iint [T_x] \{\bar{\delta}\} dA^e \quad (3.2)$$

or

$$\bar{T} = 1/2 \iiint [S][L]^T [D][L]\{S\} dV - \iint [T_z]\{S\} dA \quad (3.3)$$

where, $\{Y\}$ is known as the strain matrix and $\{\sigma\}$ is called the stress matrix.

The strain matrix can be defined as [69]

$$\{Y\} = \begin{Bmatrix} \gamma_x \\ \gamma_y \\ \gamma_z \\ \gamma_{\theta} \\ \gamma_{z\theta} \\ \gamma_{r\theta} \\ \gamma_{rz} \end{Bmatrix} = \begin{Bmatrix} \frac{\delta d_x}{r'} \\ \frac{\delta d_x}{r'} \\ \frac{\delta d_x}{r'} \\ \frac{\delta d_x}{r'} + \frac{\delta d_x}{r'} \delta \theta \\ \frac{1}{r'} \delta d_x + \frac{\delta d_x}{\delta z'} \\ \frac{1}{r'} \delta d_x + \frac{\delta d_x}{\delta r'} - \frac{d_\theta}{r'} \\ \frac{\delta d_x}{\delta z'} + \frac{\delta d_x}{\delta r'} \end{Bmatrix}$$



179832
Central Library University of Roorkee
ROORKEE

$$= \begin{Bmatrix} \frac{\delta}{r'} & 0 & 0 \\ 0 & \frac{\delta}{\delta z'} & 0 \\ 1 & 0 & \frac{1}{r'} \frac{\delta}{\delta \theta} \\ 0 & \frac{1}{r'} \frac{\delta}{\delta \theta} & \frac{\delta}{\delta z'} \\ \frac{1}{r'} \frac{\delta}{\delta \theta} & 0 & \frac{\delta}{r'} \\ \frac{\delta}{\delta z'} & \frac{\delta}{\delta r'} & 0 \end{Bmatrix} \begin{Bmatrix} d_r \\ d_x \\ d_e \end{Bmatrix} = [L] \{ \$ \} \quad (3.4)$$

$[L]$ is known as the operator matrix, and $\{ \$ \} = [d_r \ d_x \ d_e]$.

The stress vector is given by

$$\{ \sigma \} = [D_a] \{ Y \} = [D_a] [L] \{ \$ \} \quad (3.5)$$

in which $[D_a]$ matrix is called elasticity matrix and may be defined as,

$$[D_a] = E \begin{bmatrix} G_1 & G_2 & G_2 & 0 & 0 & 0 \\ G_2 & G_1 & G_2 & 0 & 0 & 0 \\ G_2 & G_2 & G_1 & 0 & 0 & 0 \\ 0 & 0 & 0 & G_3 & 0 & 0 \\ 0 & 0 & 0 & 0 & G_3 & 0 \\ 0 & 0 & 0 & 0 & 0 & G_3 \end{bmatrix} \quad (3.6)$$

$$\text{where, } G_1 = \frac{(1 - \mu_p)}{(1 + \mu_p)(1 - 2\mu_p)} ; G_2 = \frac{\mu_p}{(1 + \mu_p)(1 - 2\mu_p)} ; \text{ and } G_3 = \frac{1}{2(1 + \mu_p)}$$

μ_p is the Poisson's ratio of the material.

System equations are derived by minimizing the potential energy with respect to the nodal displacement components and this gives

$$\left. \begin{array}{c} \delta \bar{T} \\ \dots \\ \delta \bar{d}_x \\ \dots \\ e_m \delta \bar{T} \\ \Sigma \\ e=1 \dots \\ \delta \bar{d}_x \\ \dots \\ \delta \bar{T} \\ \dots \\ \delta \bar{d}_e \end{array} \right\} = 0 \quad (3.7)$$

Using Eq.(3.3), Eqs.(3.7) are written as

$$\sum_{e=1}^{e_m} \iiint [B_d]^T [D_d] [B_d] \{d\} r' d\theta dr' dz' - \iint [M^{**}] \{T_z\} R_d d\theta dz' = 0 \quad (3.8)$$

$$\text{where, } [B_d] = [L] [M^{**}] \quad (3.9)$$

The traction force over the bearing surface is caused due to hydrodynamic pressure and is written as

$$\{T_z\} = \begin{Bmatrix} F_z \\ F_x \\ F_\theta \end{Bmatrix} = \begin{Bmatrix} \sum_{i=1}^4 M_i p_{zi} \\ \sum_{i=1}^4 M_i p_{xi} \\ \sum_{i=1}^4 M_i p_{\theta i} \end{Bmatrix} \quad (3.10)$$

Nodal pressures \bar{p}_{x1} , \bar{p}_{y1} and \bar{p}_{z1} are the components of the hydrodynamic pressure at the i^{th} node of element e . Integrations in Eq.(3.8) are carried out using Gaussian quadrature formula to obtain a set of simultaneous algebraic equations in terms of the nodal displacement vectors $\{d\}$.

$$\sum_{e=1}^{e_m} ([K_d] \{d\} - \{F_o\}) = 0 \quad (3.11)$$

The matrix $[K_d]$, and vector $\{F_o\}$ respectively represent the element stiffness and equivalent nodal force due to surface traction force $\{T_x\}$, Eq.(3.10).

Normalizing Eqs.(3.10-3.11) by $\bar{r}' = \frac{r'}{t_n}$, $\bar{z}' = \frac{z'}{t_n}$, $[\bar{D}_d] = \frac{[D_d]}{E}$,

$$\{\bar{d}\} = \frac{\{d\}}{c} \quad \text{and} \quad \bar{p} = \frac{p}{\mu_o \Omega (R/c)^2} \quad \text{and} \quad \bar{R}_B = \frac{R_B}{t_n} = \frac{(R+c)}{t_n} \quad \text{and assembling}$$

the element contributions for the entire displacement field, the non-dimensional global system equation is obtained.

$$[\bar{K}_d] \{\bar{d}\} = \bar{\Phi} \{\bar{F}_o\} \quad (3.12)$$

where, the nondimensional coefficients of the element matrix are given as

$$\bar{K}_{d_{ij}} = \iiint [\bar{B}_d]^T [\bar{D}_d] [\bar{B}_d] \bar{r}' d\theta dr' dz'$$

$$= \int_{-1}^{+1} \int_{-1}^{+1} \int_{-1}^{+1} [\bar{B}_d]^T [\bar{D}_d] [\bar{B}_d] \bar{r}' |J| d\xi d\eta d\zeta$$

and

$$\bar{F}_{o_{1j}} = \iint [M^*] \{\bar{T}_x\} \bar{R}_B d\theta dz'$$

$$\{\bar{d}\} = [\bar{d}_r \ \bar{d}_\theta \ \bar{d}_z]^T$$

$$\bar{\phi} = \left(\frac{\mu_0 \Omega}{E} \right) \left(\frac{t_h}{R} \right) \left(\frac{R}{c} \right) \text{ is a nondimensional quantity known}$$

as the deformation coefficient [36], and \bar{R}_B is the nondimensional radius of bearing inner surface.

3.3 LOADING AND BOUNDARY CONDITIONS

In big-end bearing case, the complete body of the bearing deforms freely in all direction because it is free to expand in space. Only those element nodes which lie at the junction of connecting-rod and the bearing are assumed as fixed nodes and hence

$$\{\bar{d}\}_j = 0 \quad (3.13)$$

where, j is the node number of the nodes at the outer surface of the bearing lie on the junction of the connecting-rod and bearing, Fig.3.1. The tangential traction forces (\bar{F}_θ , \bar{F}_z) at bearing shell-fluid-film interface are zero and only non zero value of the radial traction (\bar{F}_r) is obtained. This reduces the external fluid-film force vector for an element, to

$$\{\bar{F}_e\} = [\bar{F}_r \quad 0 \quad 0]^T \quad (3.14)$$

where, j^{th} node falls on the interface between the fluid-film and the bearing shell.

Mathematically, the elastic deformation problem now reduces to the determination of displacements $\{\bar{d}\}$ in the bearing by solving Eq.(3.12) satisfying the boundary conditions Eq.(3.13) and with the load given by Eq.(3.14).

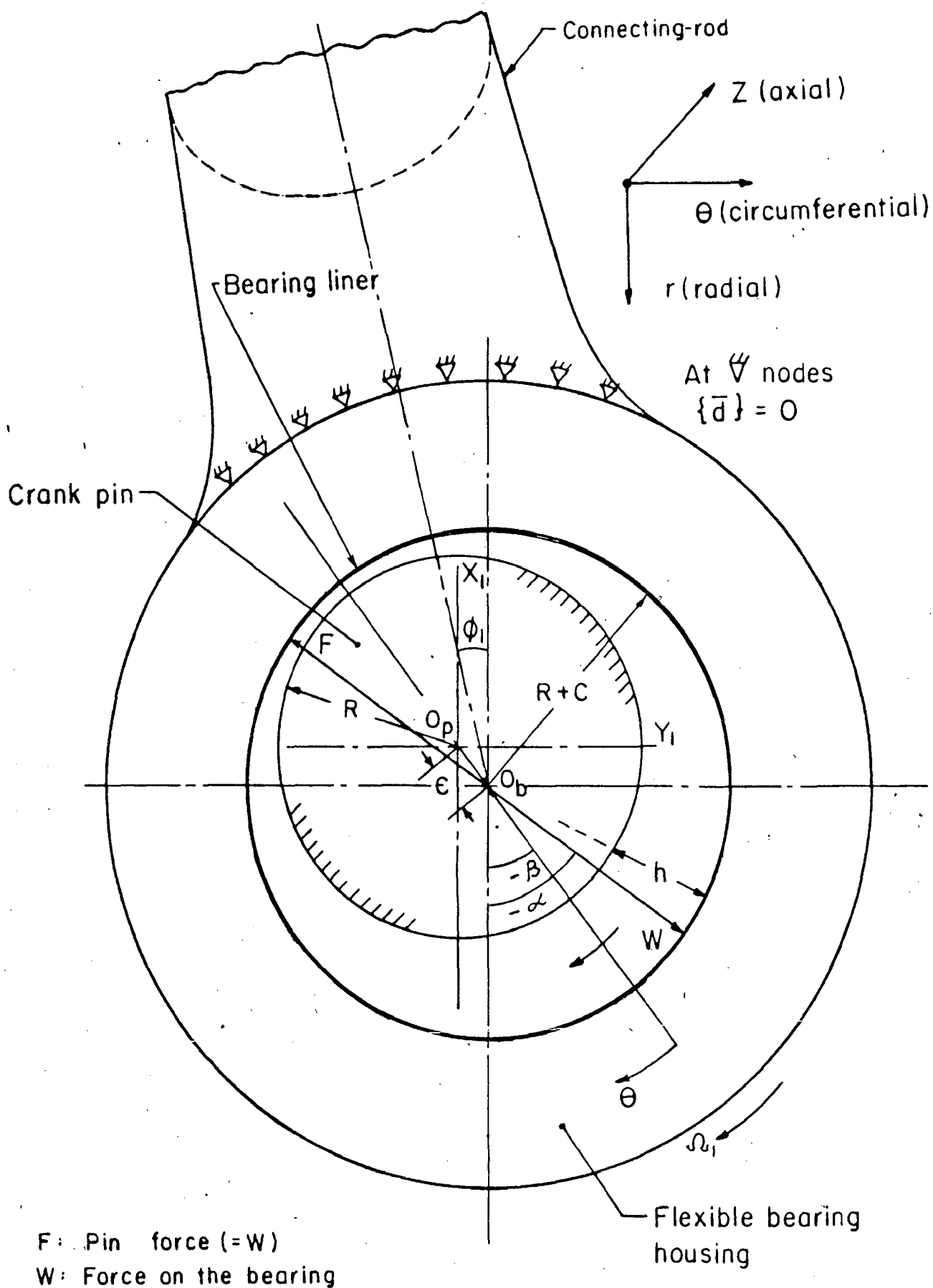


Fig. 3-1 Big-end bearing geometry

CHAPTER 4

BEARING CHARACTERISTICS

4.1 Bearing Force and Relative Motion

The big-end bearing is subjected to a complex dynamic load. The components of the dynamic load on the bearing as a function of the crank angle, can be computed from the engine data, viz., geometry, component masses and inertia, and pressure history.

The acceleration (A) of the piston of a slider crank mechanism, Fig.4.1, is given by [62],

$$A = R_1 \Omega^2 \left[\cos \theta_1 + \frac{(q^2 - 1) \cos 2\theta_1 + \cos^4 \theta_1}{(q^2 - \sin^2 \theta_1)^{3/2}} \right] \quad (4.1)$$

The inertia force of the reciprocating masses (piston, gudgeon pin and the small-end of the connecting-rod) is obtained from the relation

$$F_I = (M_1 + M_P) \times A \quad (4.2)$$

where, M_1 (usually equal to $(1/3) M_T$) is the equivalent mass of the connecting-rod at the small-end.

A centrifugal force ($F_1 = M_2 R_1 \Omega^2$) of constant magnitude is experienced by the big-end bearing, where M_2 (usually equal to $(2/3) M_T$) is the mass associated with the big-end bearing.

The gas force ($F_G = (\pi/4) D^2 p_G$) acts on the piston and is transmitted to the bearing through the connecting-rod, Fig.4.1.

The resultant force (W) on the bearing is given by

$$W = [F_1^2 + F_2^2 - 2F_1 F_2 \cos(\theta + \theta_1)]^{1/2} \quad (4.3)$$

where,

$$F_2 = (F_G - F_I) \sec \theta_1 \quad (4.4)$$

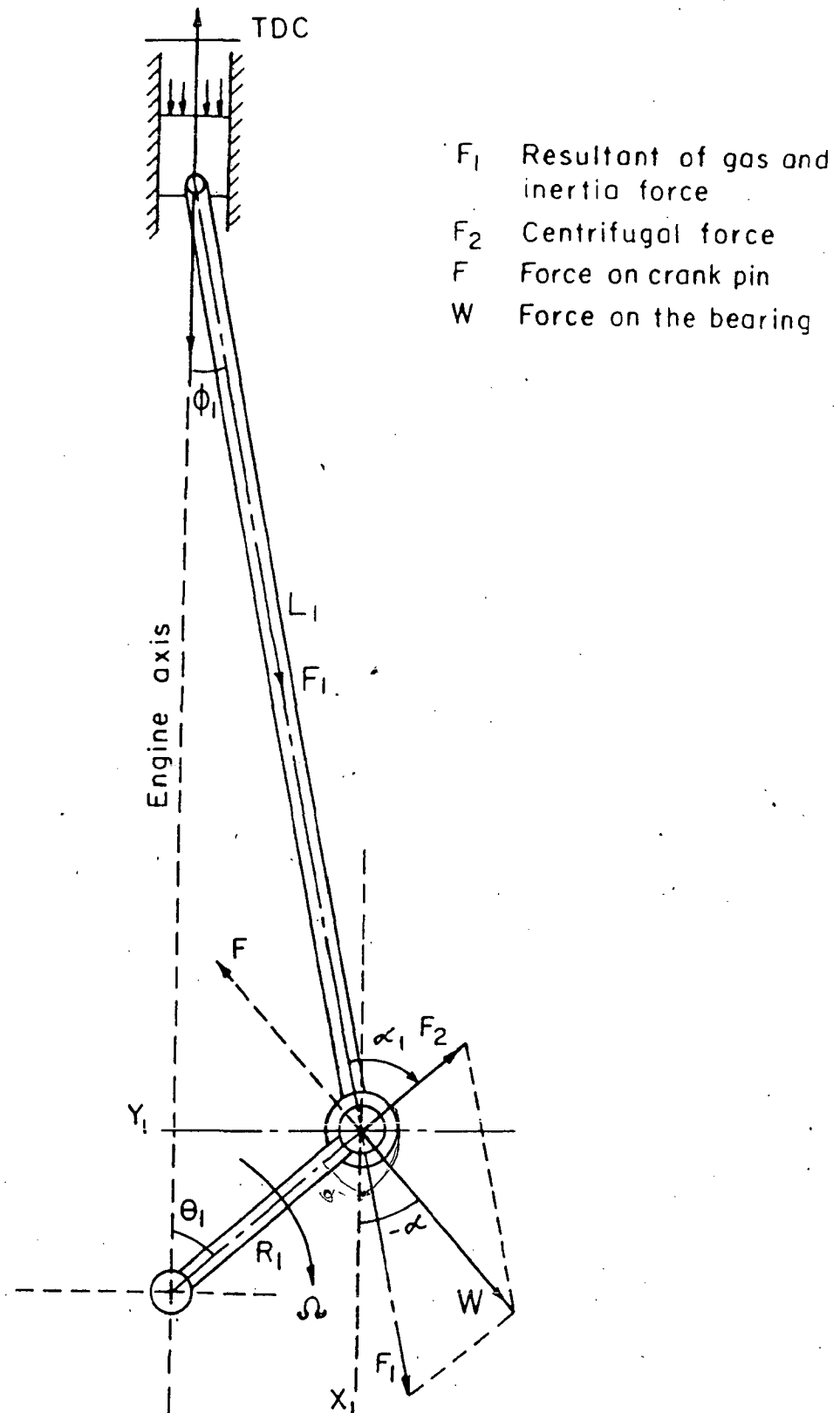


Fig. 4-1 Forces acting on a slider crank mechanism

The reaction of the resultant force (W) on the crank-pin is in the opposite direction as shown in Fig.4.1 and is denoted by F (external force = W). The profiles of the polar plot of load W , although unique to an individual engine bearing, are typically similar to the one plotted, Fig.4.2, from the load components given by Campbell et al [10] which are compiled in Table A-4.1, Appendix A-4.

The angular speed of the bearing (Ω_1) relative to the crank-pin is function of time due to the oscillating motion of the connecting-rod. From Fig.4.1,

$$\alpha_1 = \theta_1 + \phi_1 \quad (4.5)$$

Differentiating Eq.(4.5) with respect to time (t),

$$\frac{d\alpha_1}{dt} = \frac{d\theta_1}{dt} + \frac{d\phi_1}{dt} \quad (4.6)$$

Using the relations $\sin\phi_1 = \frac{\sin\theta_1}{q}$ and $\frac{d\phi_1}{dt} = \frac{\cos\theta_1}{r(q^2 - \sin^2\theta_1)} \frac{d\theta_1}{dt}$,

Eq.(4.6) can be written as

$$\frac{d\alpha_1}{dt} = \frac{d\theta_1}{dt} \left[1 + \frac{\cos\theta_1}{r(q^2 - \sin^2\theta_1)} \right]$$

or

$$\Omega_1 = \Omega \left[1 + \frac{\cos\theta_1}{r(q^2 - \sin^2\theta_1)} \right]$$

and

$$\bar{\Omega}_1 = \frac{\Omega_1}{\Omega} = \left[1 + \frac{\cos\theta_1}{r(q^2 - \sin^2\theta_1)} \right] \quad (4.7)$$

$\bar{\Omega}_1$ is the nondimensional speed of the bearing relative to the crank-pin or vice-versa and is a function of crank angle (θ_1). The dimensional relative speed (N_B) of the bearing in the example is shown in Fig.4.3.

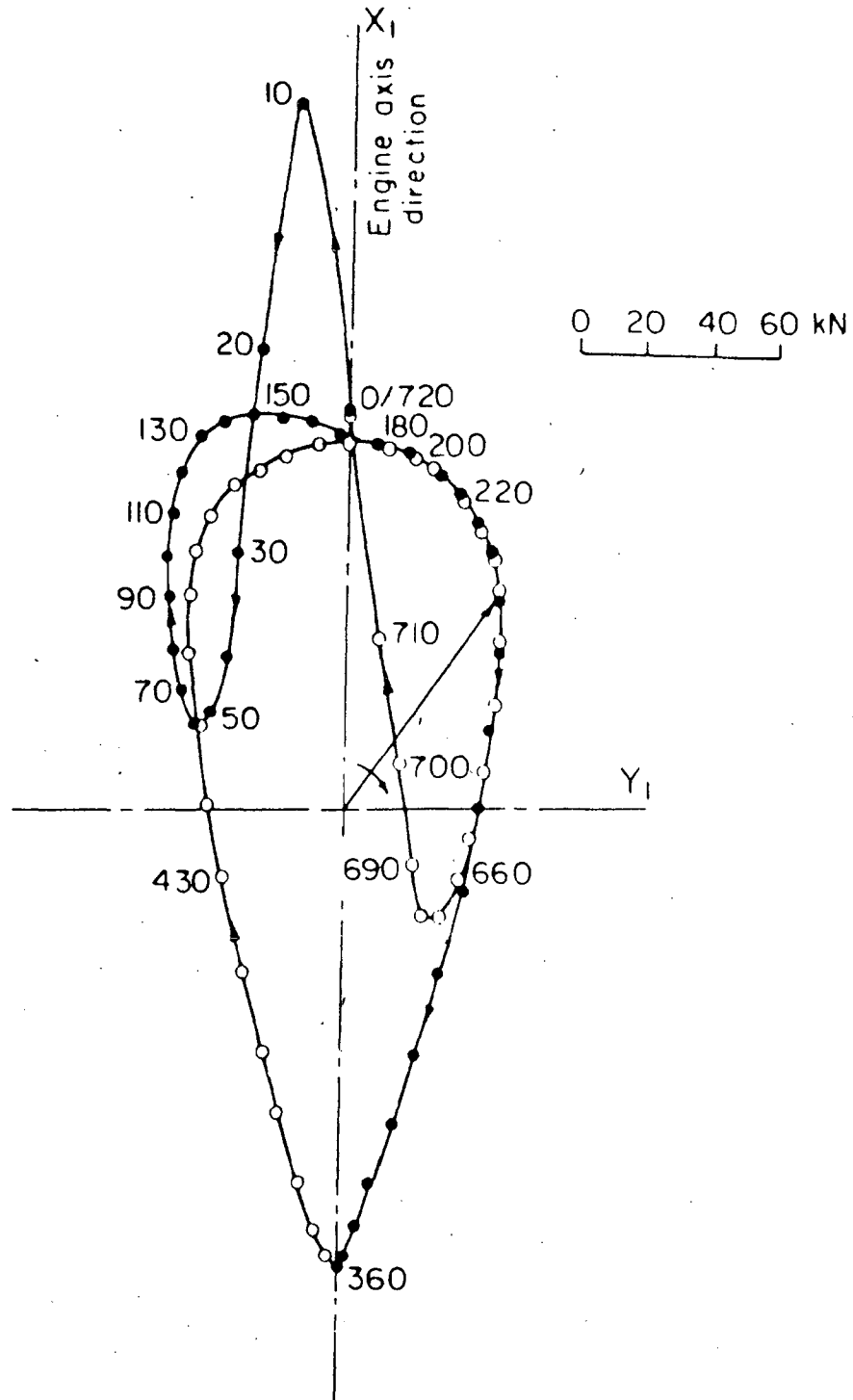


Fig.4.2 Polar force diagram of the big-end bearing
(centrifugal force + inertia force + gas force)

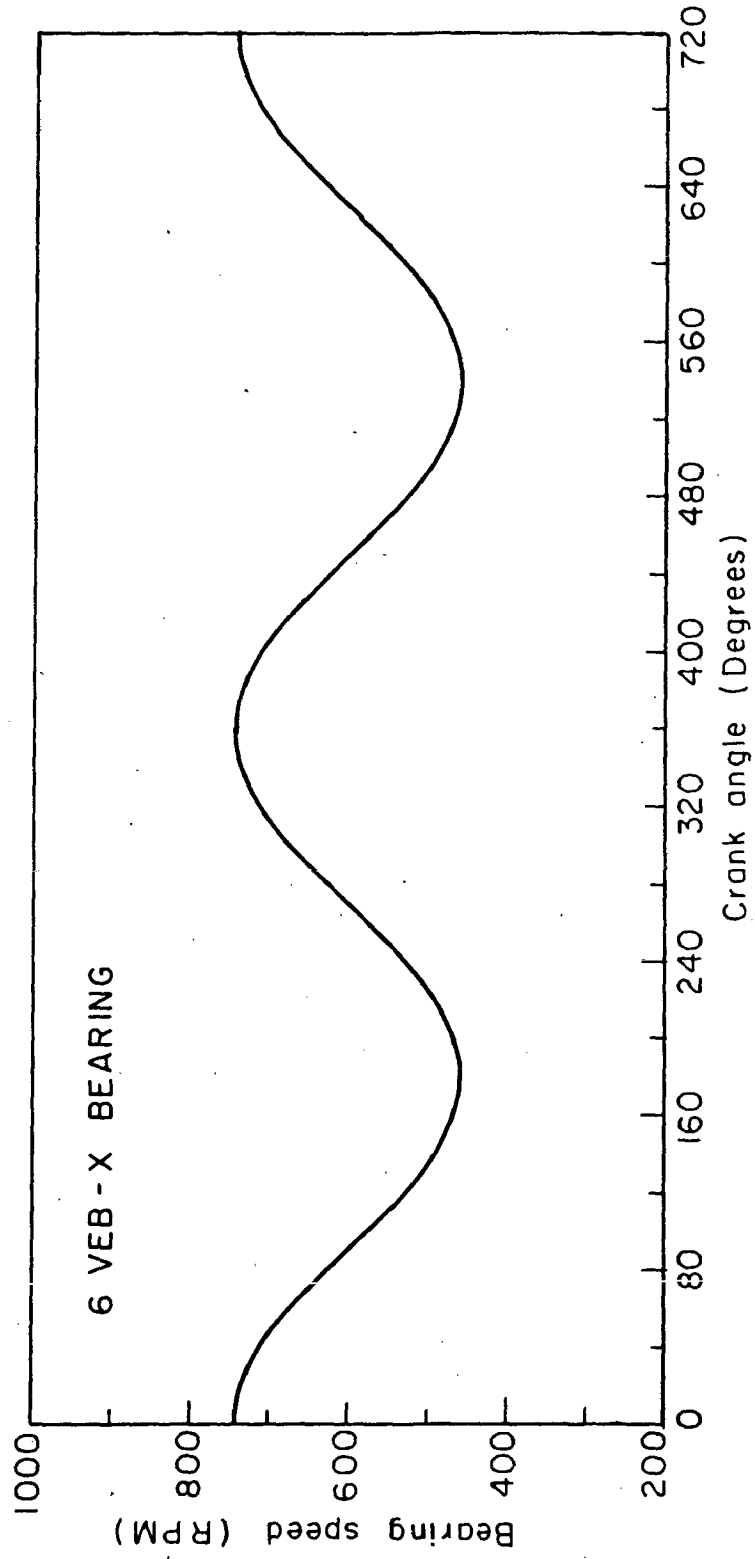


Fig. 4.3 Variation of bearing speed

4.2 FRICTION FORCE AND POWER LOSS

The power loss in the bearing is caused by the viscous resistance of the lubricant in the clearance space to the relative motion between the bearing and the crank-pin surfaces. Power loss is directly proportional to the viscosity of the lubricant, increases as the square of the speed and decreases as the oil film thickness is increased.

In a journal bearing, the shear stress at the moving surface is,

$$\tau = \mu_m \frac{\delta V_e}{\delta r} \quad (4.8)$$

In a big-end bearing, the friction force on the bearing surface may be obtained as

$$F_f = \int_{-L/2}^{+L/2} \int_0^{2\pi} \mu_m \frac{\delta V_e}{\delta r} (R+c) d\theta dz \quad (4.9a)$$

or

$$F_f = \int_{-L/2}^{+L/2} \int_0^{2\pi} \mu_m \frac{\delta V_e}{\delta r} R\{1+(c/R)\} d\theta dz \quad (4.9b)$$

In Eq.(4.9b), the value of c/R is very small and can be ignored. This reduces the friction force expression to the following form,

$$F_f = R \int_{-L/2}^{+L/2} \int_0^{2\pi} \mu_m \frac{\delta V_e}{\delta r} d\theta dz \quad (4.9c)$$

Using the normalizing factors,

$$\bar{\mu}_m = \frac{\mu_m}{\mu_o}; \quad \bar{u} = \frac{\delta V_e}{R\Omega}; \quad \bar{z} = \frac{z}{R}; \quad \text{and } \bar{F}_f = \frac{F_f}{\mu_o R^2 \Omega (R/c)}; \quad \bar{r} = \frac{r}{c}$$

$$\bar{F}_f = \int_{-B}^{+B} \int_0^{2\pi} \bar{\mu}_m \frac{\delta \bar{u}}{\delta \bar{r}} d\theta d\bar{z} \quad (4.10a)$$

or

$$\bar{F}_x = \int_{-1}^{+1} \int_{-1}^{+1} \bar{\mu}_m \sum_{i=1}^{20} \left(\frac{\delta N_i}{\delta \bar{r}} \bar{u}_i \right) |J_m| d\xi d\zeta \quad (4.10b)$$

The nondimensional power loss can be written as

$$\bar{P} = \int_{-1}^{+1} \int_{-1}^{+1} \bar{\mu}_m \sum_{i=1}^{20} \left(\frac{\delta N_i}{\delta \bar{r}} \bar{u}_i \right) \sum_{j=1}^{20} (N_j \bar{u}_j) |J_m| d\xi d\zeta \quad (4.11)$$

where,

$$\bar{P} = \frac{P}{\mu_o \Omega^2 R^3 (R/c)}$$

The friction force and power loss has been calculated using a single land of the 6VEB-X engine bearing and the total power loss is twice of the calculated value.

To consider the piezoviscous effect, the viscosity at Gaussian points may be written as

$$(\bar{\mu}_m)_k = e^{\bar{\alpha}_p \bar{p}_k} \quad (4.12)$$

where, $\bar{p}_k = \sum_{i=1}^4 N_i \bar{p}_i$ at k^{th} Gaussian point on the surface of the bearing-shell in contact with the fluid-film.

4.3 EQUATIONS OF MOTION OF THE BEARING CENTRE (Fig.4.4)

The big-end bearing is subjected to dynamic load, and so the bearing centre moves around the crank pin centre in an orbit. As the bearing centre moves around the pin centre, it acquires squeeze and whirl velocity components. The equations of motion can be written by equating the algebraic sum of all the forces acting on the bearing to zero in two mutually perpendicular directions. The external force (\bar{W}) is balanced by the forces generated by the hydrodynamic wedge, squeeze, and whirling actions of the fluid-film under the dynamic

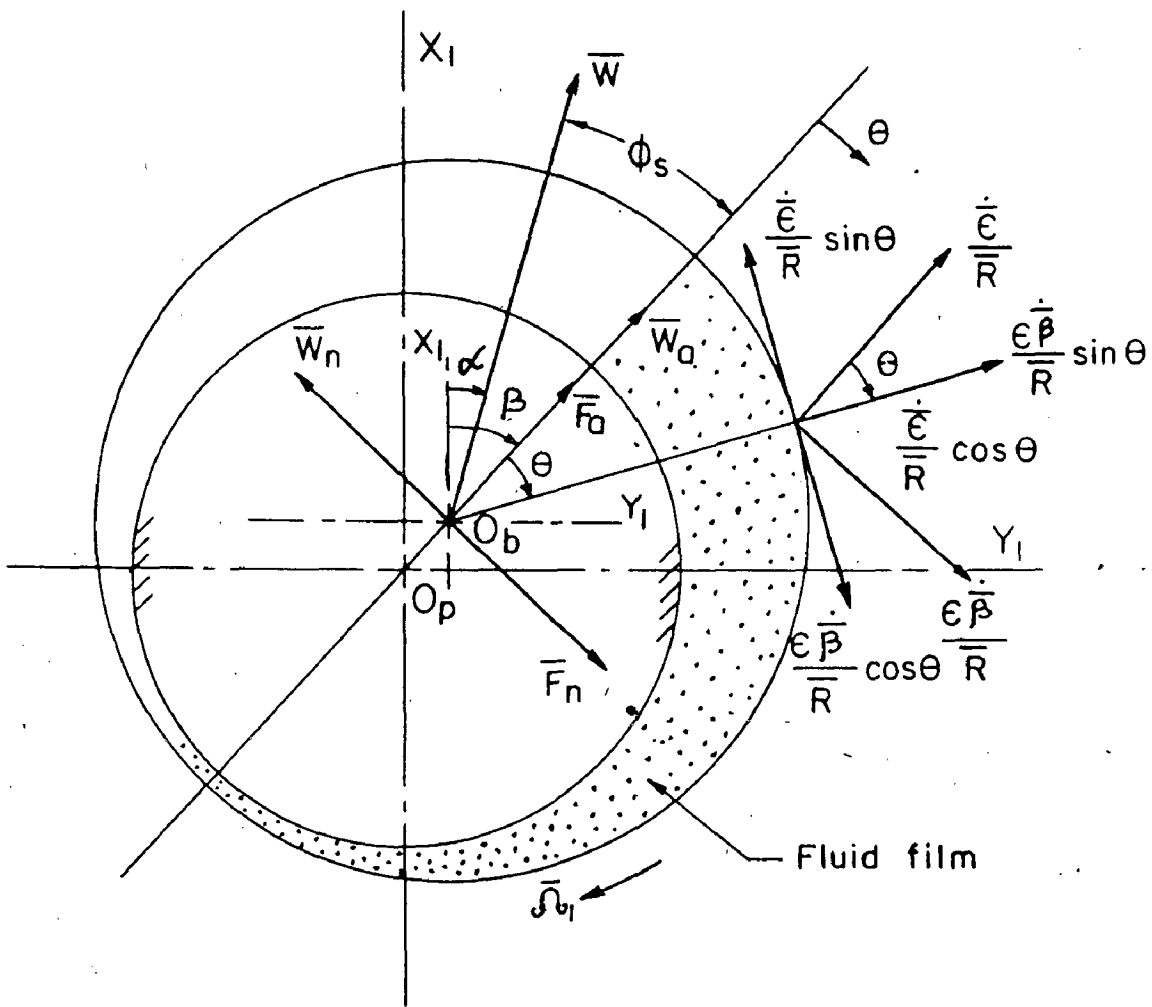


Fig. 4.4 Kinematic and dynamic quantities for a journal bearing system

loading condition and the inertia force components due to mass (M_2) associated with the big-end bearing. The equations of motion of the big-end bearing centre are thus,

$$\bar{S}_1 + \bar{F}_n(\dot{\epsilon}, \dot{\beta}) + \bar{W}_n - \bar{M}_2 \times (\ddot{\epsilon} - \epsilon \dot{\beta}^2) = 0 \quad (4.13a)$$

$$\bar{S}_4 + \bar{F}_n(\dot{\epsilon}, \dot{\beta}) - \bar{W}_n - \bar{M}_2 \times (2\dot{\epsilon} \dot{\beta} + \epsilon \ddot{\beta}) = 0 \quad (4.13b)$$

The inertia force components (i.e. $\bar{M}_2(\ddot{\epsilon} - \epsilon \dot{\beta}^2)$ and $\bar{M}_2(2\dot{\epsilon} \dot{\beta} + \epsilon \ddot{\beta})$) are generally quite small [40], in the range of 10^{-4} times the external force (\bar{W}) as compared to the other force components in the equations of motion (Eqs.4.13a-4.13b). After linearizing and ignoring the inertia forces associated with the bearing accelerations, the equations of motion (Eqs.4.13a-4.13b) reduce to

$$\bar{S}_1 + \dot{\epsilon} \bar{S}_2 + \dot{\beta} \bar{S}_3 + \bar{W}_n = 0 \quad (4.14a)$$

$$\bar{S}_4 + \dot{\epsilon} \bar{S}_5 + \dot{\beta} \bar{S}_6 - \bar{W}_n = 0 \quad (4.14b)$$

CHAPTER - 5

SOLUTION SCHEME AND COMPUTER PROGRAM STRUCTURE

The analysis of connecting-rod big-end bearing, which is subjected to a dynamic load, Fig. 4.2, presents a complex non-linear time dependent problem. Therefore, the solution strategy for the big-end bearing is also not direct but differs from the solution methods for the conventional static and dynamic journal bearing problems. In the following sections, the solution technique used for the numerical integration of the equations of motion of the big-end bearing centre to obtain the orbit is presented.

The sustenance of fluid-film, consistent with its required minimum thickness, in the clearance space between the bearing and the crank pin, is essential to avoid undue wear of the pin and the bearing surfaces. Theoretically calculated bearing centre orbit trajectory readily gives the time history of the variation of the minimum film thickness. The orbit is obtained by using a numerical time marching integration scheme for 0° to 720° (two crank revolutions) crank rotation. Euler-Cauchy's predictor-corrector method with suitable time intervals in terms of crank rotation angle is used in the time marching scheme.

The bearing in example consists a full (2π) circumferential groove in mid plane. Therefore, it is analyzed by taking only one land ($L/2R = 0.28125$) which is subjected to one half of the given load.

But to solve the same bearing without groove, the full length

(including the width 12.7 mm of the groove, $(L/2R) = 0.625$) which is subjected to full load, is considered. To account for misalignment of the bearing axes at the time of bearing assembly in the connecting-rod end, the film thickness expression is modified accordingly. The problems is also extended from the rigid bearing condition to the flexible bearing.

5.1 SOLUTION PROCEDURE TO OBTAIN NODAL PRESSURES, VELOCITY FIELD AND FLUID-FILM FORCES

According to the analysis given in the foregoing Chapters, the aim is to obtain the bearing centre orbit which require the solution of equations of motion, Eq.(4.14). To solve the equations of motion, the forces \bar{S}_1 to \bar{S}_6 are required and hence in turn nodal pressures are to be obtained first. The complete solution method is divided in two main parts:

1. To obtain the nodal pressures for rigid bearing and for EHD bearing, and
2. To obtain orbit using the information from the first part of the solution.

For the first part, the solution algorithm is as follows:

5.1.1 Rigid Bearing

5.1.1a Isoviscous Lubricants

In the case of rigid bearing with isoviscous lubricant, the pressure, velocity field, positive pressure zone and the fluid-film force components (\bar{S}_1 to \bar{S}_6) are obtained as follows :

A value of eccentricity ratio(ϵ) is given as input data alongwith viscosity $\bar{\mu}_m = 1$ and the already defined data for bearing geometry in the computer program. First for the given value of ϵ , the mesh of the elements (global nodal numbers and three (r, θ, z) coordinates) is

generated for full (2π) film, using the full Sommerfeld boundary condition, Fig. 5.1a. From the momentum equations (Eqs.2.2a-2.2c) and the continuity equation (Eq.2.4), and using the Galerkin's finite-element technique, the element fluidity matrix and other element matrices are derived (Sec.2.3). In the element equations, the boundary conditions (Eqs.2.5a-2.5f) are incorporated to minimize the computer storage. By the usual assembly method, the global fluidity matrix and the right hand side column vectors represented by Eq.(2.16) are obtained. The global system equation (2.16) is then solved by the direct Gauss elimination method. The elimination operations are done simultaneously to all three right hand side vectors and this gives three solution vectors having nodal pressures and velocity field corresponding to wedge, squeeze and whirl actions in the fluid-film.

In the pressure field, since 2π film was assumed, there is a zone of negative resultant nodal pressures. The fluid-film can not sustain the negative pressure, hence, before integration of pressures over bearing area to calculate force components, the positive pressure zone is established by taking into consideration the following criteria:

All the three actions (wedge, squeeze and whirl) take place simultaneously in the clearance space of the bearing, the resultant nodal pressure (\bar{p}_j) may be defined as the algebraic sum of three pressures such as

$$\bar{p}_j = \bar{p}_{Hj} + \dot{\epsilon} \bar{p}_{Ej} + \dot{\beta} \bar{p}_{Bj} \quad (5.1)$$

Hence, at those nodes where the resultant pressure (\bar{p}_j) is negative, all the three pressure components (\bar{p}_{Hj} , \bar{p}_{Ej} , \bar{p}_{Bj}) are set to zero. In this way, the remaining nodes having the positive values of resultant pressure establish the positive pressure zone. The modified

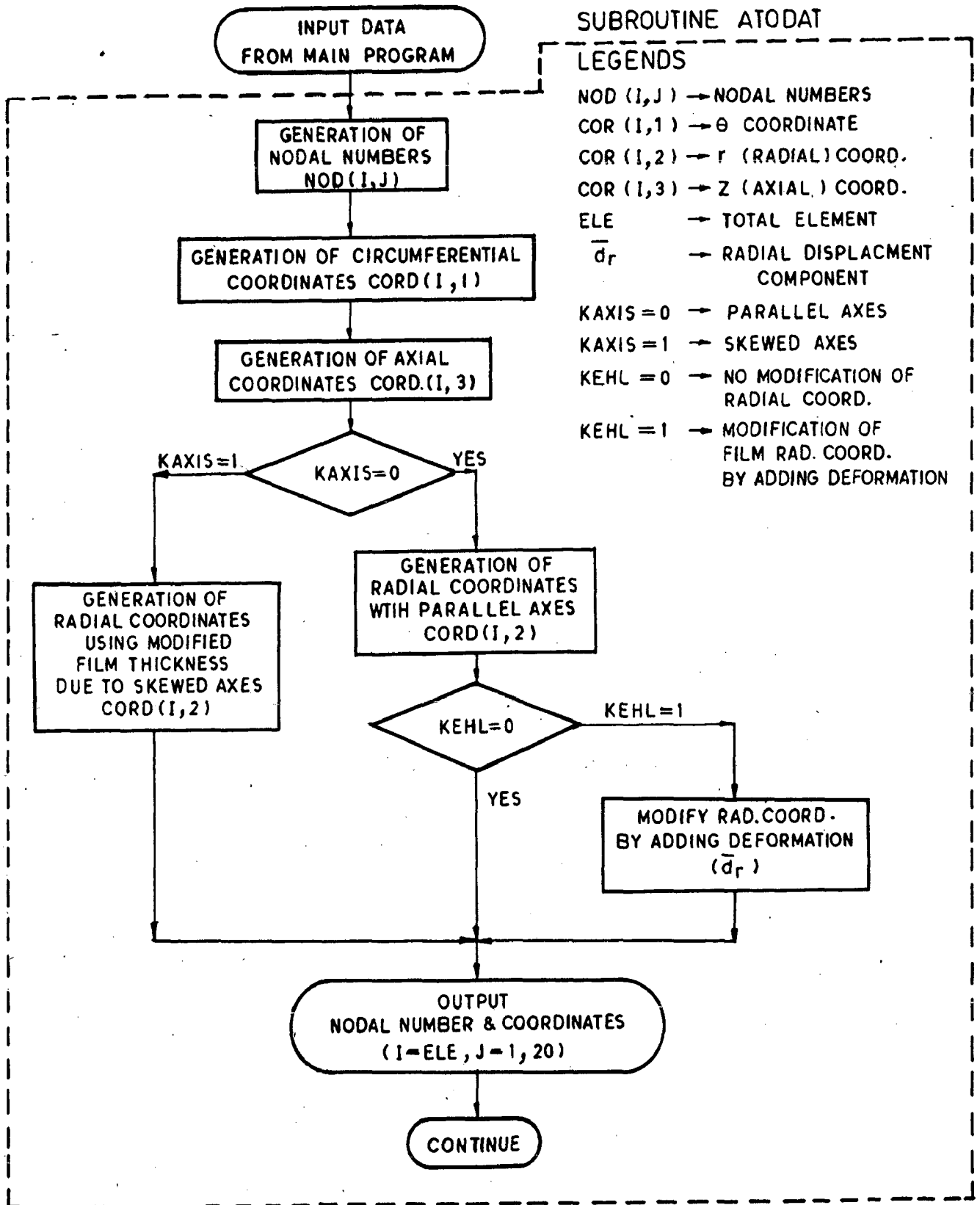


Fig. 5-1 a Flow diagram for mesh generation (Subroutine ATODAT)

pressure vectors after proper integration over the bearing area give the force components \bar{S}_1 to \bar{S}_6 . The flow diagram of the algorithm is shown in BLOCK-I, Fig. 5.1b. The computer program including subroutine ATODAT, Fig. 5.1a, represented by flow diagram, Fig. 5.1b, gives the nodal pressures, velocity field and force components \bar{S}_1 to \bar{S}_6 for the given eccentricity ratio (ϵ) for rigid bearing isoviscous case.

5.1.1b Piezoviscous Lubricants

To take into account the effect of variation of viscosity with pressure (piezoviscous effect), the initial trial solution is obtained with $\bar{\mu}_a = 1$ as described in Section 5.1.1a, BLOCK-I, Fig. 5.1b. Then using the values of resultant nodal pressures obtained from BLOCK-I (after establishing the positive pressure zone), the apparent viscosity ($\bar{\mu}_a$) is calculated on each Gaussian integration point of each element using the following relation.

$$\bar{\mu}_{ajk} = \exp(\bar{\alpha}_p \bar{p}_{jk}) \quad (4.12')$$

where, subscripts j and k represent respectively the element and the Gaussian integration point. Using these new values of viscosity $\bar{\mu}_{ajk}$, the new element stiffness matrices are generated. The modified global system equations yield the new pressure and velocity fields, and forces \bar{S}_1 to \bar{S}_6 . The flow diagram for the piezoviscous lubricant case utilizing flow diagram of BLOCK-I, Fig. 5.1b, is shown in BLOCK-II, Fig. 5.2, which can be used to get the solution for a rigid bearing with a piezoviscous lubricant.

5.1.1c Lubricants having Piezo-Thermal Viscosity Characteristics

For considering the combined effects of temperature and pressure on viscosity, the initial trial solution is again obtained first for the corresponding isoviscous ($\bar{\mu}_a = 1$) case, and then the temperature

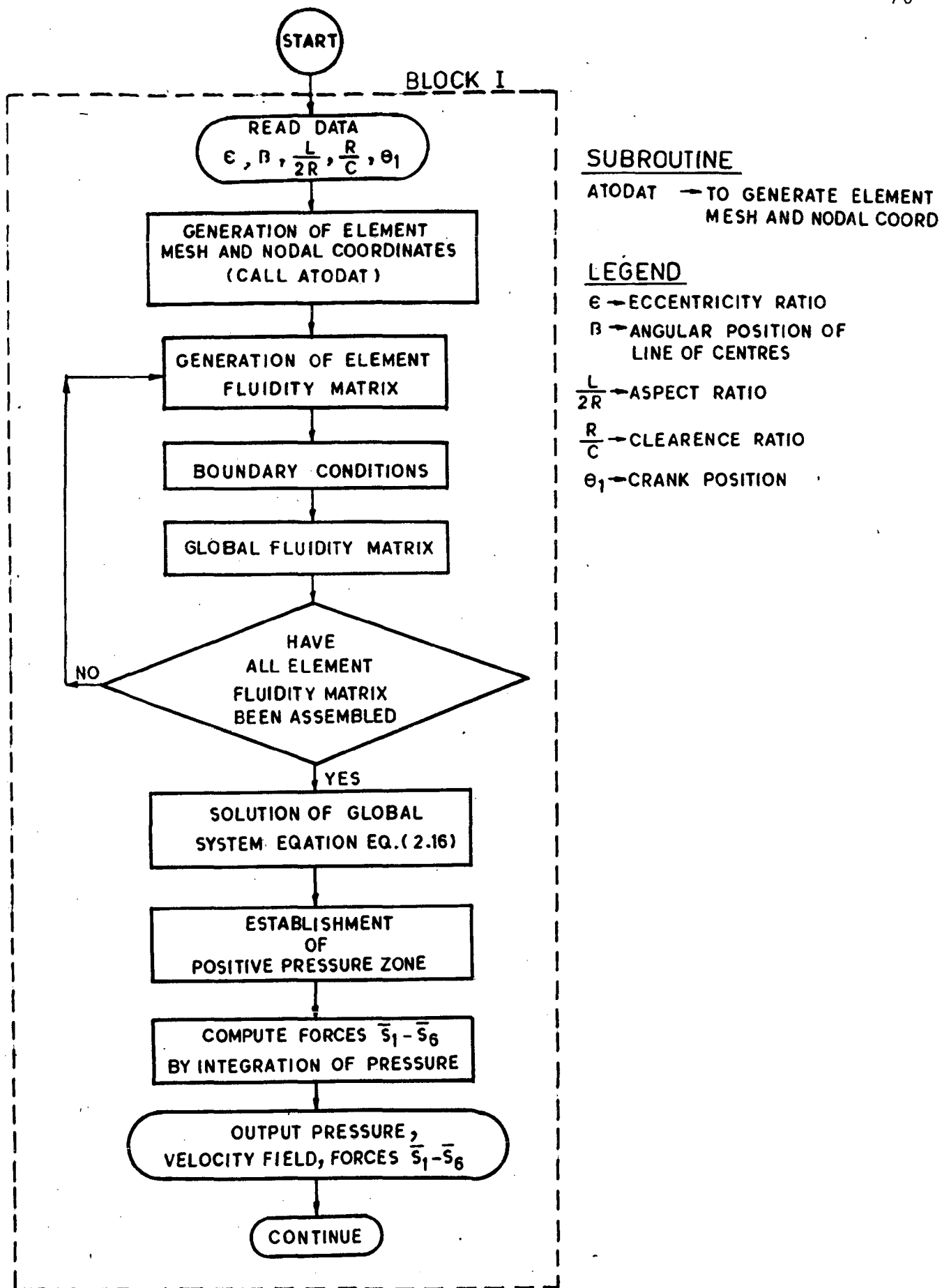


Fig. 5-1 b Flow diagram for the hydrodynamic problem

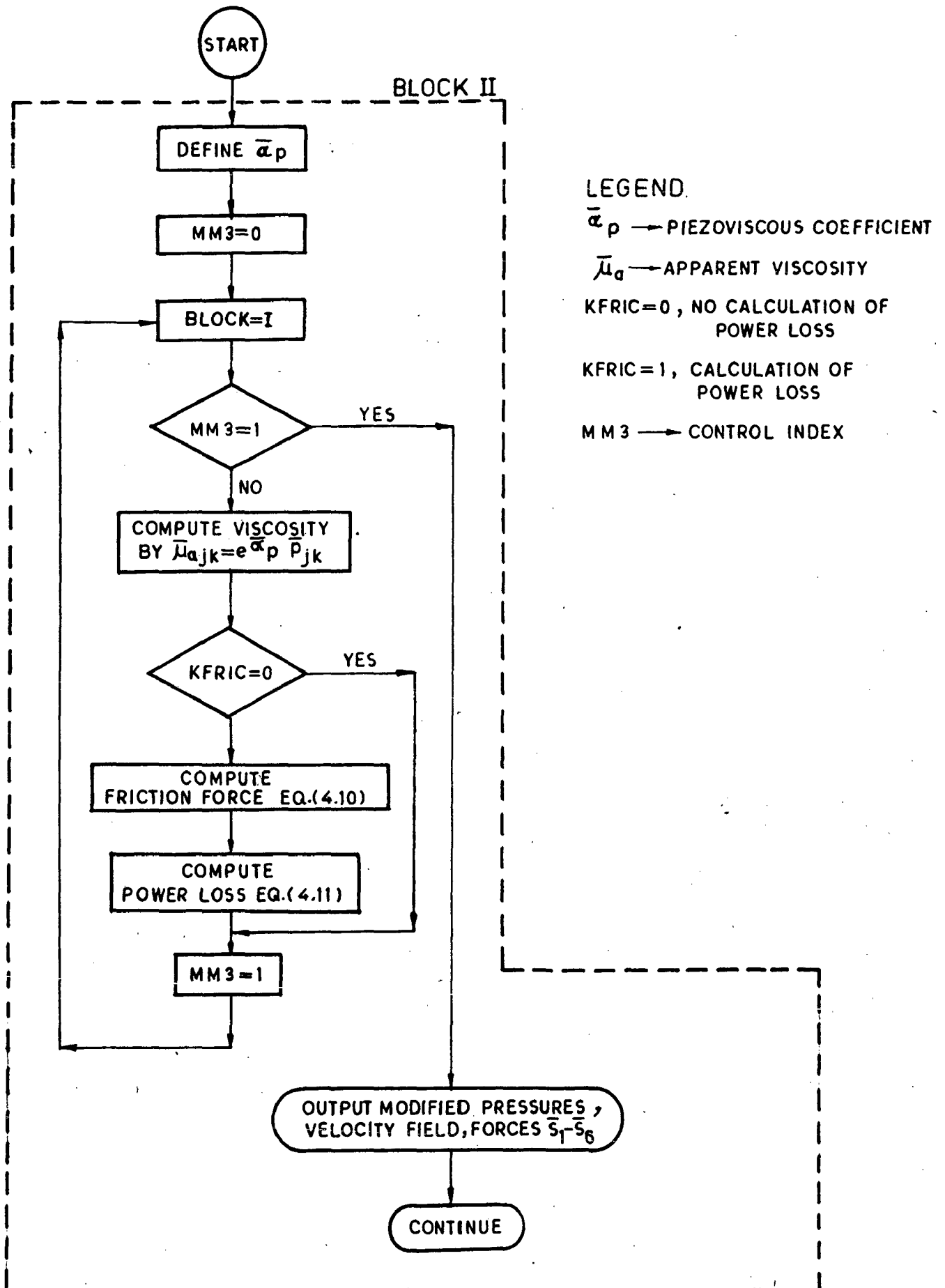


Fig. 5-2 Flow diagram for piezoviscous effect

field is obtained by solving Eq.(2.34) which is derived from energy equation, Eq.(2.24). After knowing the temperature and pressure, the apparent viscosity ($\bar{\mu}_{\Delta k}$) is calculated using the following relation

$$\bar{\mu}_{\Delta k} = \exp \{ \bar{\alpha}_p \bar{p}_{\Delta k} - \bar{\beta}_T (\bar{T}_{\Delta k} - 1) \} \quad (2.25')$$

The following method is used to solve Eq.(2.34) which yields temperature distribution in the flow field. To establish the temperature field in the fluid-film, the known velocity field (from BLOCK-I) is used to calculate the dissipation function $\bar{\phi}_v$ (Eq.2.33) and the convective terms (Eq.2.22). The nodal temperatures at the crank-pin surface (\bar{T}_c) are assumed to be constant (\bar{T}_c is not available in the literature) at a value somewhat higher than the oil supply temperature (89°C). The nodal temperatures at the bearing and fluid-film interface are also taken equal to the supply temperature (i.e., $\bar{T}_b = 1.0$) in the first iteration. The space or surrounding temperature (in which the bearing rotates) is assumed uniform and less than the supply temperature (i.e., $\bar{T}_s = 0.9$). From the specified boundary condition (Sec.2.5.2), the temperature in the fluid-film is obtained by solving the equation (2.34). When all the nodal (20 nodes) temperatures are known for each element, the nodal temperature

gradient ($\frac{\delta \bar{T}}{\delta \bar{r}} : \bar{r} = \bar{R}_i$) at the nodes on the bearing inner surface and in turn heat rate, Eq.(A-2.2), are calculated. The heat rate, which transfer from the bearing inner surface to the outer surface through conduction and the same heat rate from bearing outer surface to the surrounding by convection process is calculated in terms of \bar{T}_b , Eq.(A-2.6). By equating these two heat rates (Eq.A-2.2 and Eq.A-2.6), the new value of \bar{T}_b is calculated from the relation given in Appendix A-2, Eq.(A-2.7).

By using these calculated values of \bar{T}_b as the new boundary conditions, the equation (2.34) is again solved and heat rates are equated to obtain the new values of \bar{T}_b . To improve the convergence of the iteration, the following criteria is used for \bar{T}_b .

$$\bar{T}_b = W_x \bar{T}_b^{k-1} + (1-W_x) \bar{T}_b^k \quad (5.2)$$

where, W_x is the weighting factor ($W_x = 0.8$) and k is the iteration counter in Eq. (5.2). The convergence has generally been achieved in four to five iterations.

The new temperature field is thus obtained and corresponding to these temperatures, the viscosity value is modified for each Gaussian integration point. Using the modified viscosities, a new set of nodal pressure, velocity field and forces \bar{S}_1 to \bar{S}_6 is obtained from the global system equation (2.16). The flow diagram of the solution to include the effects of temperature and pressure on viscosity of lubricants is shown in BLOCK-III, Fig. 5.3.

5.1.1d Non-Newtonian Lubricants

To account for the viscosity variation for lubricants with nonlinear constitutive equation (non-Newtonian), the value of apparent viscosity ($\bar{\mu}_a$) is calculated either from any one of the non-Newtonian models (Eqs.2.17a-2.17g) or from the curve-fit model (Eq.2.20) based on experimental data [37]. These calculated values of ($\bar{\mu}_a$) are substituted in the integral expressions generating the element fluidity matrix (Sec.2.3).

The following procedure is used to obtain the apparent viscosity for the non-Newtonian lubricants.

The initial trial solution is obtained as described in BLOCK-I with $\bar{\mu}_a = 1$ (Newtonian lubricants) and the velocity field is

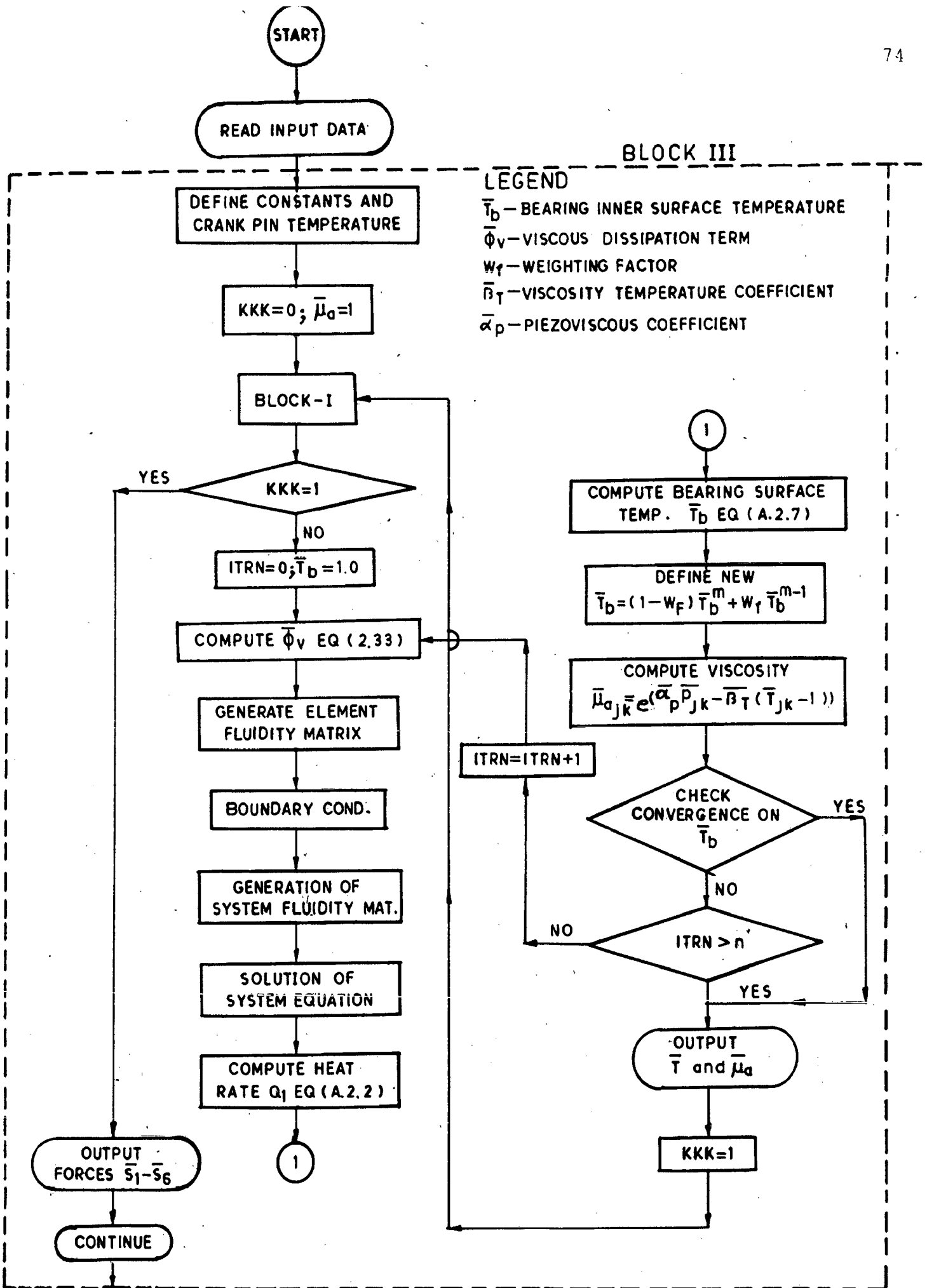


Fig. 5.3 Flow diagram for piezo-thermal effects

established. For this velocity field, the strain rate ($\dot{\bar{\gamma}}$) is calculated at each Gaussian integration point in each element using Eq.(2.18). For any selected non-Newtonian model (Eqs.2.17a-2.17g), the corresponding shear stress ($\bar{\tau}$) is calculated by Newton-Raphson method. The apparent viscosity is then obtained from the relation $\bar{\mu}_a = (\bar{\tau}/\dot{\bar{\gamma}})$, (Eq.2.19).

In the case of curve-fit model, for any selected oil (C- 2, Appendix A-1), a polynomial is fitted by the least square method between the viscosity and shear rate experimental data, Table-2.1, which is converted into nondimensional form. A fourth order polynomial is obtained to express the functional relationship between the non-dimensional values of viscosity and shear rate. Using the velocity field (known from the solution of BLOCK-I with $\bar{\mu}_a = 1$), the shear rate ($\dot{\bar{\gamma}}_{jk}$) occurring in the fluid-film element is then obtained and from the polynomial, the corresponding value of apparent viscosity ($\bar{\mu}_{a,jk}$) is computed. Once these updated values of apparent viscosity for each element are known, they are substituted in place of $\bar{\mu}_a = 1$ in the element equation and the updated pressure, velocity field and forces \bar{S}_1 to \bar{S}_6 are obtained. The corresponding flow diagram is shown in BLOCK-IV, Fig.5.4.

5.1.1e Misalignment of Axes

If the axes of the crank pin and the big-end bearing are not parallel, the expression of the film thickness must be modified to include the skew components σ and δ , it results a change in the radial coordinates of the nodal points. The expression of the film thickness is derived in Appendix A-5. The solution procedure given in BLOCK-I may be used for skewed axes case also.

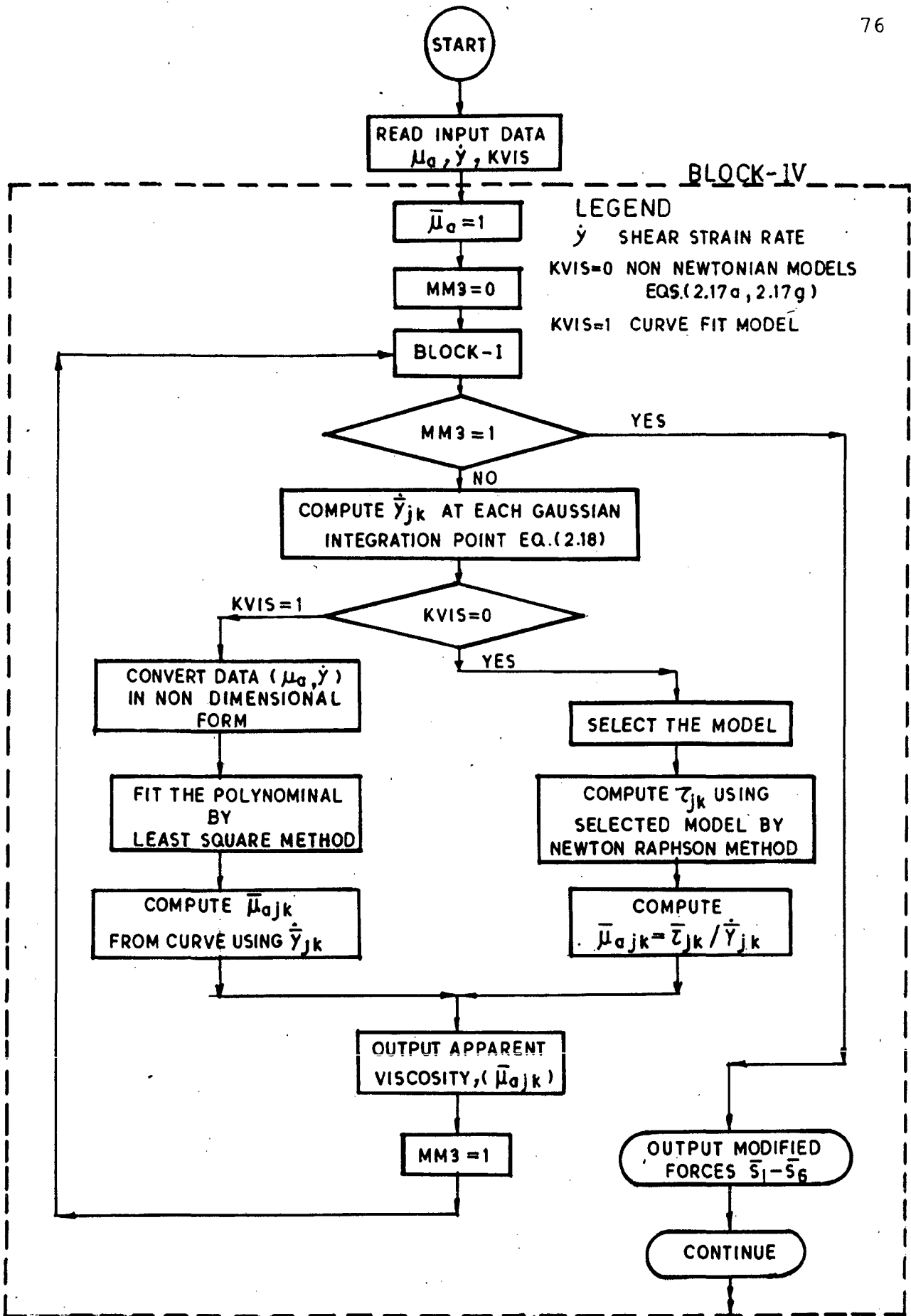


Fig. 5.4 Flow diagram for solution with non-Newtonian lubricants

5.1.2 Flexible Bearing

In case of EHD lubrication, the computer program has two main parts. The first part determines the pressure and velocity field (BLOCK-I, for isoviscous case, BLOCK-II for piezoviscous case, and BLOCK-III for piezo-thermal case) in the fluid-film, it is named here as the hydrodynamic part. The second part gives the nodal elastic displacements corresponding to the pressure field, it is named as the elasticity part.

In the following subsection, the procedure to obtain the nodal displacement in the flexible body of the bearing is described. Solution algorithm for hydrodynamic part has been described in Sec.5.1.1.

Elasticity Part

In this case, the bearing body is discretized in such a manner that all the nodes lying at fluid-film and bearing body interface match to each other in both (fluid-film or bearing body) discretization systems. The elasticity matrix, element fluidity matrix and the element nodal traction force vector are obtained using the analysis described in Chapter 3. Then after applying the boundary conditions (Sec.3.3) all the element matrices and vectors are stored on computer disk/tape. The frontal solution method is used which yields the nodal displacements (\bar{d}_r , \bar{d}_θ , \bar{d}_z) in three directions. It is observed that the nodal displacements (\bar{d}_θ , \bar{d}_z) along circumferential and axial direction are much smaller in comparison to the radial displacement (\bar{d}_r). Therefore, only the nodal radial displacements (\bar{d}_r) at the fluid-film and bearing shell interface are added algebraically to the radial coordinates of the fluid-film element nodes. For the EHD isoviscous, EHD piezoviscous and ETHD

lubrication cases, the flow diagram is shown in BLOCK-V, Fig.5.5.

5.2 INTEGRATION SCHEME FOR THE EQUATIONS OF MOTION OF THE BEARING CENTRE

The bearing centre orbit requires the bearing centre instantaneous position (ϵ_1, β_1) and velocities $(\dot{\epsilon}_1, \dot{\beta}_1)$ at i^{th} interval of crank rotation. The velocities $(\dot{\epsilon}_1, \dot{\beta}_1)$ are obtained by solving the force balance (i.e., Eqs.4.14, equations of motion) by using the known force components \bar{S}_1 to \bar{S}_6 . Force components are known from the solution procedure presented in BLOCK-I,II,III,IV or V. The following time marching scheme (or integration scheme) to obtain the bearing centre orbit is found to work well.

5.2.1 Intergration Scheme

Let ϵ_{i-1} and β_{i-1} are the coordinates of the bearing centre corresponding to the quasi-static equilibrium condition of bearing under the external load at the i^{th} interval of crank rotation which are obtained as given in Appendix A-6. The scheme works as follows:

Step 1. To begin with, the initial input data are given as $\epsilon_1 = \epsilon_{i-1} + \delta\epsilon$, $\beta_1 = \beta_{i-1}$ ($\beta_{i-1} = \alpha_1 + \theta_{i-1}$, Fig.4.4), $\theta_{1,1}$, $\dot{\epsilon}_1 = \dot{\beta}_1 = \ddot{\epsilon}_1 = \ddot{\beta}_1 = 0$, $\bar{\mu}_1 = 1$ and time increment in terms of crank rotation interval ($\delta\theta_1$) for any crank angle position defined by i^{th} interval. The solution may be started at any arbitrary crank angle position (i.e., i^{th} interval) and with any values of ϵ_1 and β_1 . But it was found, that a fast convergence is possible, if for any particular crank angle $\theta_{1,1}$, the values of $\epsilon_1 = \epsilon_{i-1} + \delta\epsilon$ and $\beta_1 = \beta_{i-1}$ are used. The hydrodynamic part, BLOCK-I, is first solved.

To include other effects, the program runs through BLOCK- II, III, IV or V which give modified values of force components \bar{S}_1 to \bar{S}_6 .

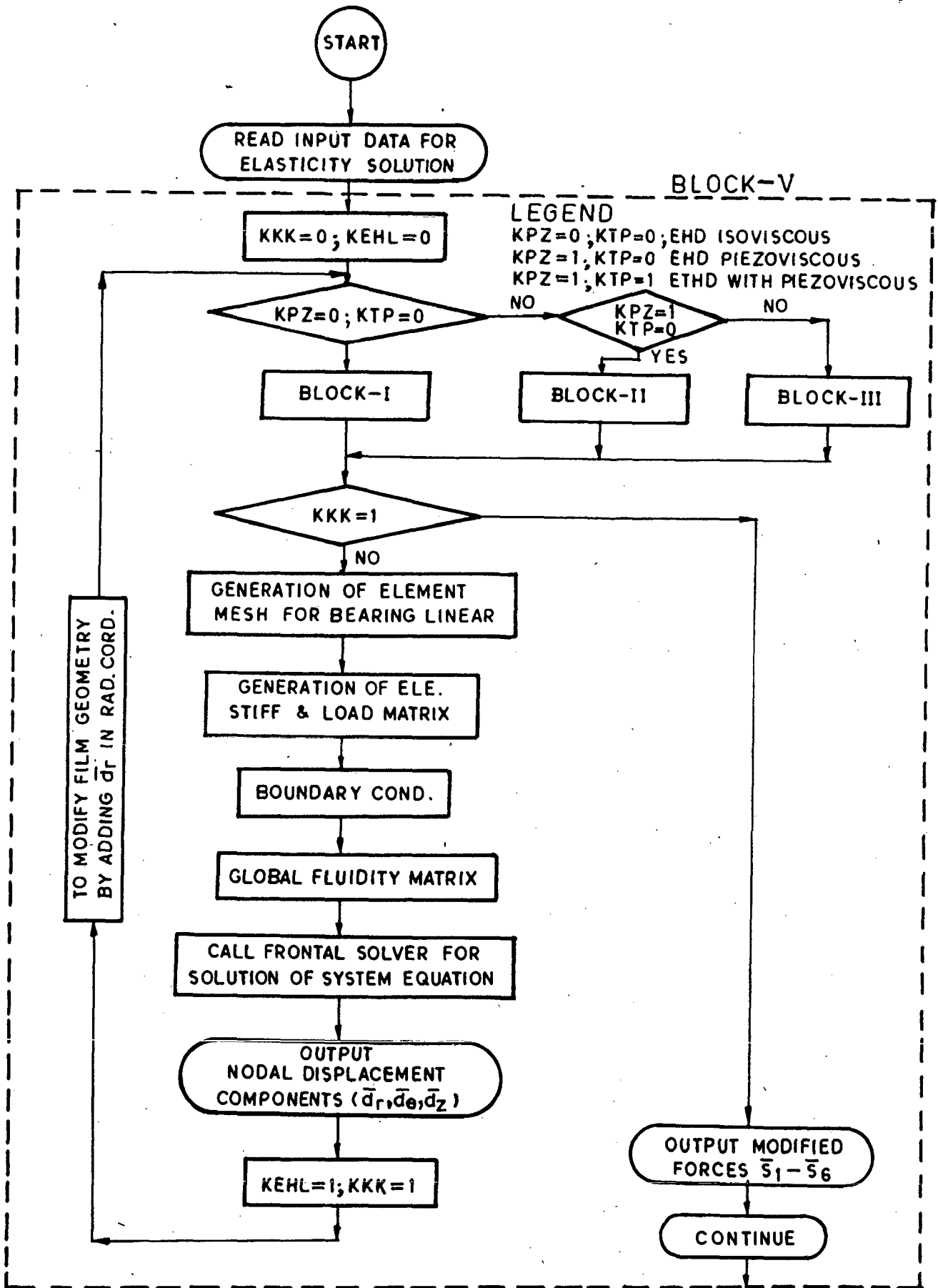


Fig. 5-5 Flow diagram for solution of the elastic problem

Step 2. The values of $\dot{\bar{e}}_1$, $\dot{\bar{\beta}}_1$ are calculated using the equations of motion (4.14),

$$\dot{\bar{e}}_1 \bar{S}_2 + \dot{\bar{\beta}}_1 \bar{S}_3 = - (\bar{W}_m + \bar{S}_1) \quad (4.14a')$$

$$\dot{\bar{e}}_1 \bar{S}_5 + \dot{\bar{\beta}}_1 \bar{S}_6 = - (-\bar{W}_n + \bar{S}_4) \quad (4.14b')$$

Step 3 The eccentricity ratio (\bar{e}_{i+1}^P), angle of line of centres (β_{i+1}^P) and the velocities ($\dot{\bar{e}}_{i+1}^P$, $\dot{\bar{\beta}}_{i+1}^P$) are predicted using Euler's formula (only for one initial interval i.e., the $(i+1)^{th}$ interval).

$$\bar{e}_{i+1}^P = \bar{e}_i + \delta\bar{t} \dot{\bar{e}}_i \quad (A-3.5')$$

$$\dot{\bar{e}}_{i+1}^P = \dot{\bar{e}}_i + \delta\bar{t} \ddot{\bar{e}}_i = \dot{\bar{e}}_i \quad (\text{in starting only})$$

where, $\delta\bar{t}$ is the non-dimensional time increment, ($\delta\bar{t} = (\Omega \times \delta t) = \delta\theta_1$) For crank angle θ_{1i+1} ($\theta_{1i+1} = \theta_{1i} + \delta\theta_1$), using the predicted values \bar{e}_{i+1}^P , β_{i+1}^P , the hydrodynamic part is solved. The positive pressure zone is established using $\dot{\bar{e}} = \dot{\bar{e}}_{i+1}^P$ and $\dot{\bar{\beta}} = \dot{\bar{\beta}}_{i+1}^P$ in Eq.(5.1). This yields a new set of force components \bar{S}_1 to \bar{S}_6 for crank angle θ_{1i+1} . The values of $\dot{\bar{e}}_{i+1}$ and $\dot{\bar{\beta}}_{i+1}$ are then calculated from Eqs.(4.14a'-4.14b'). At this stage, corresponding to the calculated values of $\dot{\bar{e}}_{i+1}$, $\dot{\bar{\beta}}_{i+1}$, the values of \bar{e}_{i+1} , β_{i+1} are corrected for the same position of crank angle (θ_{1i+1}) by using the following Euler-Cauchy's corrector formula [34].

$$\bar{e}_{i+1}^c = \bar{e}_i + (1/2) \delta\bar{t} (\dot{\bar{e}}_{i+1}^P + \dot{\bar{e}}_i) \quad (A-3.4')$$

$$\beta_{i+1}^c = \beta_i + (1/2) \delta\bar{t} (\dot{\bar{\beta}}_{i+1}^P + \dot{\bar{\beta}}_i)$$

The values of accelerations are also calculated using the backward difference formula [25].

$$\ddot{\bar{e}}_{i+1} = (\dot{\bar{e}}_{i+1}^c - \dot{\bar{e}}_i) / \delta\bar{t} \quad (A-3.6')$$

$$\ddot{\bar{\beta}}_{i+1} = (\dot{\bar{\beta}}_{i+1}^c - \dot{\bar{\beta}}_i) / \delta\bar{t}$$

For convergence of solution, using these corrected values of

$\bar{\epsilon}_{i+1}$ and $\bar{\beta}_{i+1}$, the whole process of solution is repeated unless the respective difference between the values of ϵ and β obtained from the previous and current iteration become smaller than the predefined tolerance limit. For convergence, the following tolerance limit is defined.

$$\left| \frac{\epsilon_i^n - \epsilon_i^{n-1}}{\epsilon_i^n} \right| \leq 10^{-3} \quad \text{and} \quad \left| \frac{\beta_i^n - \beta_i^{n-1}}{\beta_i^n} \right| \leq 10^{-2} \quad (5.3)$$

where, n is the current iteration number at i^{th} crank interval. The iteration generally is terminated when $n \geq 4$.

Step 4 Once the time marching process reaches the second point ($i+1$), it is possible to operate with higher-order prediction formula, such as Euler-Cauchy's predictor formula [34]. The next values of ϵ_{i+2}^p , β_{i+2}^p , $\dot{\epsilon}_{i+2}^p$ and $\dot{\beta}_{i+2}^p$ are predicted as

$$\begin{aligned} \epsilon_{i+2}^p &= \epsilon_i + 2 \delta t \dot{\epsilon}_{i+1} \\ \dot{\epsilon}_{i+2}^p &= \dot{\epsilon}_i + 2 \delta t \ddot{\epsilon}_{i+1} \end{aligned} \quad (A-3.3')$$

Using this scheme (flow diagram, Fig.5.6), a complete or a partial orbit of the big-end bearing centre for any loading case can be obtained. The time process is extended even beyond two revolutions (720°) till the orbit starts repeating itself into a limit cycle.

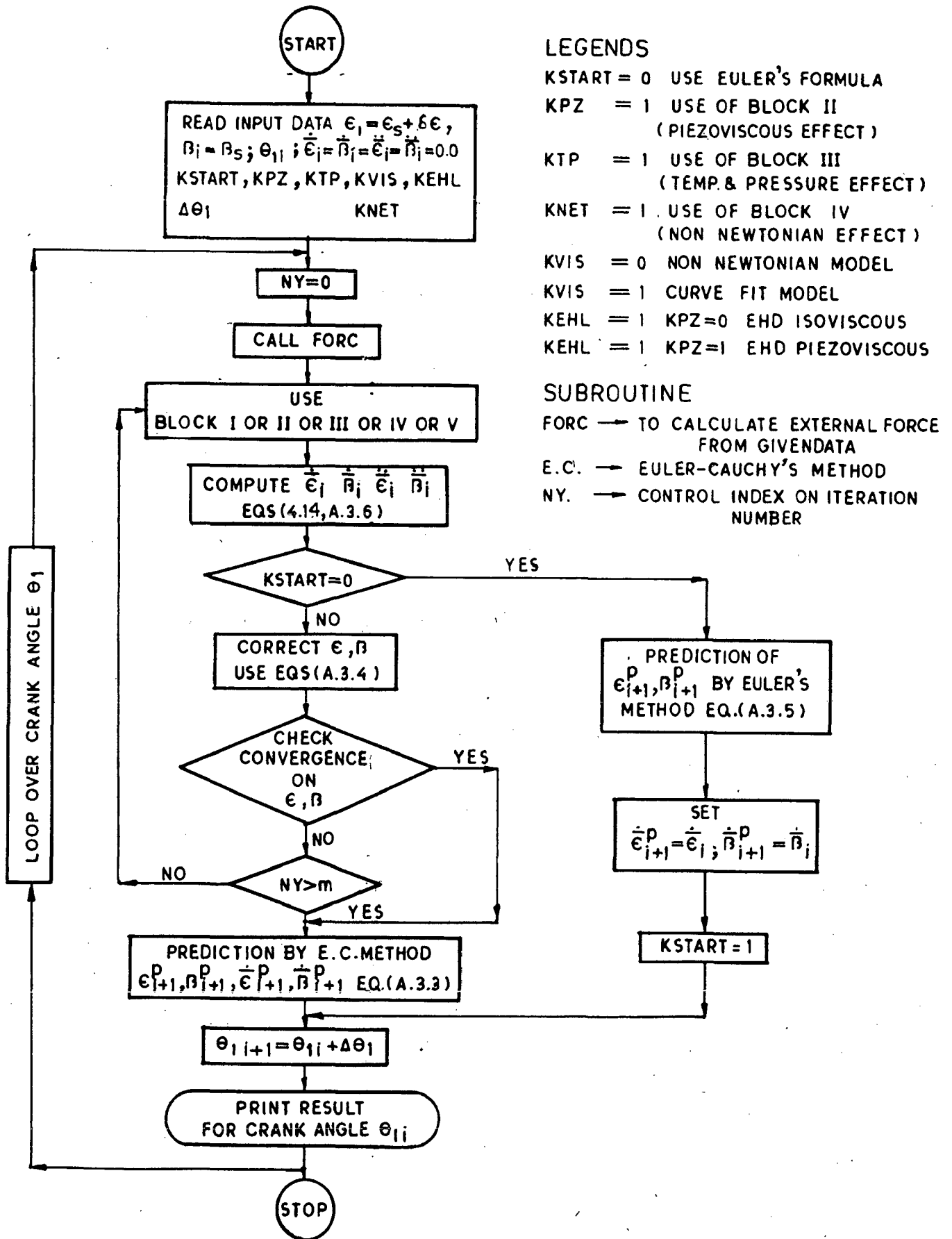


Fig. 5-6 Flow diagram for the time marching scheme

CHAPTER-6

RESULTS AND DISCUSSIONS

The big-end bearing, as one of the most important components of the internal combustion engine and subjected to a complex dynamic loading, has been an interesting problem for investigation. It is also one of the most practical problems of the bearing under dynamic loading. In the present work, although, the problem is quite involved and non-linear in nature, the author has tried to obtain its solution in a general way. The momentum and the continuity equations are used to represent the flow-field; the full (2π) film is discretized for analysis, and to account for the cavitation, all the resultant negative pressures are set equal to zero. Galerkin's technique is used for finite-element formulation and Euler-Cauchy's predictor-corrector method is used for the time marching scheme, all of which are described in detail in the foregoing Chapters. This Chapter deals with the computed results and the discussions thereof.

The bearing centre orbits with respect to the crank pin centre and fixed axis along engine cylinder axis, are calculated for two revolutions of the crank for a four stroke engine. The orbit also gives the variation of the minimum film thickness as a function of crank rotation in the rigid bearing case. To validate the computer program, the static characteristics of the circular bearing are first calculated and compared with the existing data available in the literature.

The computed results are presented in two main sections. The first section includes the results of the big-end bearing with rigid

body accounting for effects of various parameters on the performance characteristics of the big-end bearing, Table-6.1. The second section includes the results of the bearing considering body deformation and the dependence of viscosity on pressure and temperature, both. The required computational CPU time for all cases is also compiled.

Table- 6.1

Studies for the rigid big-end bearing

Cases* studied	1	2	3	4	5	6
Bearing ** characteristics presented	a,b,c	a,b,c,d	a,b,c,d,e	a,b,c	a,b,c	a,b,c

- * 1. isoviscous lubricant,
 2. piezoviscous lubricant,
 3. piezo-thermal effects on viscosity,
 4. non-Newtonian lubricants,
 5. ungrooved bearing with parallel axes,
 6. ungrooved bearing with skewed axes.

- ** a. bearing centre orbit,
 b. variation of the maximum film pressure,
 c. variation of the minimum film thickness,
 d. power loss
 e. the maximum temperature rise in the fluid-film at various crank angles.

In the second section which includes the deformation of the bearing body, the following results for the big-end bearing are obtained and presented for a finite crank rotation. They are bearing centre locus, minimum film thickness, maximum radial deformation and temperature rise.

Results are also presented to show that Euler-Cauchy's predictor-corrector method for the time marching scheme is more suitable for the present problem than higher-order predictor methods, such as Runge-Kutta, Adams-Moulton methods.

6.1 SAMPLE PROBLEM

The results presented in this study are for the Ruston-Hornsby 6 VEB-X, Mk-III engine connecting-rod big-end bearing for which the input data and results are available in the literature for comparison. It is most analysed bearing in the literature [4,6,10,23,24,42,45,50,54,56,60]. This bearing has a central circumferential groove as shown in Fig.1.4. Using the symmetry about the central plane, only one of the lands of the bearing subjected to one half of the given load is discretised for the computation of the bearing characteristics. Details of the bearing geometry and the loading are given in several references (for instance Campbell et al [10]) and are briefly summarized in Appendix A-4. For the bearing analysed here, the dynamic load is given in terms of its two perpendicular components at intervals of crank rotational angle for two revolutions [10], but if the geometry of the engine (connecting-rod length, crank radius, cylinder bore, masses of the reciprocating and rotary parts etc.) and the cylinder gas pressure are known, the dynamic load components can be calculated in accordance to the analysis presented in Sec.4.1 and for which a subroutine is prepared. In the present problem, the bearing load components with reference to the engine cylinder axis [10] are converted to resultant force vector in SI units and is shown as load diagram in Fig.4.2.

6.2 DISCRETIZATION OF FLUID-FILM

The fluid-film domain and the bearing body are divided into 48 isoparametric elements each. Keeping in view the computer storage requirement, a $12 \times 4 \times 1$ grid consists of 12 circumferential and 4 axial divisions, Fig.6.1. The bearing is divided into four circumferential zones. The size of the elements in each zone was decided on the basis of the anticipated pressure, using the smallest size in the zone where the maximum pressure is expected to occur. The elements are equal in size in each respective zone and their numbers vary from one zone to the other. In each element of the fluid-film, the velocity components and temperature are approximated by quadratic variations (20 nodes), the pressure in the fluid-film and the deformation in the bearing body by linear variations (8 nodes), Fig.6.2.

6.3 SELECTION OF THE METHOD FOR NUMERICAL INTEGRATION OF THE EQUATIONS OF MOTION OF THE BEARING CENTRE

There are various numerical integration methods available which can be used to obtain the bearing centre orbit. Euler's method is suitable only for small time intervals, hence it is not computationally economical. The higher-order predictor methods (for instance, Runge-Kutta or Adams-Moulton) are more accurate but were not found suitable for the present type of problem.

The trials indicated that Euler-Cauchy's predictor-corrector method can be used successfully with good accuracy. The values of ϵ, β obtained by Euler-Cauchy's predictor-corrector method were compared with those obtained by using a combination of Runge-Kutta (up to initial five points) and higher-order predictor-corrector formula due to Adams-Moulton [25] at 10° interval for a finite crank rotation, Table-6.2. Table-6.2 shows that after the crank angle $\theta_1 =$

Table-6.2

Comparison of the results obtained by Euler-Cauchy's predictor-corrector and Runge-Kutta-higher-order predictor-corrector methods

Crank angle θ_1	Euler-Cauchy's Method			R-K ^a , P-C ^b Method			Remark
	ϵ	β	CPU Time (min.)	ϵ	β	CPU Time (min.)	
70	0.87629	-28.40	-	0.87629	-28.40	-	
80	0.87632	-28.72	2	0.88395	-27.20	4	R-K method
90	0.90725	-24.29	2	0.88883	-26.11	4	R-K method
100	0.91316	-21.27	2	0.89633	-24.07	4	R-K method
110	0.91704	-19.22	2	0.90481	-21.39	4	R-K method
120	0.92193	-16.74	2	0.91250	-18.52	4	R-K method
130	0.92715	-13.87	2	0.91917	-15.48	2	P-C method
140	0.93203	-10.83	2	0.92525	-12.30	2	P-C method
150	0.93657	-7.67	2	0.93071	-9.04	2	P-C method
160	0.94045	-4.40	2	0.93524	-5.69	2	P-C method
170	0.94369	-0.99	2	0.93899	-2.20	2	P-C method
180	0.94645	+2.56	2	0.94232	+1.42	3	P-C method
190	0.94898	6.23	2	0.94513	5.20	2	P-C method
200	0.95135	10.06	2	0.94774	9.11	2	P-C method
210	0.95344	14.04	2	0.95006	13.16	3	P-C method
220	0.95532	18.20	2	0.95220	17.39	2	P-C method
230	0.95703	22.54	2	0.95397	21.79	2	P-C method
240	0.95831	27.08	2	0.95548	26.39	2	P-C method
250	0.95909	31.93	2	0.95660	31.24	2	P-C method
260	0.95952	37.19	2	0.95726	36.44	3	P-C method

^a Runge-Kutta method, ^b Higher-order predictor-corrector method.

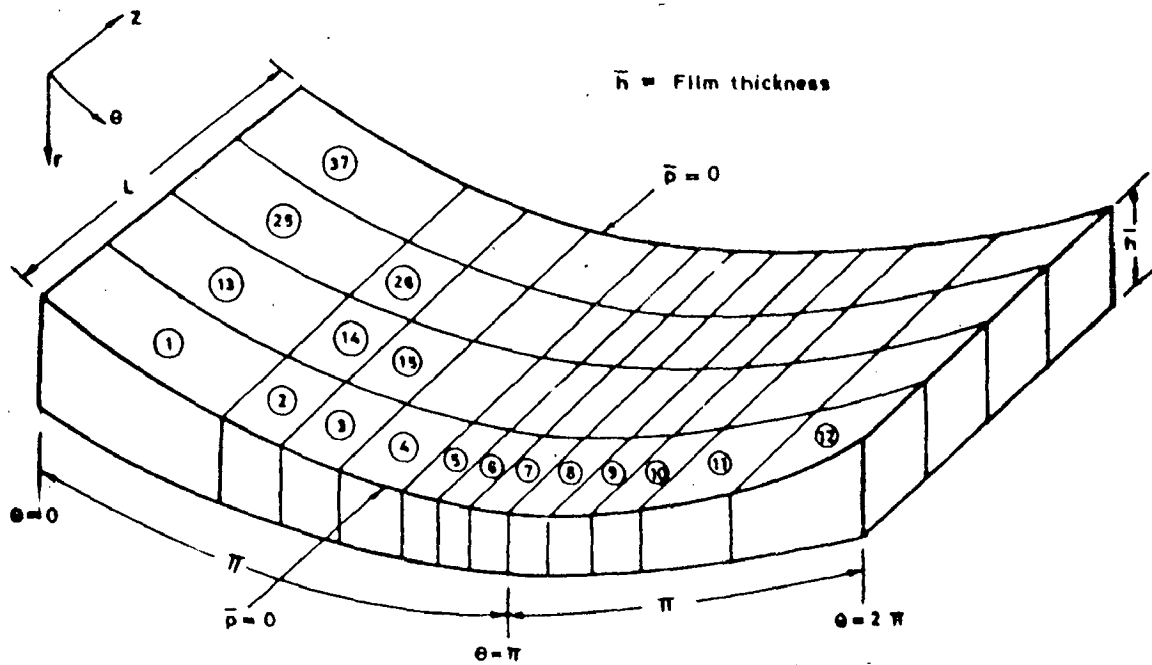


Fig. 6.1 Discretization of a symmetric half of the bearing (One land)

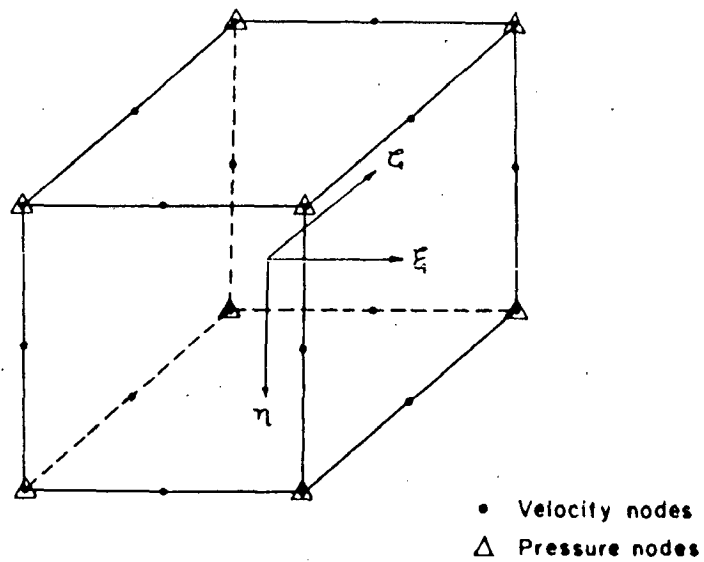


Fig. 6.2 Element

180°, both the (Euler-Cauchy and combination of Runge-Kutta, Adams-Moulton) methods give almost same values of ϵ and β . Higher-order methods (Runge-Kutta or Adams-Moulton or combination of both), though attractive, are found computationally more expensive and also give unstable results in the segments of rapid change of force vector. This is observed by the author and also by Shelly[60]. Fantino and Frene [18] have mentioned that Runge-Kutta method creates difficulties of convergence for EHD (elastohydrodynamic) lubrication problems. Hence, it was decided to use the Euler-Cauchy's predictor-corrector method for the time marching scheme in this thesis.

6.4 RESULTS AND DISCUSSIONS

In this section the computed results are presented and discussed. They are compared with each other to highlight the effects of various parameters and also with the existing results wherever necessary. The authenticity of the computer program is established first.

Using the analysis and the solution algorithm presented in the forgoing Chapters, a general computer program was developed. To authenticate the algorithm and the computer program, the static characteristics of the cylindrical hydrodynamic journal bearing were computed. These characteristics (i.e., Sommerfeld number (S), attitude angle (θ_m)) of the plain cylindrical bearing are compared with those of Pinkus [51] and Raimondi [57] in Table-6.3; they compare well.

To compare the results of plain cylindrical bearing with non-Newtonian lubricants under static condition, the load capacity (\bar{W}_s) of the plain bearing using $\epsilon = 0.2, 0.4, 0.6, 0.8$, and cubic shear stress law (Eq. (2.17a), with $K = 0.58$) were computed and checked with the experimental results [67]. Fig.6.3 shows good agreement and validates the computer program involving the nonlinear behaviour

Table-6.3

Static performance of circular bearing (aspect ratio = 1.0) and its comparison with the data available in the literature

e	S			θ_m		
	+	++	+++	+	++	+++
0.2	0.643	0.632	0.631	73.17	74.00	74.02
0.4	0.264	0.261	0.264	62.09	62.00	63.10
0.6	0.123	0.120	0.121	50.36	50.00	50.58
0.8	0.0453	0.0448	0.0446	36.28	36.00	36.24

+ Present Analysis

S - Sommerfeld number

++ Pinkus [51]

+++ Raimondi and Boyd [57]

θ_m - Attitude angle

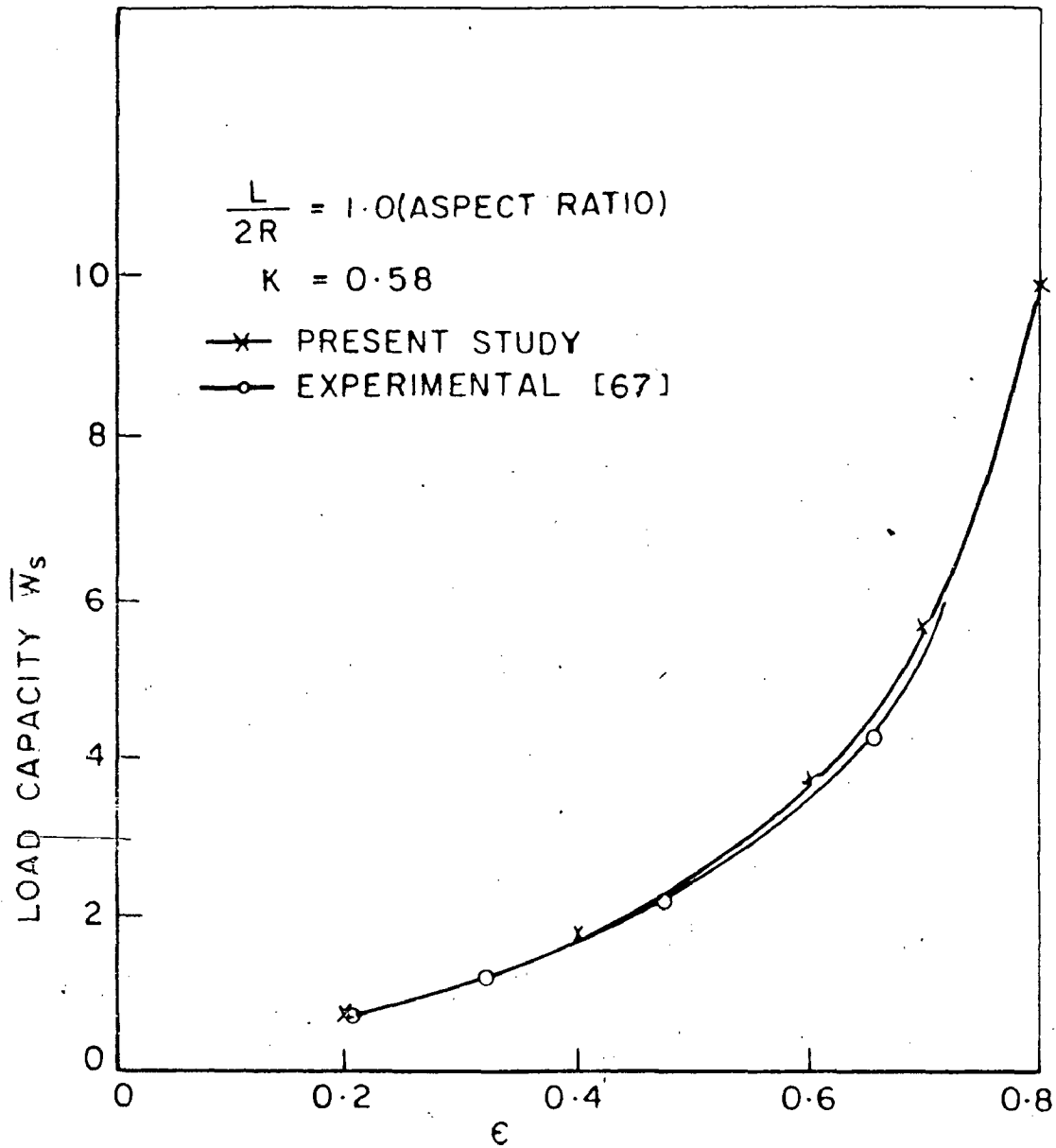


Fig. 6.3 Comparison of load capacity for non-Newtonian lubricants using cubic shear stress law (static load)

of the lubricant.

6.4.1 Rigid Bearing with Isoviscous Lubricants

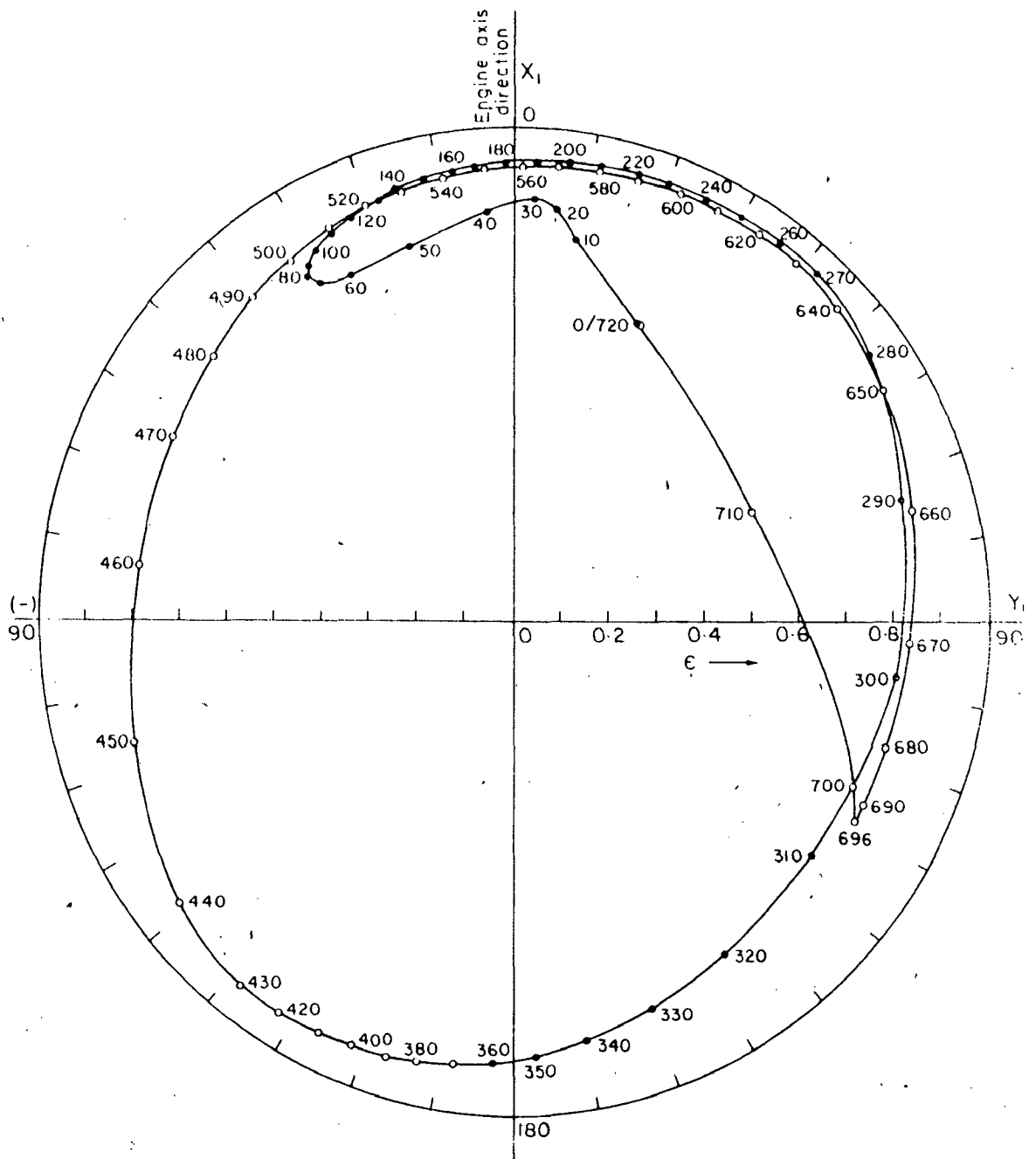
Performance of the big-end bearing, in terms of its bearing centre orbit, minimum film thickness and maximum film pressure for one complete duty cycle, are obtained for isoviscous lubricants considering the bearing body as rigid. The results are summarized below;

6.4.1a Bearing Centre Orbit:-

Fig. 6.4 gives the bearing centre orbit of the big-end bearing subjected to the dynamic load with respect to the crank pin centre, Fig.4.2. The complete bearing centre orbit is obtained by using the Euler-Cauchy's predictor-corrector method (Appendix A-3). From the calculations, the maximum eccentricity ratio is found as $\epsilon = 0.95341$ and the corresponding value of β is 41.83° . This value of ϵ occurs at $\theta_1 = 270^\circ$ crank angle, with reference to the top-dead-centre (TDC) at $\theta_1 = 0^\circ$; $0^\circ < \theta_1 < 180^\circ$ crank rotation represents the expansion stroke of the engine. The computed orbit, Fig. 6.4, is drawn with reference to a fixed axis along the engine cylinder axis. The orbits, Fig.1.2, given in the literature (for instance Campbell et al [10]) are drawn with reference to connecting-rod axis. When the points of the computed orbit are transformed with reference to the connecting-rod axis, it is found that the transformed orbit compare very well to the orbits of Fig.1.2.

The minimum film thickness or maximum eccentricity ratio occurs at 270° crank angle and does not occur at 10° crank angle at which the load is maximum, Fig. 4.2. This condition may be explained as follows:

In a dynamically loaded bearing if the angular velocity of the



— Fig. 6.4 Bearing centre orbit (Isoviscous case)
(Force variation, Fig. 4.2)

(The figure on curve represent the crank angular position
in degrees from t. d. c.)

relative motion of the bearing and the rotational velocity of the load vector are N_1 and N_L , then the approximate load capacity of the bearing is directly proportional to the effective velocity of bearing ($N_1 - 2N_L$).

At 270° crank angle, the load vector rotates at a speed large enough in the same direction as does the bearing (i.e., clockwise, Fig.4.2), hence, the effective velocity of the bearing decreases and in turn the load capacity of the bearing is considerably reduced in the vicinity of 270° crank angle, whereas at 10° crank angle, the load rotates in the direction opposite to that of the bearing, so the load capacity of the bearing increases and in turn the eccentricity ratio is obtained as smaller. A similar effect of increase in load capacity is observed during the crank rotation from 670° to 60° where the load vector rotates in direction opposite to that of the bearing, Fig.4.2.

6.4.1b Maximum Film Pressure:-

Fig.6.5 shows the values of the peak pressure in the fluid-film for two revolutions of the crank shaft. The peak pressures are plotted as a function of crank angle. The maximal value (i.e., the largest of the peak value) of film pressure, hereafter called as the maximum film pressure, in rigid bearing case is found to be 38.61 MPa which occurs at the crank angle position 180° after TDC. For the same big-end bearing geometry, Goenka [24] has obtained the value of maximum film pressure as 34.40 MPa which is about 11% smaller than the value (38.61 MPa) obtained in the isoviscous case.

6.4.1c Minimum Film Thickness:-

Fig.6.6 shows the minimum film thickness variation with time or crank rotation. In the isoviscous case of rigid bearing, the minimal

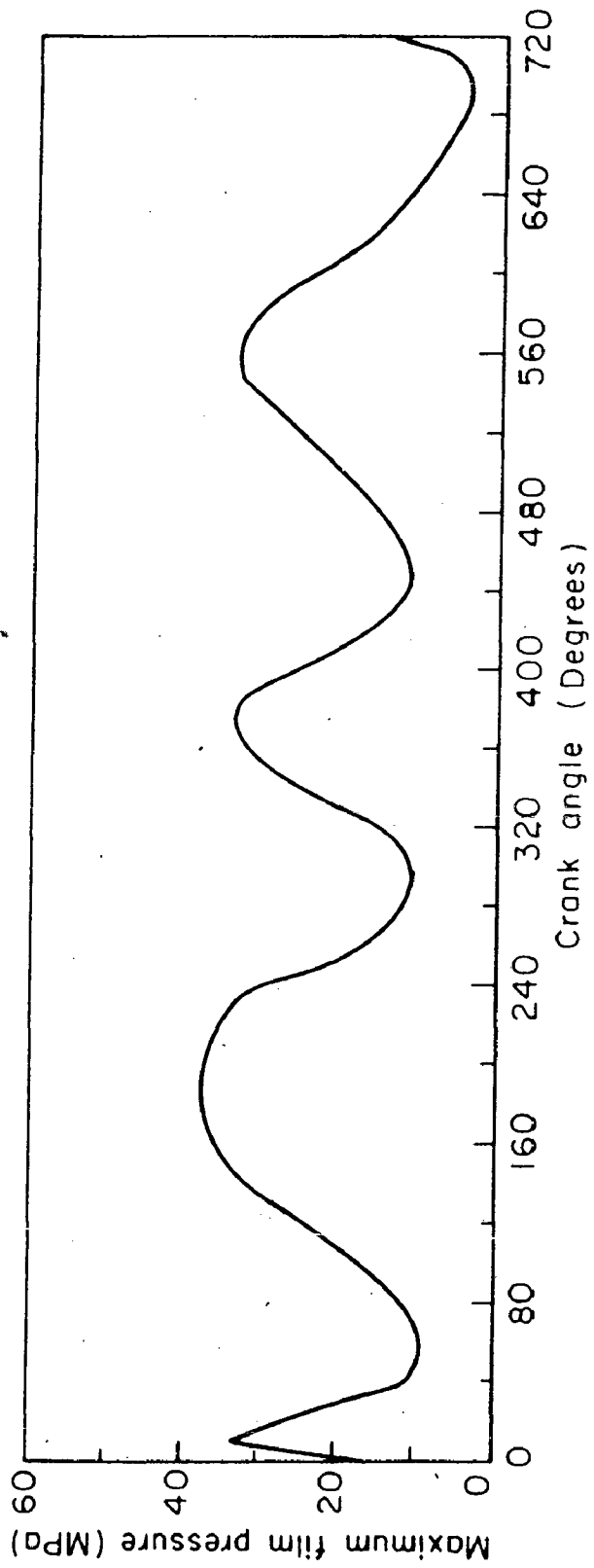


Fig. 6-5 Variation of maximum film pressure
(Rigid bearing, isoviscous case)

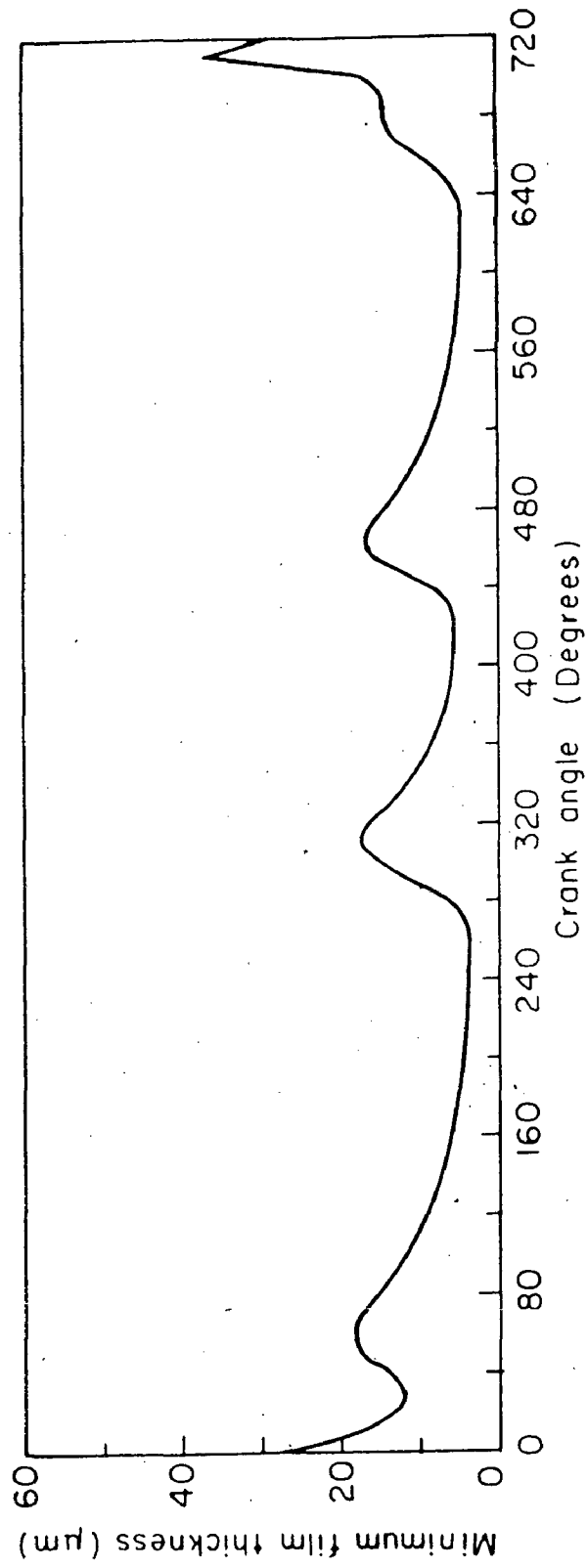


Fig. 6.6 Variation of minimum film thickness
(Rigid bearing, isoviscous case)

value (i.e., the smallest of the minimum value of film thickness), hereafter called as the minimum film thickness, is obtained as $3.85\mu\text{m}$.

The other reported values of the minimum film thickness along with the present value for the 6VEB-X engine big-end bearing are presented in Table-6.4 for comparison. Table-6.4 indicates that the value of the minimum film thickness in the present study ($3.85\mu\text{m}$) lies in the range of the values of the minimum film thickness obtained by others [10]. From these observations, it can be concluded that the analysis, the solution algorithm and the computer program are all valid.

The value of minimum film thickness does not occur at those crank angles where the bearing load is maximum (e.g., at $\theta_1 = 10^\circ$ or 360° , Fig.4.2), but it occurs at crank angle 270° . In the literature [10], the crank position at which the minimum film thickness occurs is also reported in the vicinity of 270° crank angle, Table-6.4.

6.4.2 Rigid Bearing with Piezoviscous Lubricants

Performance of the same big-end bearing considering the effect of pressure on viscosity of lubricants is obtained in terms of the bearing centre orbit, variations of the peak pressure, the minimum film thickness and the power loss. These results are also compared with those obtained in the isoviscous case 1, Table-6.1. For viscosity modification, the value of piezoviscous coefficient $\bar{\alpha}_p$ is taken as $0.02133 (1.5 \times 10^{-9} \text{ Pa}^{-1})$ in Eq.(4.12). The results are as follows:

6.4.2a Bearing Centre Orbit:-

Fig.6.7 shows the bearing centre orbit of the big-end bearing having piezoviscous lubricants. The shape of the orbit is almost

Table-6.4

Comparison of the minimum film thickness obtained in the isoviscous case with the experimental and theoretical values available in the literature for the Ruston-Hornsby 6 VEB-X, MK-III engine big-end bearing

Sr.No.	Source	Remarks	\$	#
1.	<u>Glacier Metal Co.</u>	Experimental	2.79*	240
	From R & H 6VEB engine	Experimental	3.30*	270
2.	Booker: short bearing	Graphical	5.58*	277
	Block: finite bearing	Graphical	3.30*	274
4.	Martin-Booker: short bearing	Computed	5.84*	-
5.	Booker: short bearing	Computed	5.84*	271
6.	Booker: finite bearing using Warner solution	Computed	2.31*	271
7.	Blok: finite bearing, Herrebrugh & Moes	Computed	2.90*	280
8.	Horsnell: finite bearing	Computed	5.44*	273
9.	Lloyed: finite bearing	Computed	4.47*	289
10.	<u>General Electric Co., U.K.</u>		**	
	Ritchie: finite bearing	Computed	3.63**	-
	Ritchie: optimised short bearing	Computed	3.30	-
11.	<u>General Motors Research Co.</u>		**	
	Goenka: FEM	Computed	3.48**	-
	Goenka: rapid curve fit program	Computed	3.48	-
12.	<u>Glacier Metal Co.</u>		**	
	Jones: finite bearing	Computed	3.56**	-
	Jones: with film history	Computed	2.29	-
13.	<u>University of Sussex</u>		**	
	Dede: finite bearing, mass effect	Computed	4.45	-
	Dede: 1D solution, mass effect	Computed	3.73**	-
14.	Present study	Computed	3.85	270

* Campbell et al [10], ** Martin [45], \$ Minimum film thickness (μm)
Crank shaft position after T.D.C. at minimum film thickness

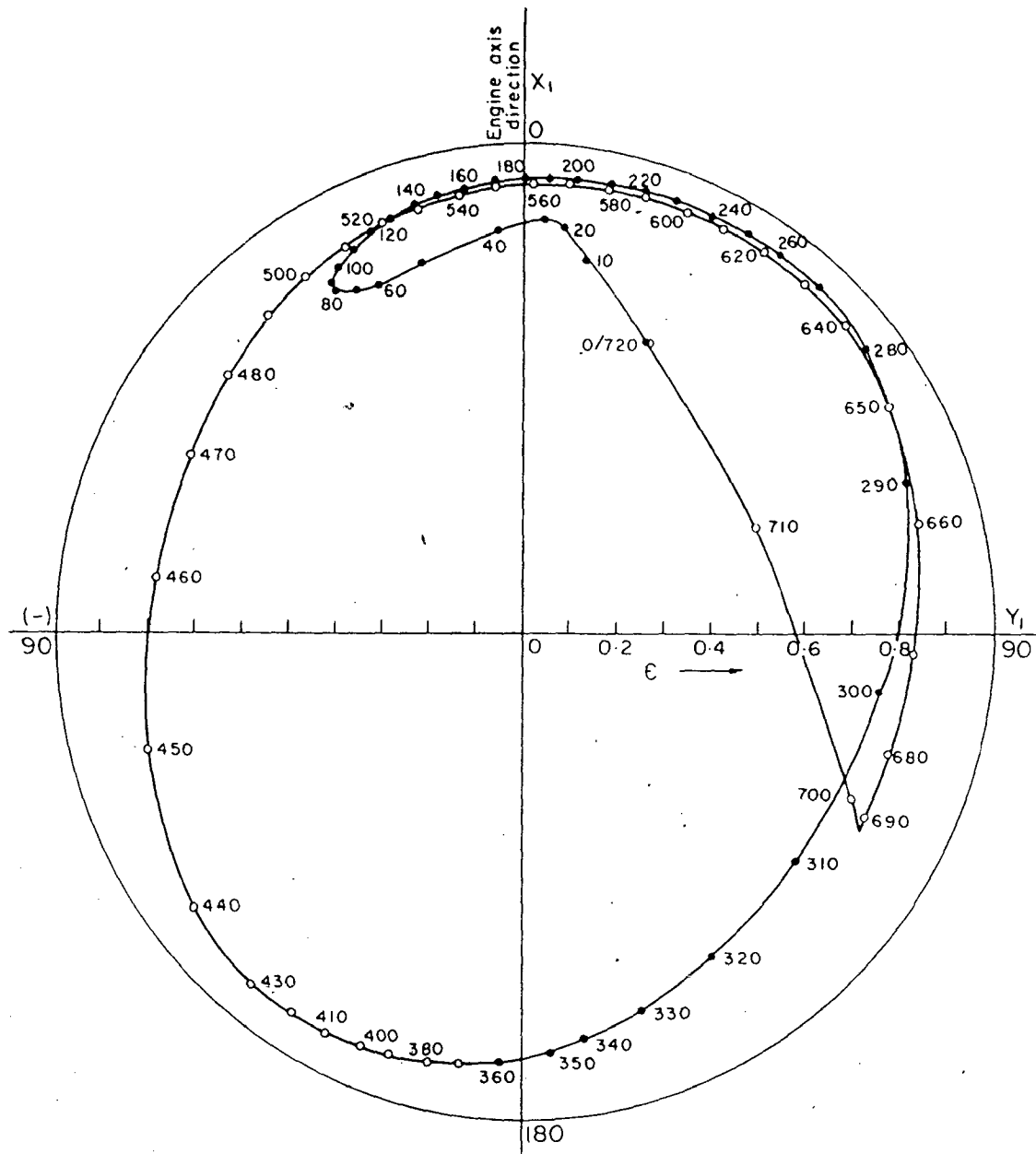


Fig.6.7 Bearing centre orbit (Piezoviscous case)

similar to that of the isoviscous case, Fig. 6.4 but the values of eccentricity ratios are slightly smaller than the values obtained in the isoviscous case. The maximum value of E in the piezoviscous case is 0.95059 which occurs at the crank angle 270° like that in the isoviscous case. Also the maximum value of E in the piezoviscous case is only slightly smaller than the corresponding value (0.95341) in the isoviscous case. Piezoviscous effect is, however, observed as significant at high loads (for instance at 100° , 180° , and 360° crank angles).

6.4.2b Maximum Film Pressure:-

Fig.6.8 shows the peak pressure variation versus crank shaft angle for the cases 1 and 2, Table-6.1. From Fig.6.8 it is noticed that almost in entire duty cycle the pressure generated in the fluid-film due to piezoviscous effect are larger than those in the isoviscous case. It is due to the increase of viscosity of the lubricant with pressure. The value of the maximum film pressure for the piezoviscous lubricant is found about 10% larger than that in the isoviscous case.

6.4.2c Minimum Film Thickness:-

A comparison of the minimum film thickness as a function of crank angle is shown in Fig.6.9 for cases 1 and 2. The minimum film thickness values are larger in the piezoviscous case in comparison to those in the isoviscous case. The minimum film thickness in the piezoviscous case is about 6% larger than that obtained in the isoviseous case. In both the cases 1 and 2, Table-6.1, the minimum film thickness occurs at the crank angle 270° .

6.4.2d Power Loss:-

Power loss accounting for pressure dependent viscosity variations

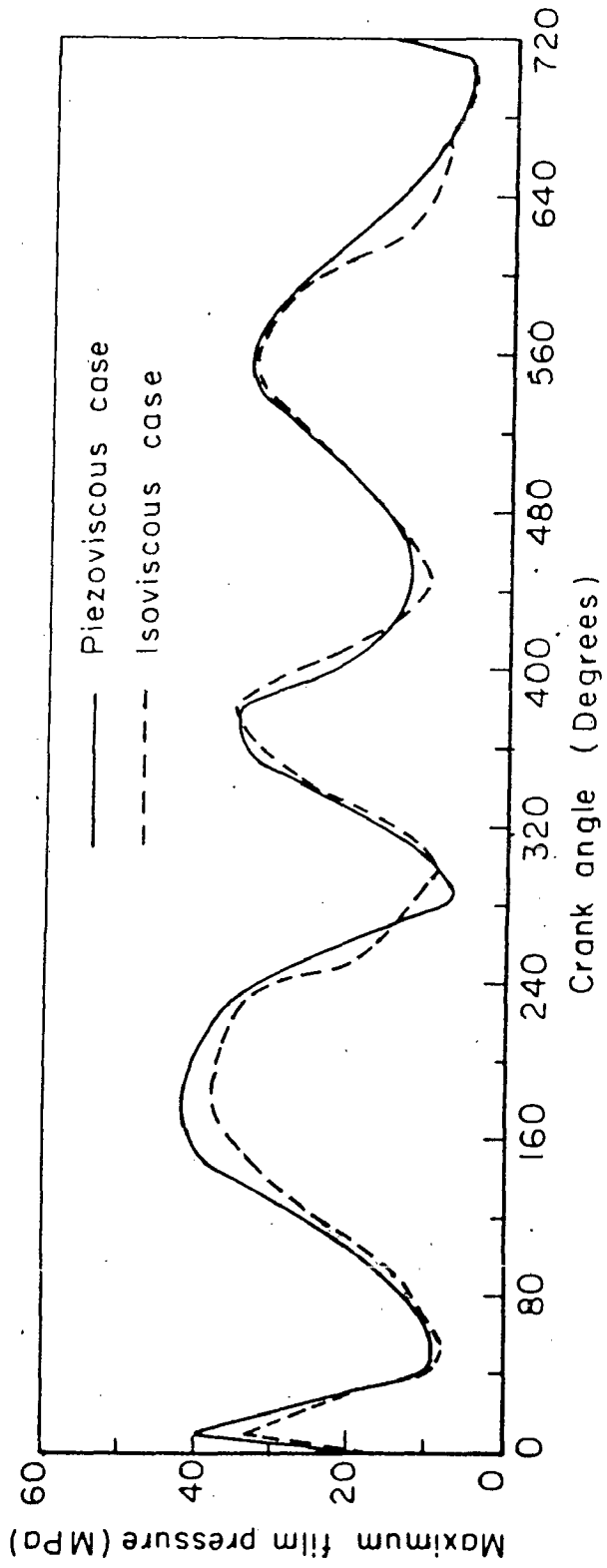


Fig. 6.8 Variation of maximum film pressure

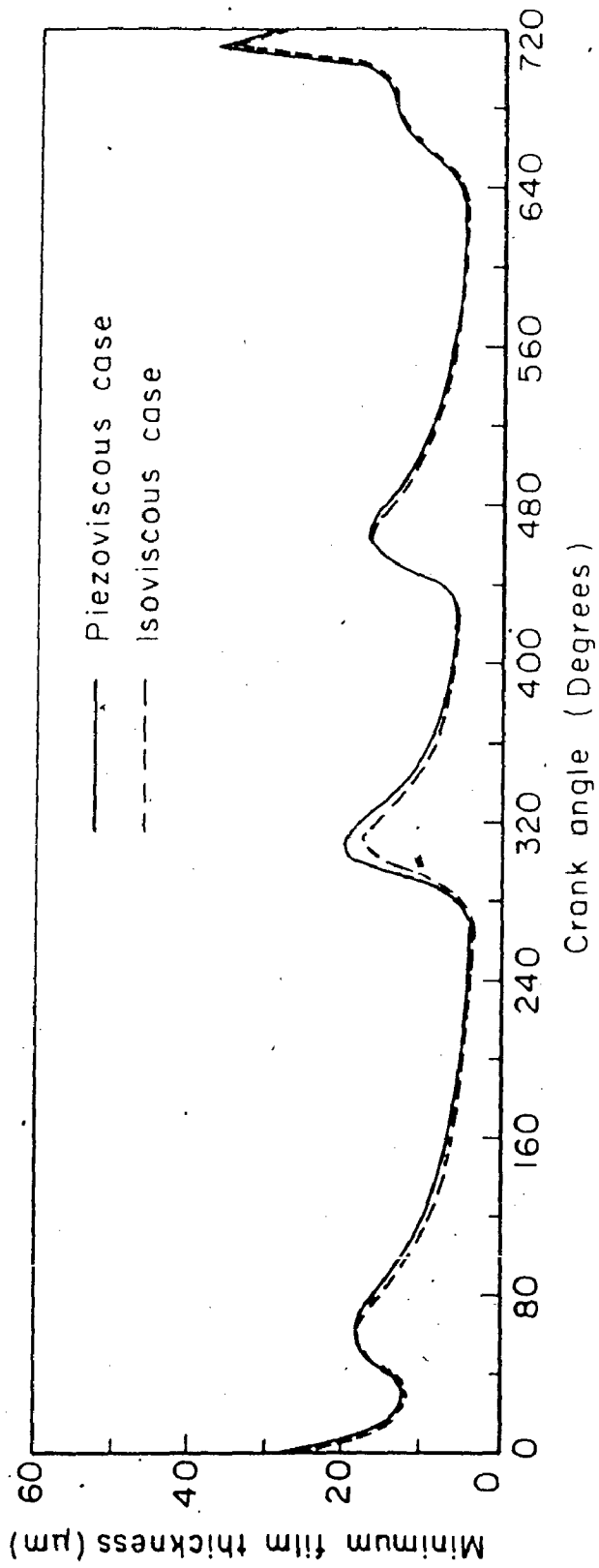


Fig.6-9 Variation of minimum film thickness

is calculated and is plotted against crank angle, Fig. 6.10. The maximum power loss is observed as 1.24 kW at the crank angle 10° in one duty cycle. The power loss is significant in the segment of crank rotation 320° to 400° in which the bearing speed is large, Fig. 4.3.

6.4.3 Rigid Bearing with the lubricants having Piezo-Thermal Viscosity Characteristics. (Piezo-Thermal case)

The combined effects of temperature and pressure on viscosity of lubricant is also considered to obtain the performance characteristics of the rigid big-end bearing. In the preceding sections, the viscosity is taken as constant or pressure dependent but in reality the viscosity of lubricant is more sensitive to temperature change. Hence, considering the viscosity variation with pressure and temperature both, the big-end bearing centre orbit, variation of the minimum film thickness, the peak pressure, power loss and the maximum temperature rise are calculated. The following results are observed and compared with those of the isoviscous case.

6.4.3a Bearing Centre Orbit:-

Fig. 6.11 shows the bearing centre orbit for one duty cycle. The shape of the orbit is similar to those previously obtained but in the piezo-thermal case almost all the values of eccentricity are larger than the values obtained in the isoviscous case. The maximum eccentricity ratio is calculated as 0.96176 and the corresponding value of β is 43.0° while, in the isoviscous case, the maximum eccentricity ratio is calculated as 0.95341 and the corresponding value of β is 41.8° .

6.4.3b Maximum Film Pressure:-

Fig. 6.12 shows the variation of the peak pressure in both, piezo-thermal and isoviscous case. In almost entire duty cycle, the

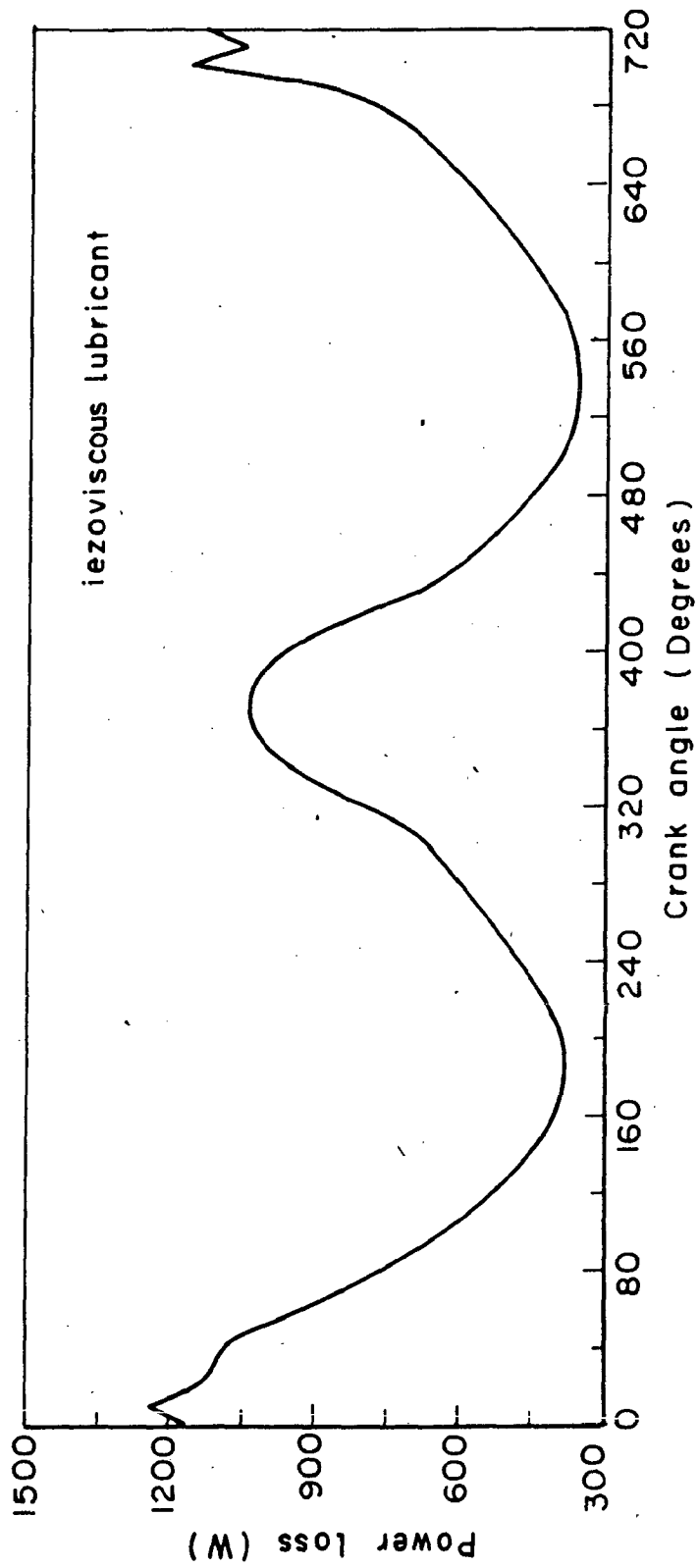


Fig. 6.10 Power loss as a function of crank angle
(Rigid bearing, piezoviscous case)

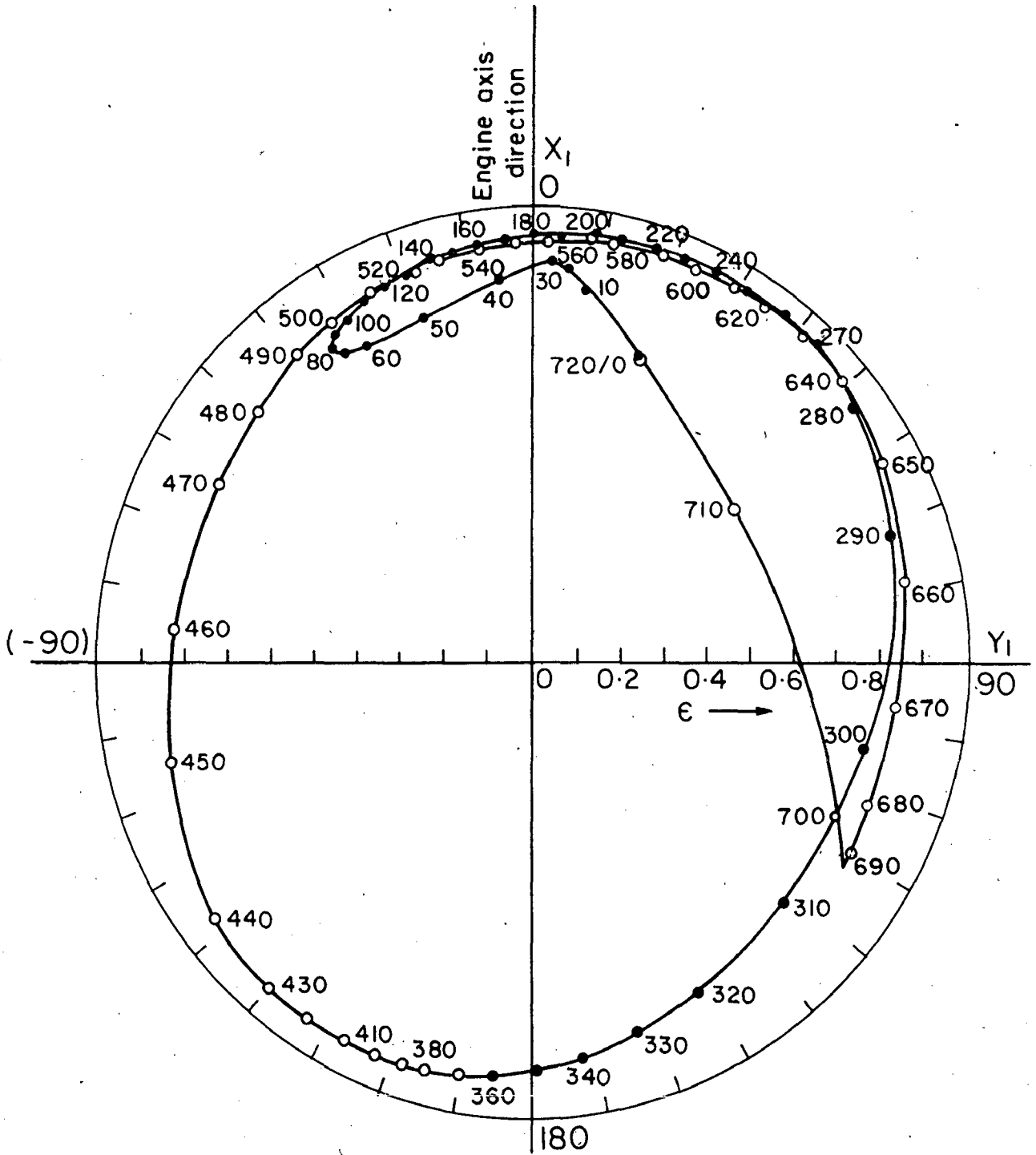


Fig. 6·11 Bearing centre orbit (Piezo-thermal case).

pressure values in the former case are more than those in the latter case. The maximum film pressure in the piezo-thermal case 3, Table-6.1, occurs at the crank angle 200° approximately. The maximum film pressure in the case 3 is about 24% larger than that in the isoviscous case 1. In the isoviscous case, the maximum film pressure occurs at 180° crank angle.

6.4.3c Minimum Film Thickness:-

Fig.6.13 presents the variation of the minimum film thickness against crank angle for both the cases 1 and 3. In the piezo-thermal case 3, the values of viscosity reduce significantly due to temperature rise of the fluid-film and in turn the load capacity of the bearing decreases. Hence, in this case, almost all the values of the minimum film thickness are smaller than those in the isoviscous case, Fig. 6.13. The value of minimum film thickness in the piezo-thermal case is calculated about 18% smaller than that obtained in the isoviscous case. The value of the minimum film thickness ($3.15 \mu\text{m}$) in the piezo-thermal case agrees more with the experimental values ($2.79 \mu\text{m}$ [10], $3.17 \mu\text{m}$ [4]). The position of occurrence of the minimum film thickness is almost same as in the isoviscous case i.e., in the vicinity of 270° crank angle position.

6.4.3d Maximum Temperature Rise:-

For the calculation of temperature rise in the fluid-film of the bearing in example, the SAE-30 oil was selected as lubricant for which the value of the constants ($\bar{\beta}_T, \bar{K}_S, \bar{K}_V, h_m$) are given in Appendix A-2. The supply temperature is assumed as 89°C . The crank pin surface temperature is taken uniform as 100°C and the bearing surrounding temperature (i.e., temperature in the crank case) is assumed as 80°C . The maximum temperature rise under these conditions,

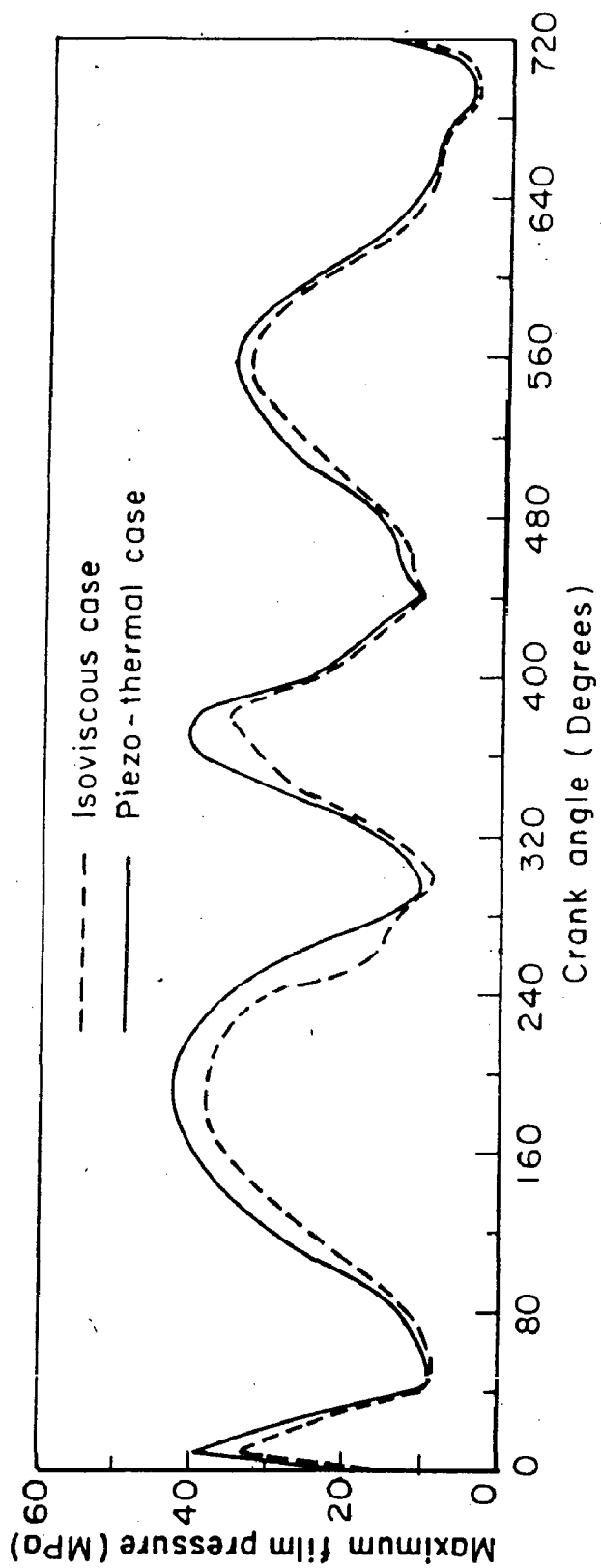


Fig.6.12 Variation of maximum film pressure

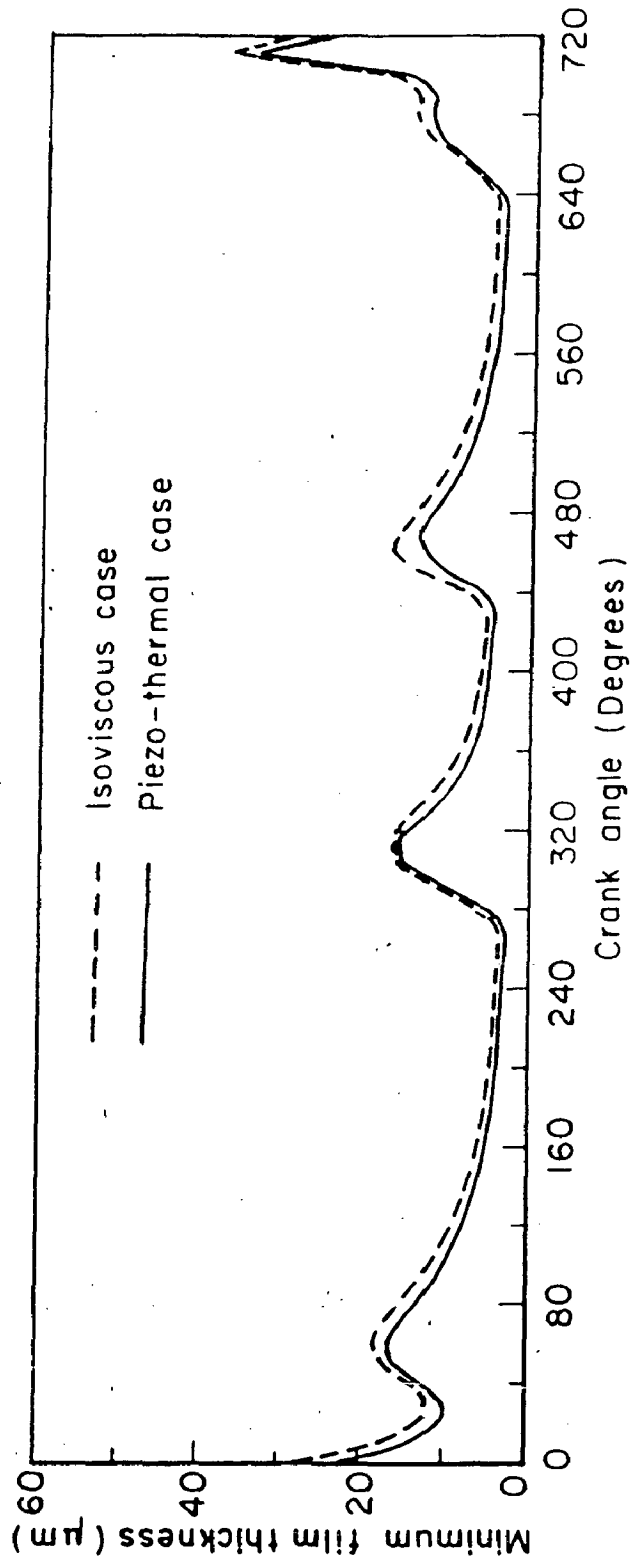


Fig.6.13 Variation of minimum film thickness

is shown in Fig. 6.14. The maximum temperature rise is obtained in the range of 10°C to 30°C which is comparable to the theoretically calculated value 25°C reported in the literature [63].

6.4.3e Power Loss:-

The variation of power loss and its comparison with that in the piezoviscous case is shown in Fig. 6.15. The maximum power loss obtained in the piezo-thermal case is found to be about 10% smaller than that (1.24kW) in the piezoviscous case. From Fig. 6.15, it may be concluded that due to reduction in viscosity, the power loss decreases under piezo-thermal condition.

6.4.4 Rigid Bearing with Non-Newtonian Lubricants

In the foregoing sections of this Chapter, the isoviscous, piezoviscous and piezo-thermal cases are discussed considering the lubricant as Newtonian. But the heavy duty engines require lubricants with superior viscosity index. The viscosity index is improved by adding suitable additives in the base oil which makes the behaviour of the lubricant non-Newtonian [37]. Hence, in this thesis the performance of the big-end bearing is also found with non-Newtonian lubricants represented by models, Eqs. (2.17) or curve-fit model, Eq.(2.20). The following results are obtained.

6.4.4(i) Cubic Shear Stress (c.s.s) Law Model

6.4.4(i)a Bearing Centre Orbit:-

Fig. 6.16 shows the bearing centre orbit using non-Newtonian lubricants. The non-Newtonian behaviour of the lubricants implies reduction in viscosity at high shear rate in the flow-field (range $2.5 \times 10^5 \text{ sec}^{-1}$ to $10 \times 10^5 \text{ sec}^{-1}$), and so, the load capacity of the bearing decreases. Due to this reason, the values of eccentricity ratio are obtained some what higher with non-Newtonian lubricants

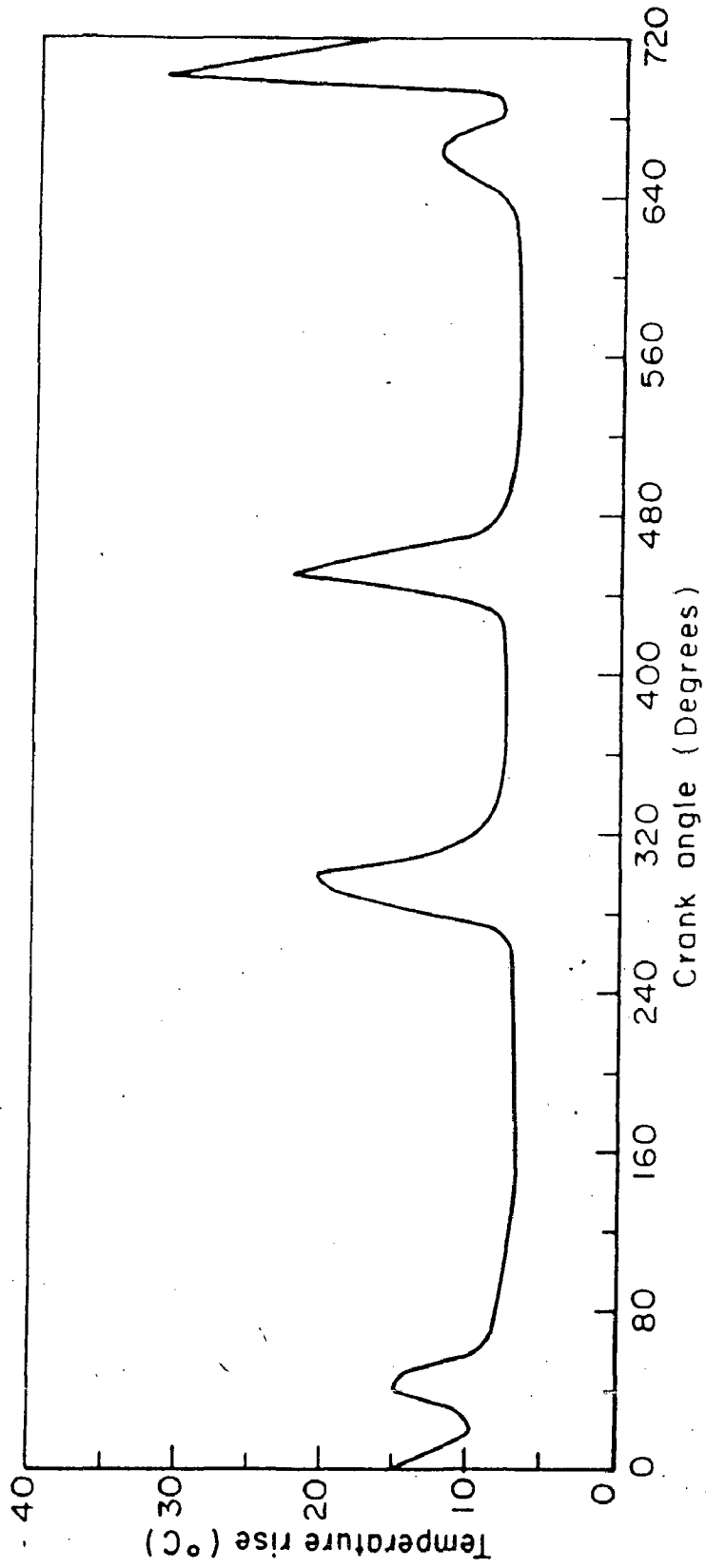


Fig.6.14 Variation of maximum temperature rise
(Rigid bearing, piezo-thermal case)

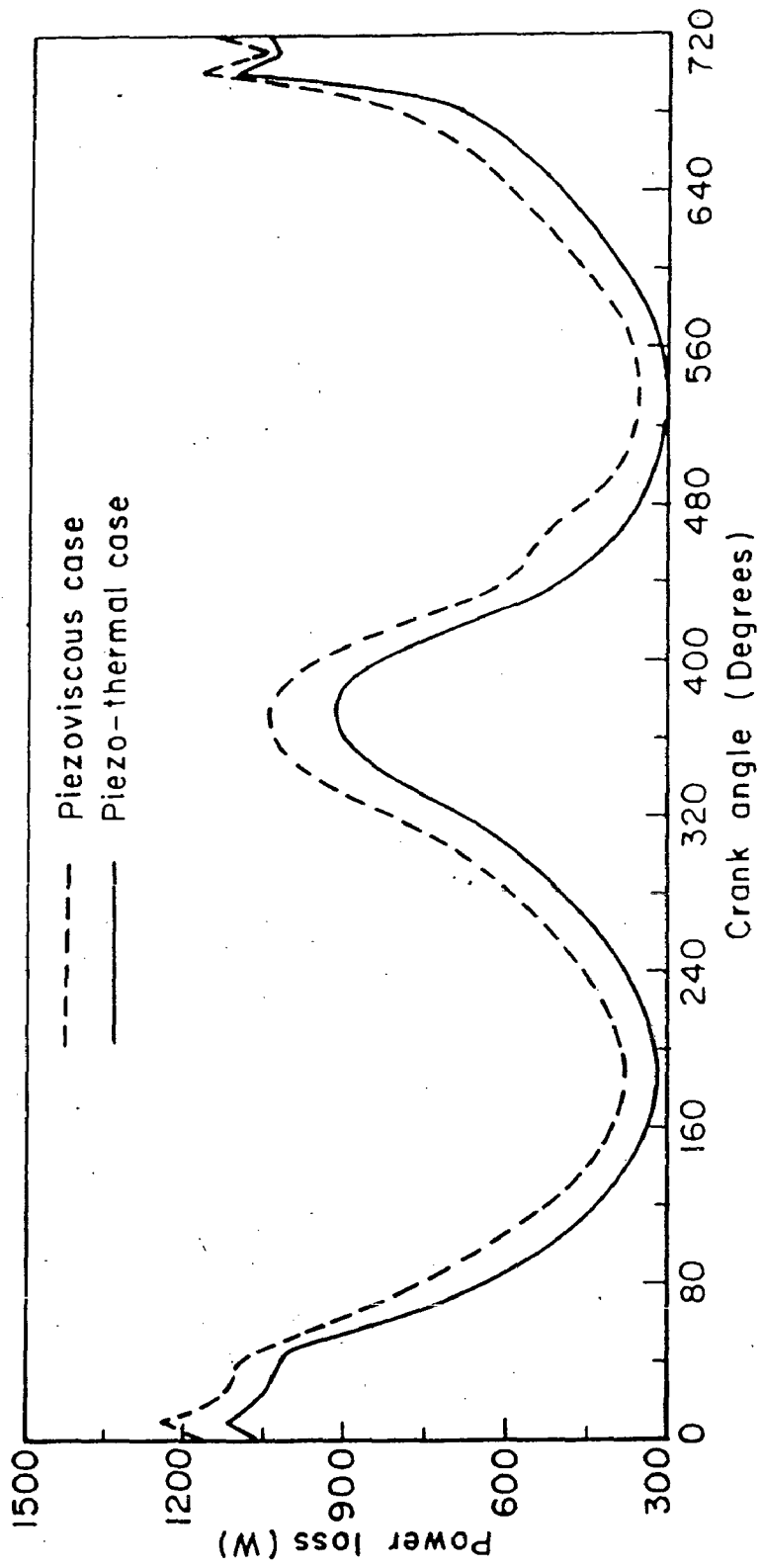


Fig. 6.15 Comparison of power loss

when compared to those obtained with the Newtonian lubricants in almost entire duty cycle. The orbit, Fig. 6.16, is obtained by representing the relation between shear strain rate ($\dot{\gamma}$) and shear stress ($\bar{\tau}$) with the cubic shear stress law, Eq.(2.17a). The cubic shear stress law represents the constitutive equation for most of the non-Newtonian oils in a wide range of shear rates. The value of constant $K = 0.58$ in Eq. (2.17a) is taken for calculation of complete orbit and other relevant results. The computer program is general and can handle any non-Newtonian model, Eqs. (2.17). A large CPU time is however required to compute one orbit, therefore, only one orbit using the cubic shear stress law with a selected value of K is calculated.

By comparing the orbit of Fig. 6.16 of the non-Newtonian case with that of Newtonian case, Fig. 6.4, a difference in the values of the maximum eccentricity ratio is noticed. For the non-Newtonian analysis, the maximum eccentricity ratio is found as 0.96165 in comparison to that (0.95341) in the Newtonian case. The maximum values of ϵ occur at 270° crank angle in both the cases 1 and 4, Table-6.1.

6.4.4(i)b Maximum Film Pressure:-

Fig. 6.17 is the plot of the peak pressure values which occur in the fluid-film of non-Newtonian lubricants at different position of the crank. These values of the peak pressure are also compared with those obtained in the Newtonian case. From Fig. 6.17, it is noticeable that in most part of the duty cycle the values of the peak pressure in both (Newtonian and Non-Newtonian) cases 1 and 4 are similar. The maximum value of the peak pressure for the non-Newtonian

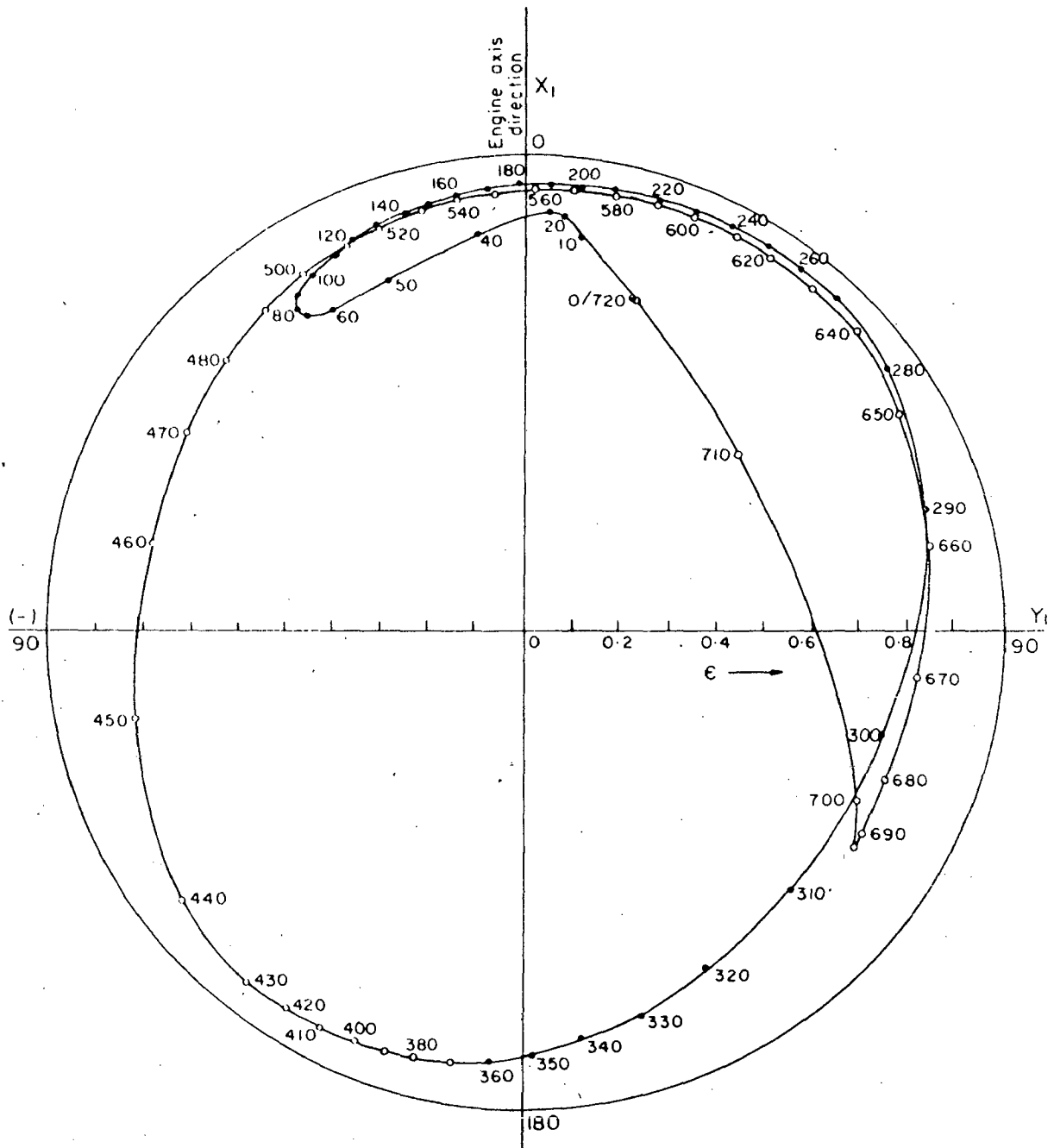


Fig. 6-16 Bearing centre orbit (Non-Newtonian case, cubic shear stress law model)

lubricant is only about 6% smaller than that for the corresponding Newtonian lubricant.

6.4.4(i)c Minimum Film Thickness:-

Fig. 6.18 shows the variations of the minimum film thickness against crank angle for cases 1 and 4. In most part of the duty cycle, the values of the minimum film thickness for the non-Newtonian lubricant case are smaller in comparison to those in the Newtonian case. The value of the minimum film thickness for non-Newtonian lubricant is 17% smaller than that for the corresponding Newtonian lubricant. The reduction in the value of the minimum film thickness is appreciable, hence, the non-Newtonian behaviour of lubricants should be taken into account for a more accurate design and analysis of the big-end bearing.

6.4.4(ii) Curve-Fit Model

For any lubricant, a relation between the apparent viscosity (μ_a) and shear strain rate ($\dot{\gamma}$) can be established by curve fits on experimental data. Experimental data are available for several non-Newtonian (commercial) oils at different temperatures [37]. Using the least square method, a fourth order polynomial is fitted on the values of μ_a and $\dot{\gamma}$ for one of the oils (code C-2, at 99° C), Eq.(2.20). Using this equation in the non-dimensional form, a part of the orbit is obtained with 10° interval for a finite crank rotation $110^\circ < \theta_1 < 270^\circ$. The cubic shear stress law, Eq. 2.17a, represents the non-linear behaviour of a wide range of non-Newtonian lubricants. The values of ϵ and β obtained by using the cubic shear stress law and the curve-fit model are given for comparison in Table-6.5. The Table shows that the values of ϵ, β are almost identical in the two cases.

Using the least square method, other given values of μ_a and $\dot{\gamma}$ for

Table-6.5

Comparison of the results obtained for the big-end bearing having non-Newtonian lubricants (cubic shear stress law and curve-fit model)

Crank angle θ_1	Curve-fit model		Cubic shear stress law model	
	ϵ	β	ϵ	β
110	0.91818	-19.49	0.91755	-19.32
120	0.92455	-17.49	0.92293	-17.05
130	0.93077	-14.91	0.92846	-14.33
140	0.93641	-11.97	0.93354	-11.32
150	0.94125	- 8.84	0.93805	- 8.16
160	0.94557	- 5.54	0.94205	- 4.85
170	0.94921	- 2.09	0.94541	- 1.43
180	0.95206	+ 1.49	0.94823	+ 2.13
190	0.95460	5.24	0.95074	5.85
200	0.95692	9.15	0.95308	9.72
210	0.95898	13.24	0.95518	13.75
220	0.96093	17.51	0.95702	17.94
230	0.96252	21.97	0.95870	22.30
240	0.96371	26.66	0.96013	26.89
250	0.96458	31.64	0.96102	31.81
260	0.96495	37.03	0.96152	37.14
270	0.96502	43.14	0.96165	43.06

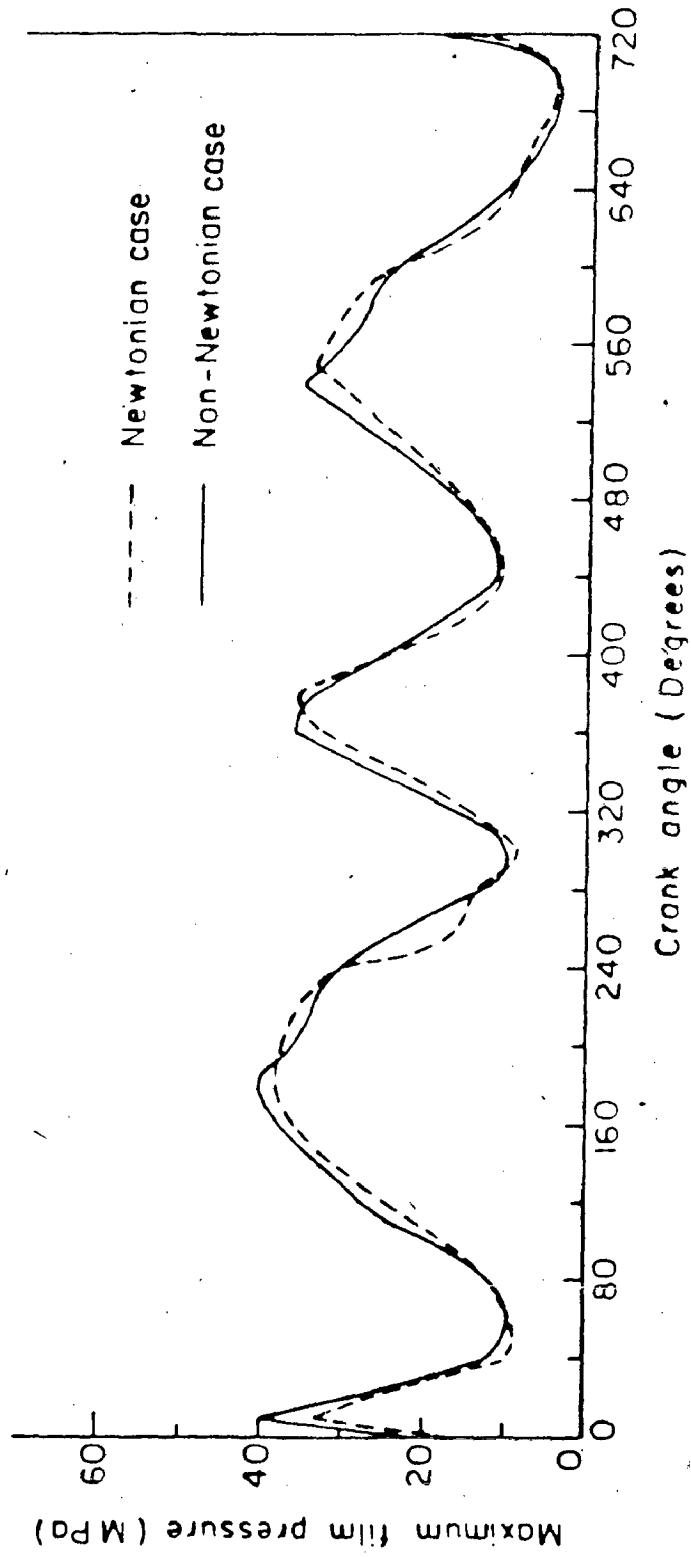


Fig.6.17 Variation of maximum film pressure

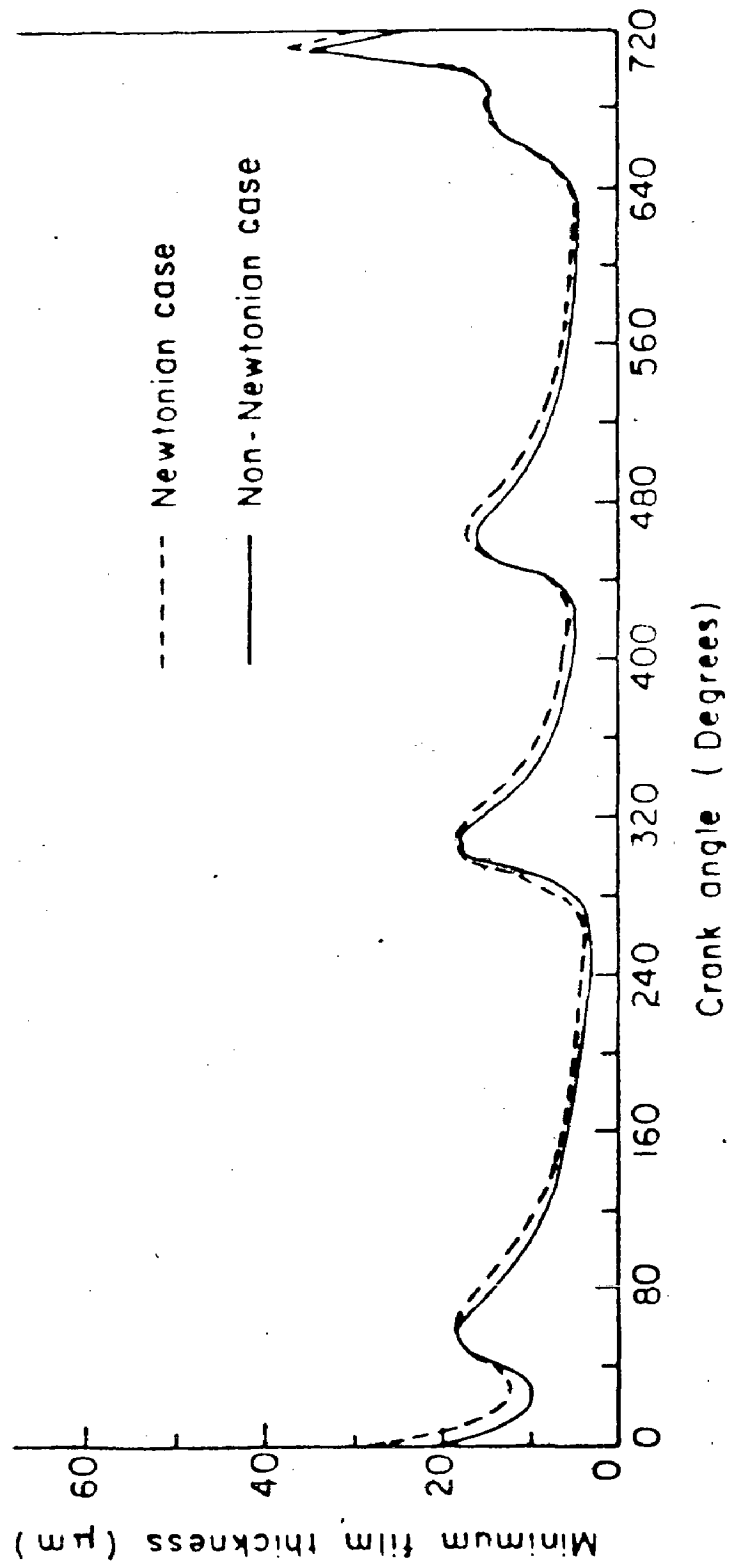


Fig.6-18 Variation of minimum film thickness

other oils [37] are fitted in fourth order polynomials whose coefficients are given in Table-2.2 for each oil. These values of coefficients may be useful for further studies.

6.4.5 Ungrooved Rigid Bearing with Isoviscous Lubricants

The 6VEB-X engine bearing has a circumferential groove of 12.7mm (0.5in) width. There are some big-end bearings which do not have this type of groove. So, to evaluate the performance of the big-end bearing without circumferential groove, the same big-end bearing with full length subjected to full load, Fig. 4.2, is solved and the results are compared with those previously presented for the grooved bearing. The same configuration of bearing with small misalignment, if present, is also studied. The bearing centre orbit, the maximum film pressure, and the minimum film thickness are obtained for, both, parallel and misaligned bearing assembly. The results are presented as follows:

6.4.5(i) Parallel Axes System

6.4.5(i)a Bearing Centre Orbit:-

Fig. 6.19 shows the bearing centre orbit of the big-end bearing without groove. In the absence of a circumferential groove, the relevant boundary conditions and in turn the pressure profile, Fig. 1.5, are different which significantly change the bearing performance. From the solution it is found that in this case, the eccentricity decreases significantly and the bearing operates with a larger minimum film thickness. The maximum eccentricity ratio is calculated as $\epsilon = 0.88974$ and the corresponding value of β is 43.50° . The two orbits, Figs. 6.19 and 6.4, show that the eccentricities for ungrooved bearings are significantly smaller than those for grooved bearings.

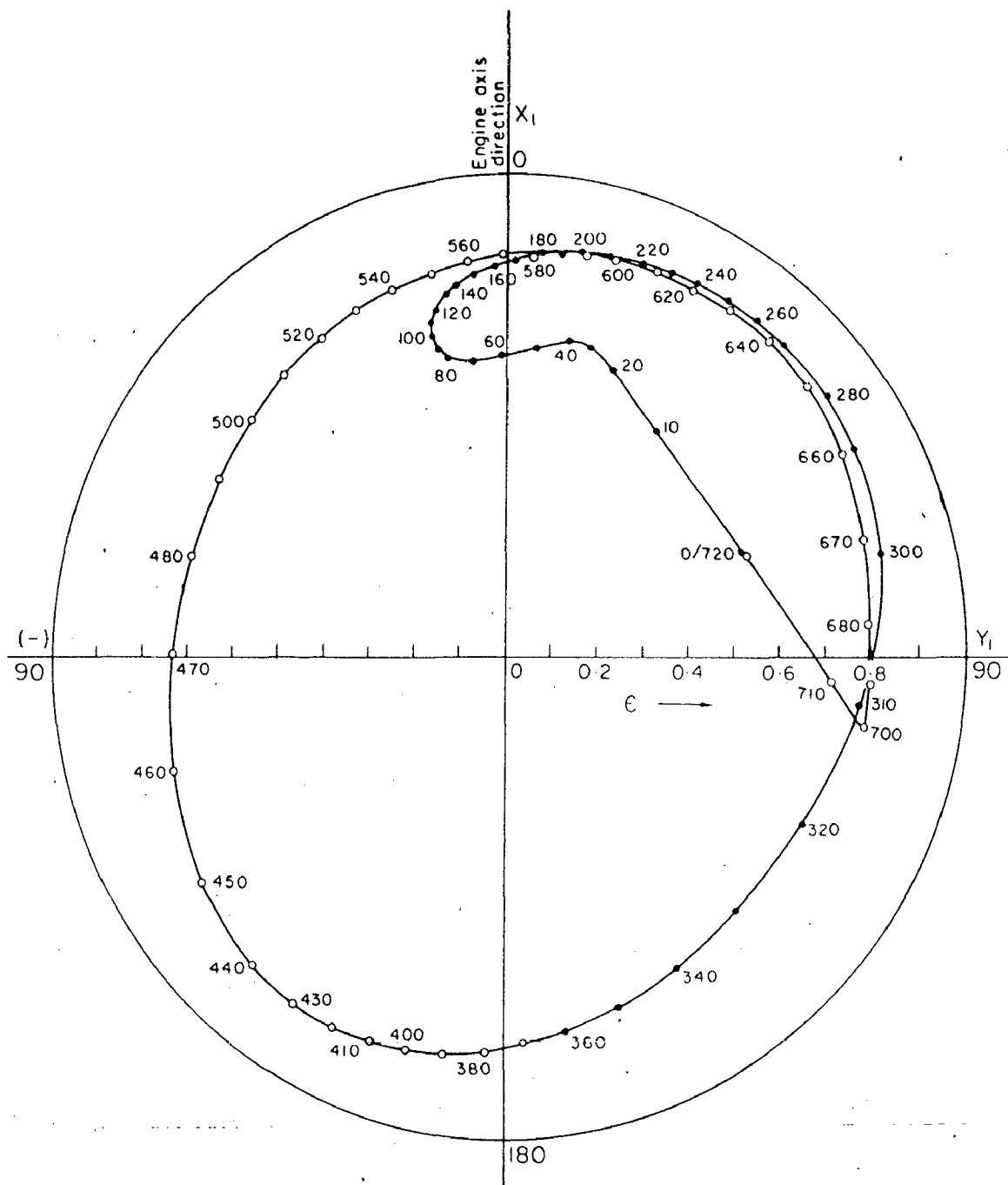


Fig.6.19 Bearing centre orbit of the big-end bearing without circumferential groove
 (Parallel axes case i.e. $\sigma = \delta = 0$ and $\bar{B} = 0.625$)
 (Force variation fig.4.2)

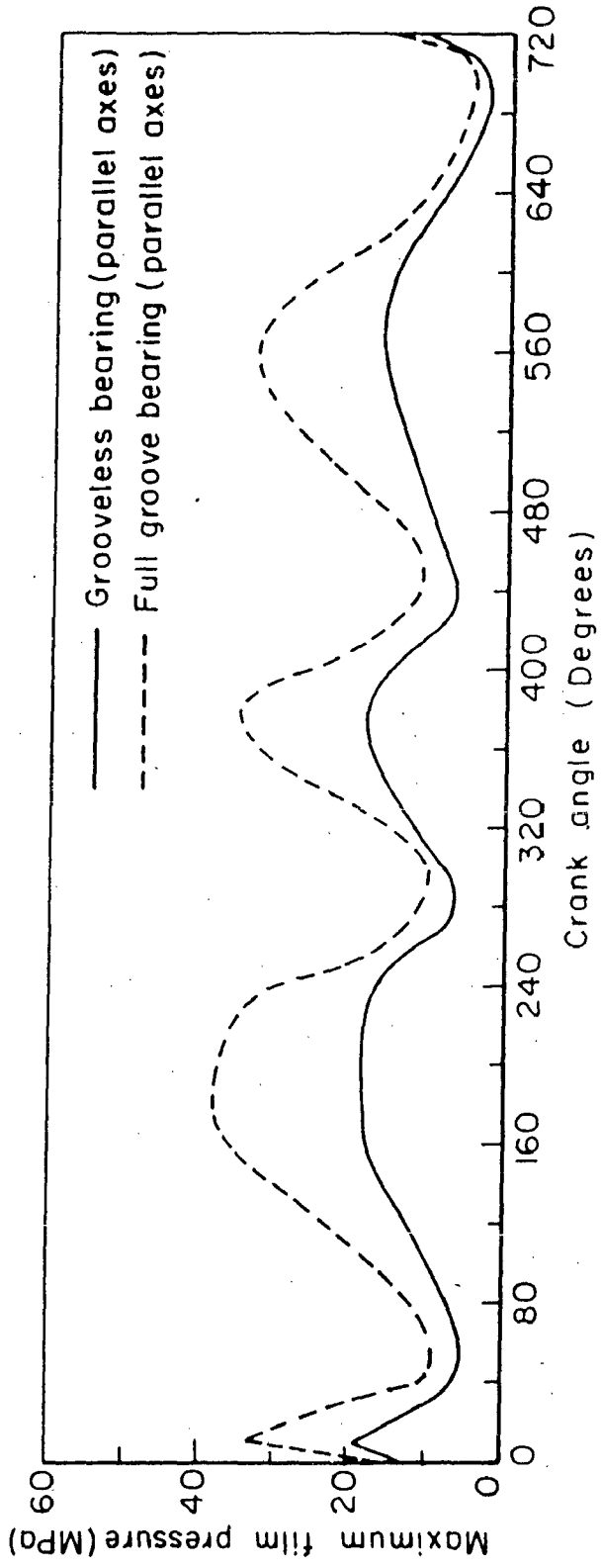


Fig.6.20 Variation of maximum film pressure

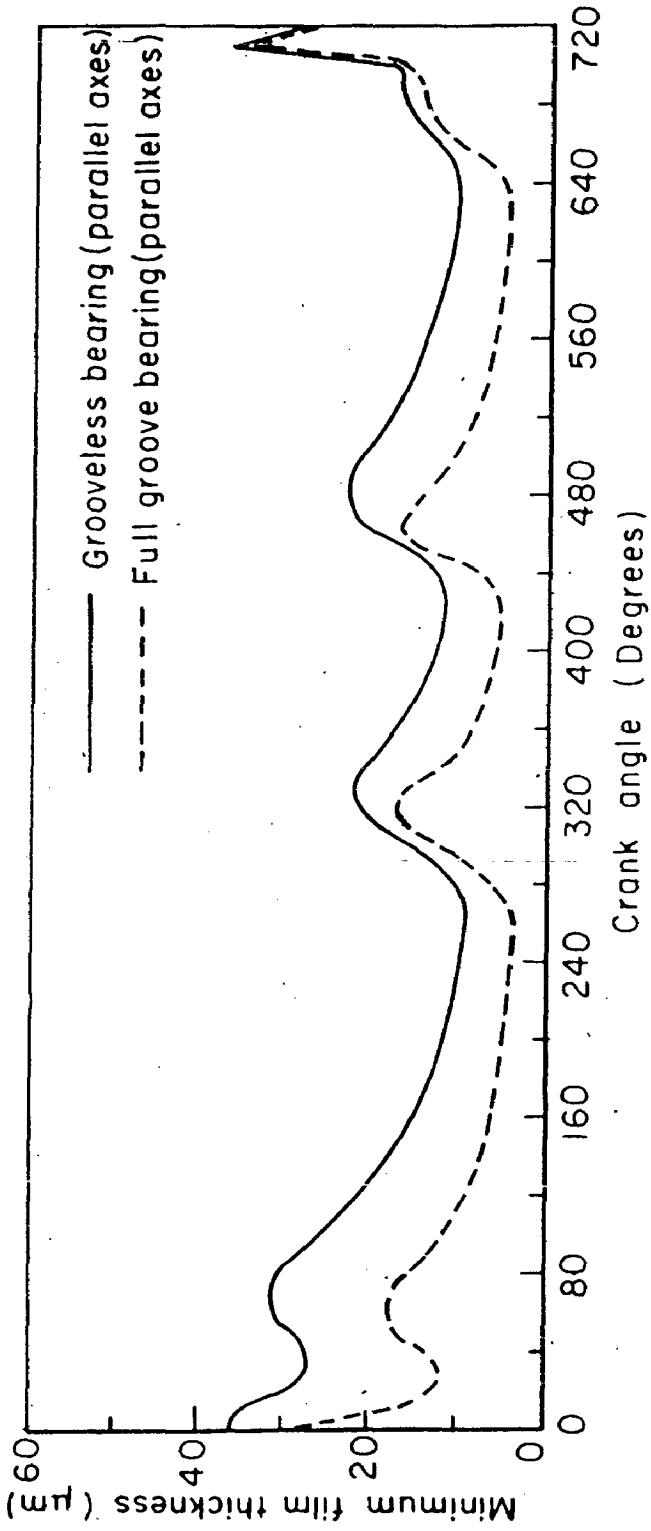


Fig.6.21 Variation of minimum film thickness

6.4.5(i)b Maximum Film Pressure:-

Fig. 6.20 is the plot of the peak values of the fluid-film pressure which occur in, both, grooved and ungrooved bearings. From Fig. 6.20, it is indicated that the fluid-film peak pressures are smaller in the ungrooved bearing in comparison to those in the grooved bearing due to different pressure boundary conditions in both the cases 1 and 5, Table-6.1. The maximum film pressure in the ungrooved bearing is about 50% smaller than that in the grooved bearing. It shows that the ungrooved bearings operate at low fluid-film pressures in comparison to the grooved bearings subjected to the same external load. It enhance the life of the bearings.

6.4.5(i)c Minimum Film Thickness:-

Fig. 6.21 is the plot of the minimum film thickness variations versus crank angle for the cases 1 and 5. In most part of the duty cycle, the values of the minimum film thickness for ungrooved bearings (parallel axis) are almost 3 times that of the corresponding values obtained in the grooved bearing case. The minimum film thickness in ungrooved bearings is about 136% larger than that in the grooved bearings.

6.4.5(ii) Skewed Axes System

Error in the assembly of the bearing in the connecting rod end makes the axes of the bearing and the crank pin misaligned. Considering a small misalignment of $\sigma = \delta = 0.0001$, Fig. A-5.1, between the bearing and the crank pin axes, the ungrooved big-end bearing performance characteristics are computed and the results are as follows.

6.4.5(ii)a Bearing Centre Orbit:-

Fig. 6.22 shows the bearing centre orbit (skewed axes) which is

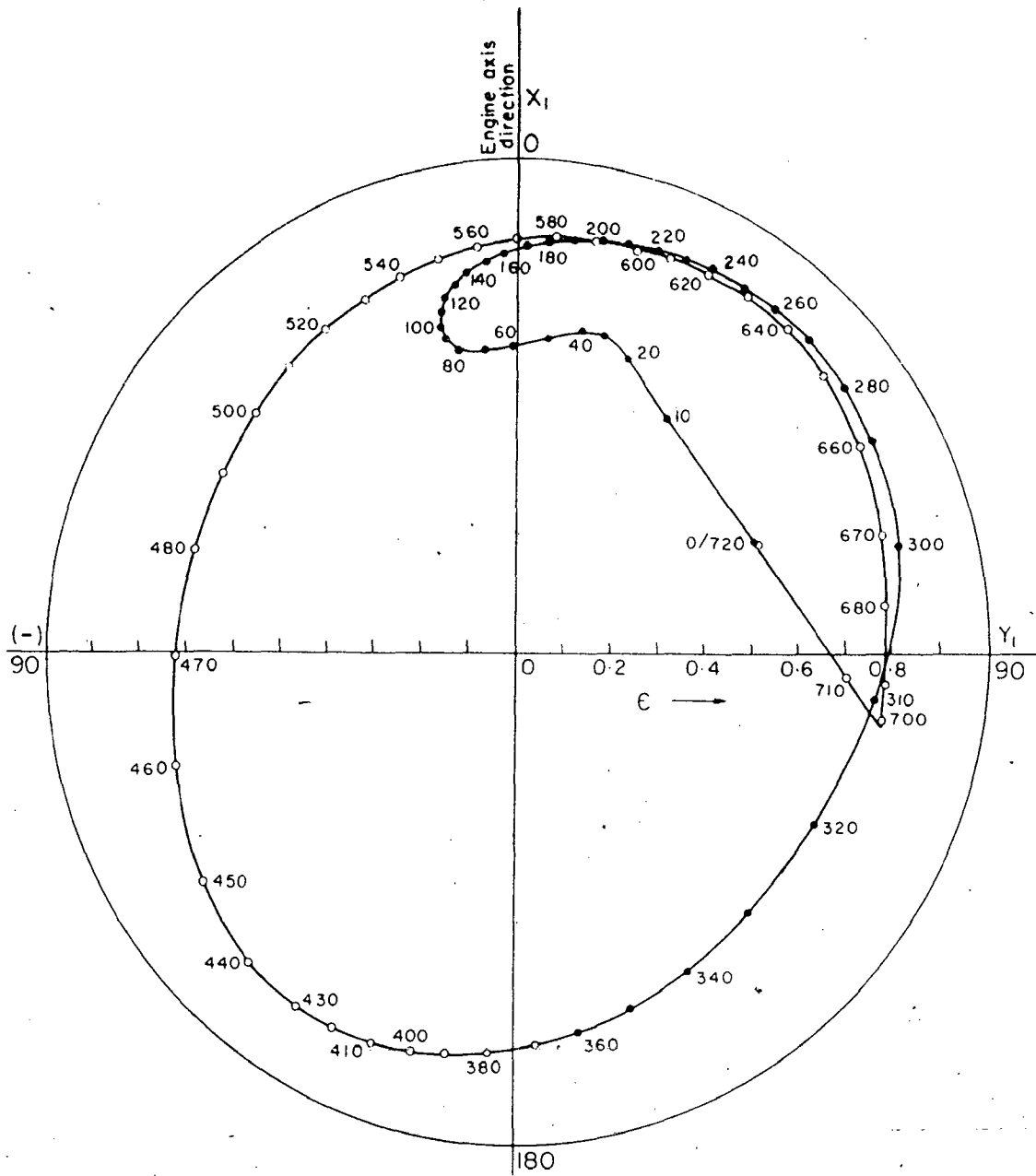


Fig.6.22 Bearing centre orbit of the big - end bearing without circumferential groove
 (Skewed axes case i.e. $\sigma = \delta = 0.0001$ and $\bar{B} = 0.625$)
 (Force variation. fig.4'2)

very similar to that of Fig. 6.19. In the case of skewed bearing, the maximum mid plane eccentricity ratio is obtained as 0.88990 and the corresponding value of β is 43.43° which are close to the values $e = 0.88974$ and $\beta = 43.50^\circ$ obtained in the parallel axes bearing system.

6.4.5(ii)b Maximum Film Pressure:-

Fig. 6.23 shows the values of the peak pressure in the bearing having skewed axes and their comparison with the peak pressures obtained in the parallel axes bearing assembly. From Fig. 6.23, it is noticed that in almost entire duty cycle, the peak pressure generated in the skewed axes bearing assembly are larger than the peak pressure in the parallel axes bearing assembly. The maximum value of the peak pressure in the skewed axes bearing system is about 26% larger than that value obtained in the parallel axes bearing system.

6.4.5(ii)c Minimum Film Thickness:-

In the case of skewed axes bearing assembly, the minimum film thickness occurs on one of the sides of the bearing away from its central plane. Fig. 6.24 shows the variations of the minimum film thickness in skewed axes bearing system and its comparison with that for parallel axes bearing system. The two variations are similar but the magnitudes of the minimum film thickness differ significantly in entire duty cycle. In the case of skewed axes bearing system, the minimum film thickness occurs at crank angle 220° , not occurs at 270° crank angle like in other cases. The minimum film thickness in skewed axes bearing system is about 28% smaller than that in parallel axes bearing system. It may be concluded, that if the misalignment is larger, the possibility of occurrence of metal to metal contact in the skewed assembly increase.

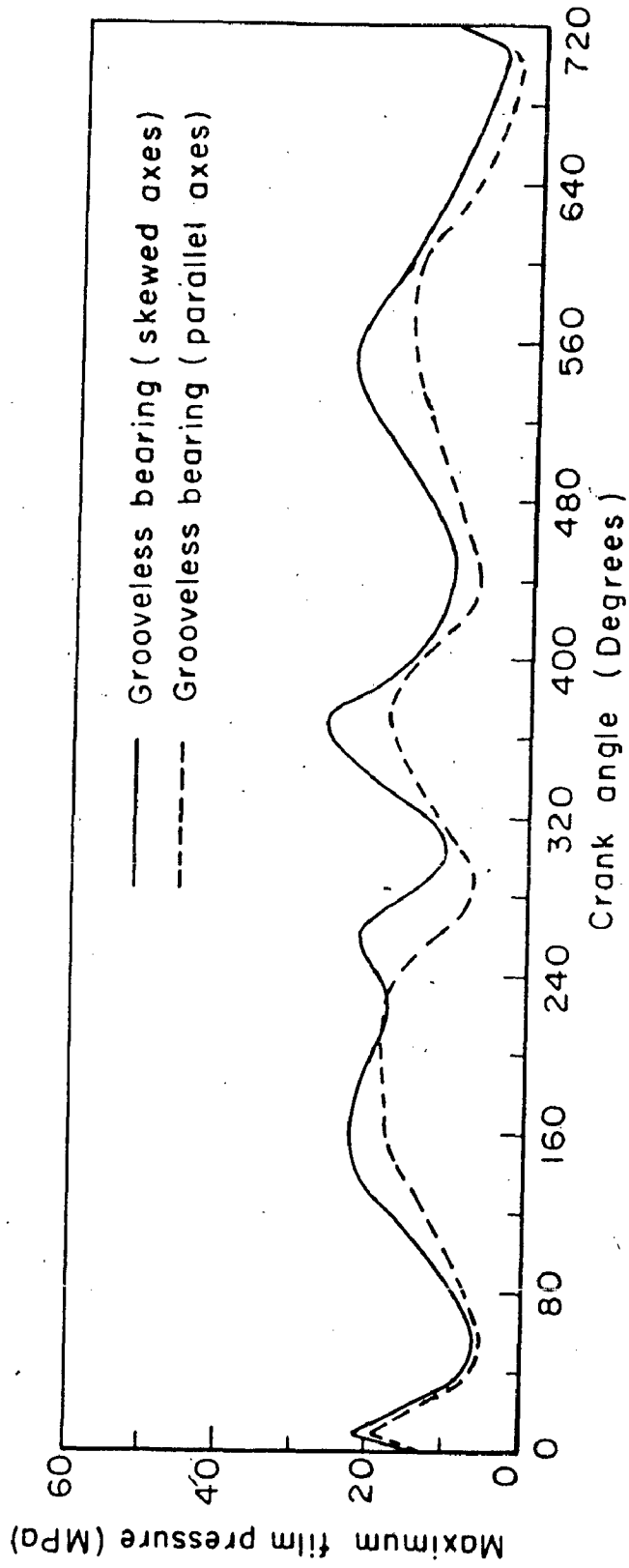


Fig.6:23 Variation of maximum film pressure

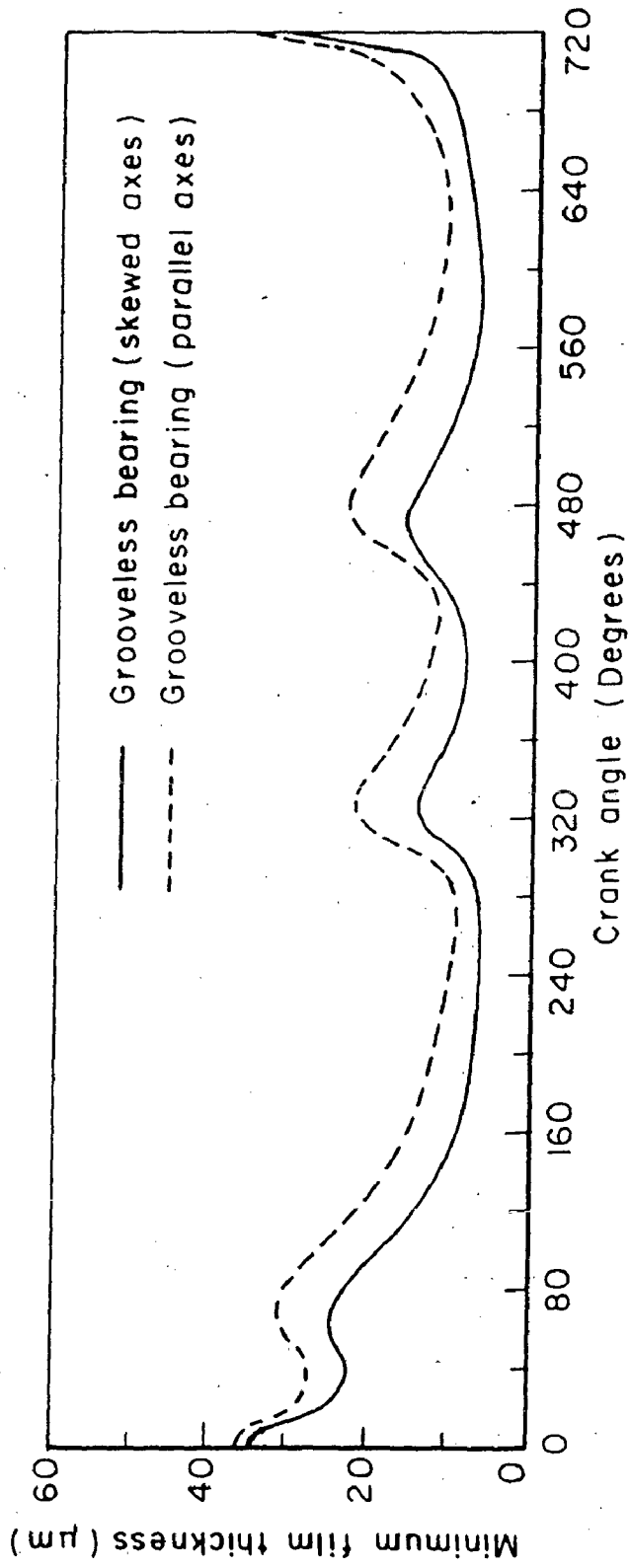


Fig.6.24 Variation of minimum film thickness

6.4.6 Elastothermohydrodynamic (ETHD) Lubrication Study of the Big-End Bearing.

In the foregoing section, the performance characteristics of the big-end bearing for various lubrication conditions without including the flexibility of the bearing body are discussed. But it is well known today that elastic deformation in the bearing body whether permanent or transient, significantly affects the performance of the hydrodynamic bearings. Hence, the analysis of the problem of the big-end bearing is extended to include the ETHD considerations. In the case of the big-end bearings, due to the deformation of bearing body, both inner and outer surfaces of bearing deform and experience change in shapes. The bearing body is assumed as cylindrical initially, and made of cast iron [42], which give the value of deformation coefficient ($\bar{\Phi}$) = 0.009229, $(R/t_h) = 1.77$ and $(c/t_h) = 0.00144$. The outer portion of the big-end bearing (about 2/9 part), which is integrated with the connecting-rod, is considered as fixed boundary and the remaining outer surface of the bearing is taken free to deform. The following results are obtained in this condition.

Starting from any arbitrary crank angle, e.g., 250° , and using a nondimensional time step of 2° , the values of e, β , the minimum film thickness, the maximum deformation, and the maximum temperature rise are calculated for a finite crank rotation, upto crank angle 320° and are reported in the Table-6.7. From this Table it may be seen that considerable deformation occurs in the bearing body. The deformation pattern of both the bearing surfaces (inner and outer) at some (260° , 270° , 280° , and 300°) crank angles are shown in Figs.6.25. Due to the irregular and significant deformations in the bearing body, Figs.6.25, the convergence of the solution at each crank angle takes a large CPU

Table-6.7

Values of ϵ , β , the minimum film thickness (h_{min}), the maximum temperature rise (T_{max}), and the maximum deformation at the inner surface of the bearing body (d_{rmax}) in the elastothermohydrodynamic lubrication case for finite crank rotation

Crank angle θ_1	ϵ	β	h_{min} (μm)	d_{rmax} (μm)	T_{max} ($^{\circ}C$)
250	0.94948	30.29	4.15	-	-
252	0.94994	31.44	7.69	4.70	7.21
254	0.95038	32.76	6.64	4.37	7.21
256	0.95048	34.14	6.20	3.79	7.30
258	0.95041	35.55	6.26	4.12	7.30
260	0.95022	37.00	6.27	4.04	7.30
262	0.94993	38.50	6.43	4.37	7.39
264	0.94959	40.18	7.82	8.33	7.56
266	0.94881	42.15	7.47	9.98	7.92
268	0.94750	44.25	7.44	9.91	8.45
270	0.94588	46.42	7.50	10.15	9.52
272	0.94385	48.70	7.52	10.15	10.68
274	0.94319	50.73	7.82	10.48	10.14
276	0.94318	52.97	8.80	10.90	10.68
278	0.94186	56.07	10.41	13.70	9.88
280	0.93921	59.70	9.57	15.27	9.35
282	0.93545	63.72	10.38	16.01	10.77
284	0.93280	68.37	14.15	20.22	9.70
286	0.93082	73.52	13.85	19.48	10.32
288	0.92803	78.90	14.00	20.06	10.15
290	0.92819	82.72	16.73	21.07	10.41

Table-6.7 Contd...

1	2	3	4	5	6
292	0.93018	85.00	19.84	26.02	6.23
294	0.93552	89.77	21.48	29.80	6.50
296	0.94625	95.73	23.86	24.68	8.54
298	0.94996	101.62	16.77	21.05	14.60
300	0.95106	108.68	19.43	22.78	12.10
302	0.95411	115.68	24.08	27.65	11.30
304	0.96871	122.16	25.64	29.22	10.68
306	0.97742	126.08	27.11	27.42	8.63
308	0.97746	127.74	23.97	23.30	7.92
310	0.97758	130.41	24.50	23.71	6.32
312	0.97938	132.98	25.25	24.12	6.40
314	1.05874	136.34	35.47	47.28	7.12
316	1.15368	141.20	30.11	46.14	7.47
318	1.18836	146.00	33.22	53.16	7.89
320	1.21673	149.81	21.49	43.91	6.67

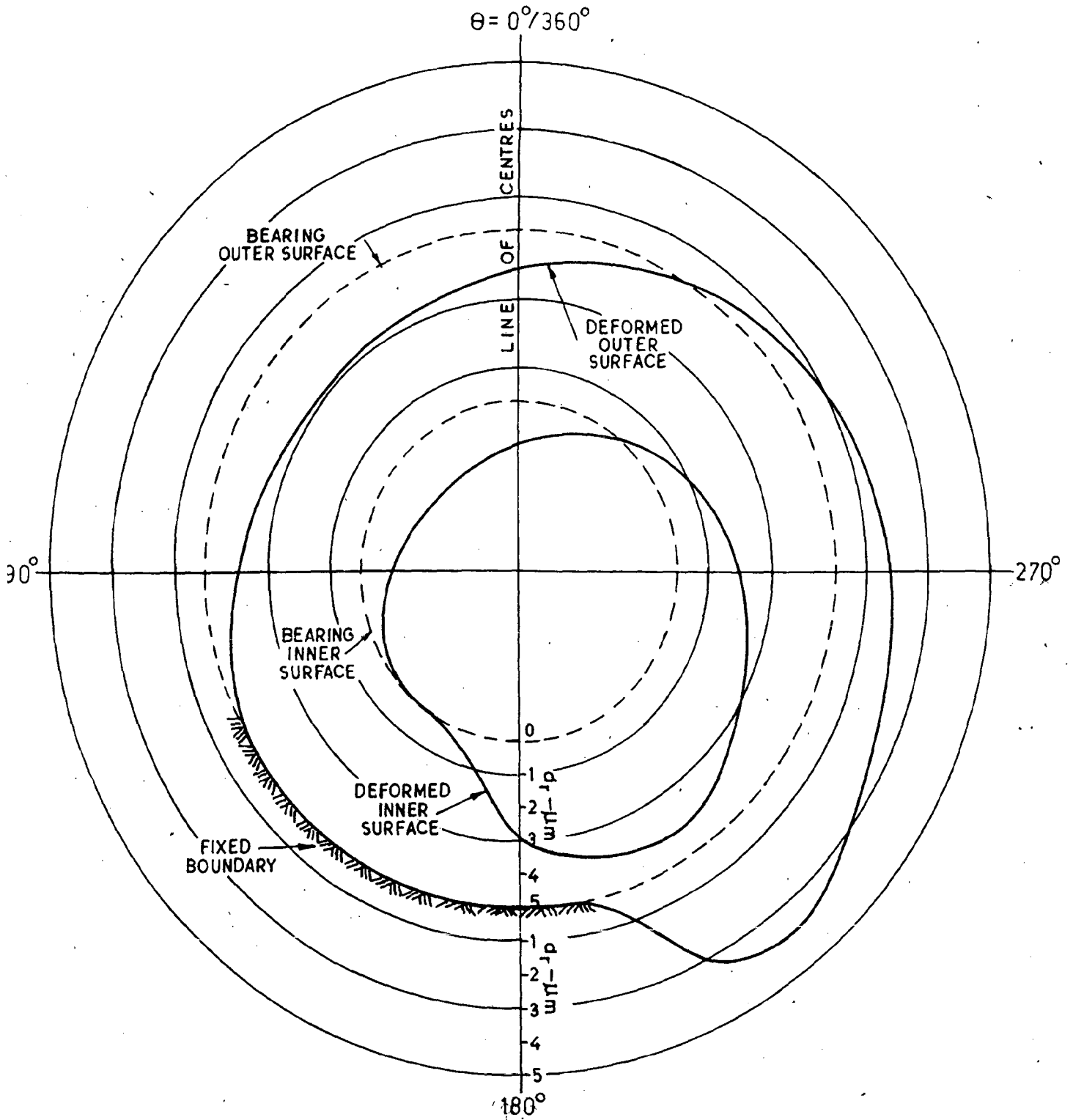


Fig.6.25a Deformation pattern of bearing body at 260 deg. crank angle

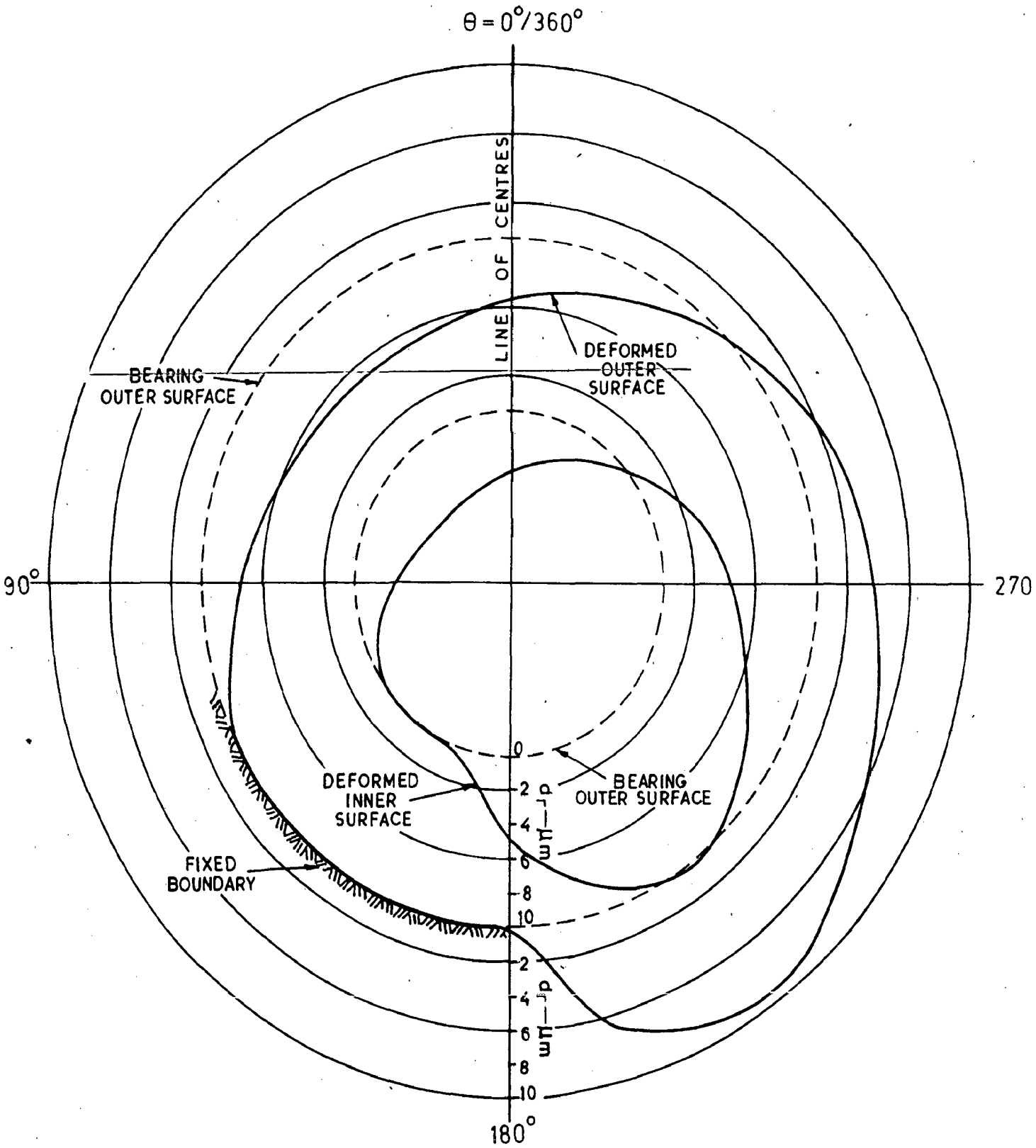


Fig. 6.25b Deformation pattern of bearing body at 270 deg. crank angle

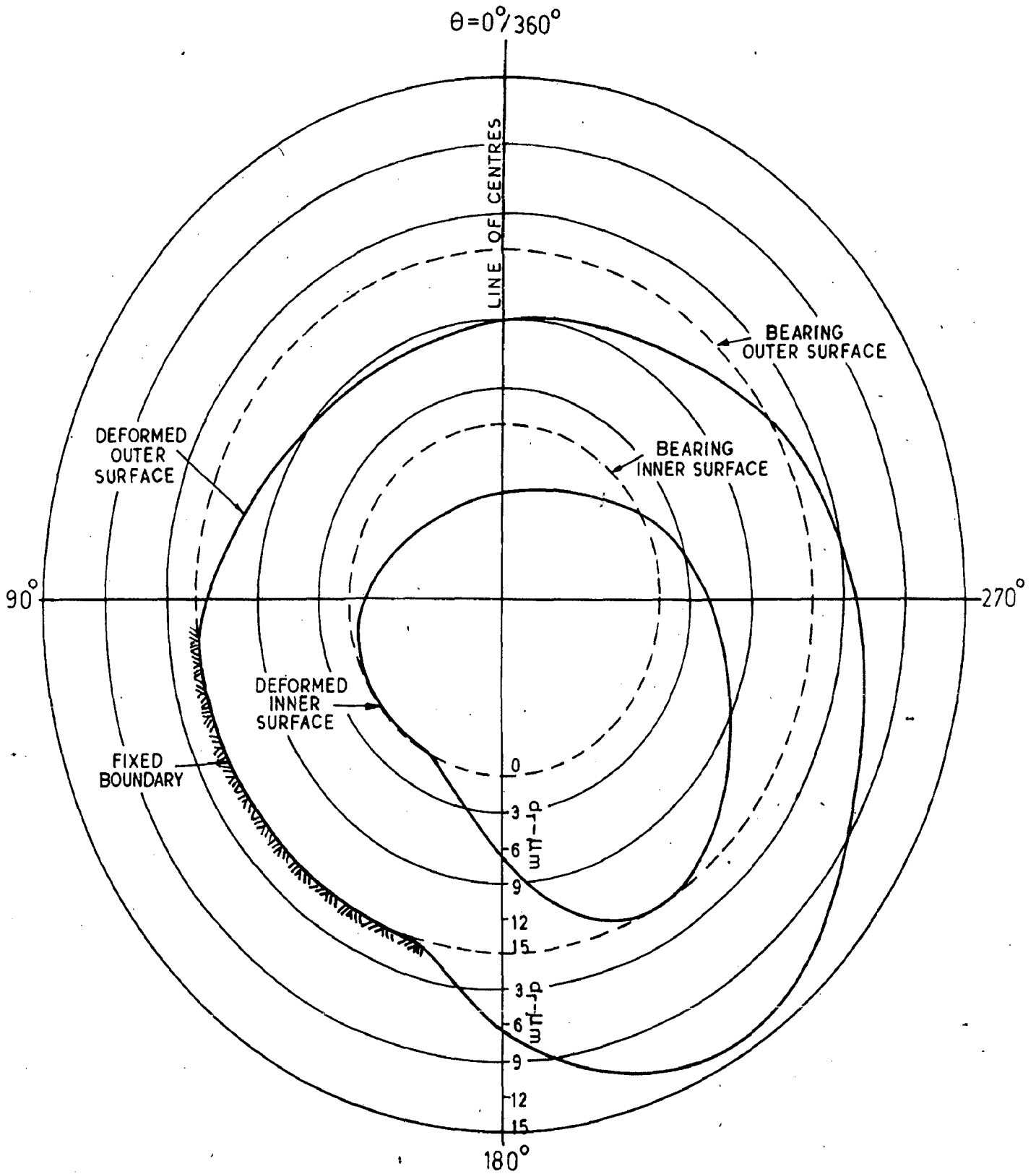


Fig. 6.25c Deformation pattern of bearing body at 280 deg. crank angle

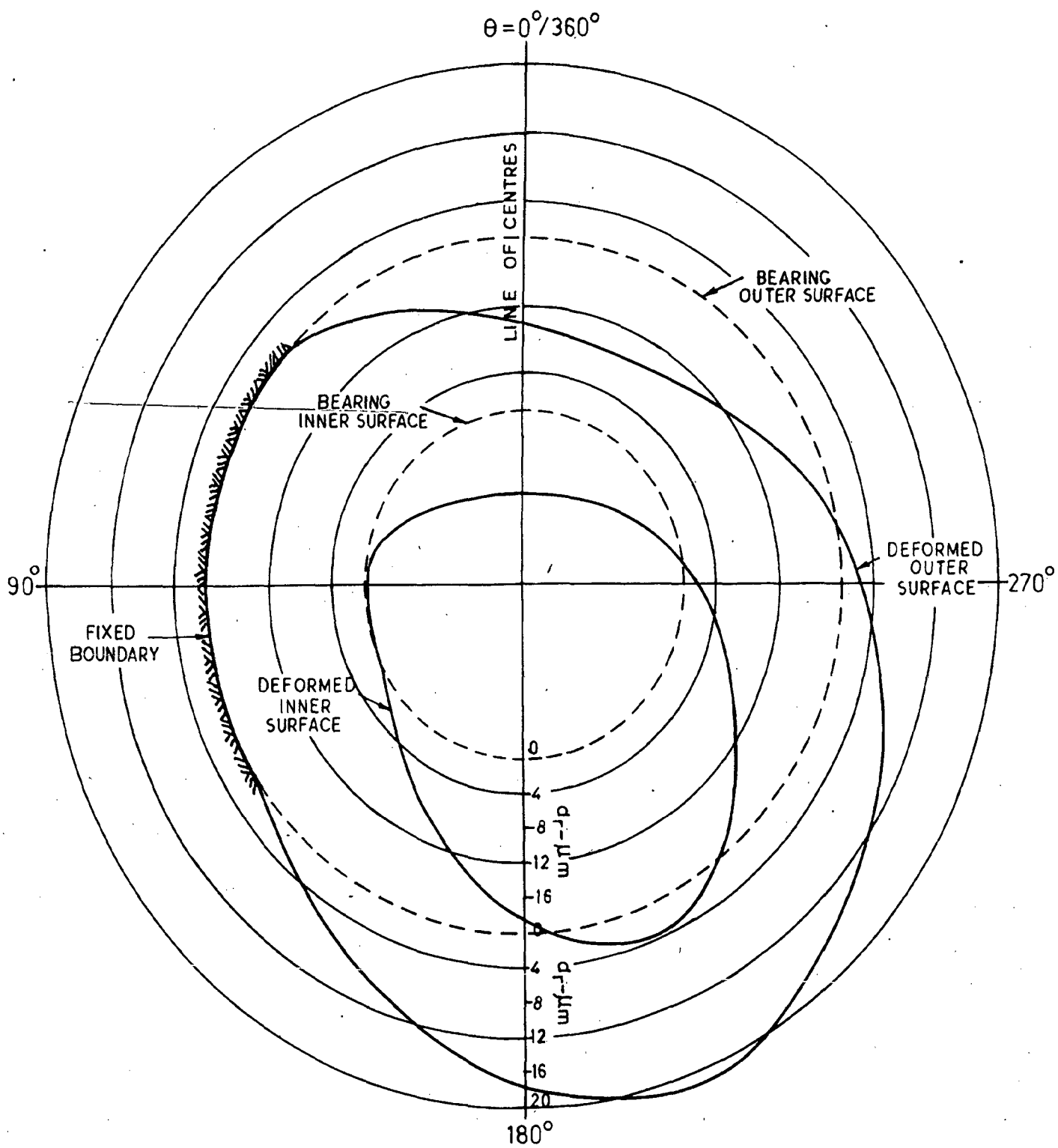


Fig.6-25d Deformation pattern of bearing body at 300 deg. crank angle

time (about 15 minutes on DEC-2050 computer). Table- 6.7 shows that as a result of deformation, the minimum film thickness increases in the case of elastothermohydrodynamic analysis. Hence, the possibility of the occurrence of metal to metal contact is less. The CPU time for the iterative solutions accounting for deformations of large magnitude is excessive, therefore, the minimum film thickness values for the entire duty cycle has not been calculated. Table- 6.7 gives the computed ETHD orbit points for only a finite crank rotation.

6.5 COMPUTATIONAL CPU TIME

The performance characteristics of the big-end bearing under various conditions along with discussions are presented in the section 6.4 of this Chapter. Information regarding the computer time needed on DEC- 2050 system in getting those results are tabulated below.

Table - 6.8

CPU time required for the cases studied.

Case studied	Remark	CPU time in hours
Selection of numerical method	-	1.5
Isoviscous lubricants	Full orbit	7
piezoviscous lubricants	Full orbit	12
piezo-Thermal effects on viscosity	Full orbit	18
Non-Newtonian lubricants(C.S.S)*	Full orbit	13
Non-Newtonian lubricants(C.F.M)**	Partial orbit	2/(13)\$
Ungrooved bearing(parallel axes)	Full orbit	7
Ungrooved bearing(skewed axes)	Full orbit	7
Elastothermohydrodynamic lubrication	Partial orbit	6.5/(80)\$

The total CPU time used in computing the results presented in this thesis is about 74 hours.

* Cubic shear stress law model.

** Curve fit model

\$ Estimated CPU time in hours to obtain full orbit.

6.6 CONCLUSIONS

6.6.1 Algorithm and the Computer Program

The solution algorithm presented in Chapter 5, is general and may be useful to the designers of the big-end bearing for any type of engine. The algorithm and the computer program were made efficient and economical by incorporating the following features.

1. Boundary conditions were introduced at the element stage to minimize computer core storage requirements.
2. For the time marching scheme Euler-Cauchy's predictor-corrector method was used which was found to be more suitable in comparison to Runge-Kutta or higher-order predictor-corrector method for this problem.
3. The frontal solver was used to economize the computer memory storage requirements for the computation of deformations in the big-end bearing body.
4. The subroutine used for non-Newtonian lubricants is based on a general algorithm which can handle any non-Newtonian model.
5. The size of time steps, when adjusted properly for successive segments of a duty cycle on the basis of the load on the bearing and its variation, considerably improves the convergence of the solution.

The following time steps were found suitable.

Crank angle range (deg.)	time steps (deg.)
60 - 250	10
250 - 510	5
510 - 690	10
690 - 720 - 60	2

6.6.2 Bearing Performance

On the basis of the results presented in the preceding Sections of this Chapter for the big-end bearing of a Ruston-Hornsby 6VEB-X, Mk-III engine, the following general conclusions can be drawn.

1. For the rigid bearing with an isoviscous lubricant, the bearing centre orbit, variations of the minimum film thickness and the maximum film pressure are close to those reported in the literature, which validates the algorithm structure and the computer program.
2. In the case of piezoviscous lubricants, the effect of piezoviscosity on the minimum film thickness and the maximum film pressure is not significant. This effect is, however, noticeable at high loads. Power loss is maximum near the top-dead-centre position of the crank.
3. The temperature effect on viscosity causes a significant change in the minimum film thickness. In the case of rigid bearing with lubricants having piezo-thermal viscosity characteristics, the minimum film thickness is about 18 percent smaller than that in the isoviscous case. The maximum temperature rise is about 10°C to 30°C and due to reduction in viscosity, power loss also decreases. In this case, the minimum film thickness is closer to the experimental value in comparison to other cases studied.
4. For the non-Newtonian lubricants, the load capacity of the bearing decreases. Hence, the values of the minimum film thickness for the bearing with non-Newtonian lubricants are found smaller to those for the Newtonian case.

5. For studying the characteristics of big-end bearing with non-Newtonian lubricants, cubic shear stress law and curve-fit models are used to represent the constitutive equations for non-Newtonian behaviour. By comparing the results of both the models, it is noticed that cubic shear stress law (constant $K = 0.58$) gives almost the same results as obtained using the curve-fit model.
6. Replacing a 12.7mm (0.5in) wide full circumferential groove by a supply hole significantly affected the characteristics of the big-end bearing. For this ungrooved bearing, two cases have been studied and the following conclusions are drawn:
 - (a) Parallel axes case:- In the case of ungrooved bearing with parallel axes, the values of the minimum film thickness are considerably larger and the values of the maximum film pressure smaller than those obtained in the corresponding grooved bearing for the entire duty cycle.
 - (b) Skewed axes case:- A small amount of misalignment between pin and bearing axes decreases the value of the minimum film thickness. Hence, if misalignment increases, there is a possibility of metal to metal contact at the edge of the bearing.
7. In the elastothermohydrodynamic (ETHD) study, the deformation in the bearing body is found significant. The temperature rise and power loss are smaller than those in the rigid case. The ETHD case represents the realistic problem but is computationally quite expensive.
8. For the grooved bearing configuration, the minimum value of film thickness occurs in the vicinity of 270° crank angle for

all the cases studied. For the ungrooved bearing with parallel axes, the position of occurrence of the minimum film thickness is also at 270° crank angle, but in the corresponding bearing with skewed axes, it occurs at 220° crank angle.

9. Isoviscous study of rigid bearing takes the minimum CPU time in comparison to the other cases studied, but in the isoviscous case, the value of the minimum film thickness is not comparable with that of available experimental value. The ETHE case represents the more realistic solution of the big-end bearing problem but it is computationally more expensive. However, the case of rigid bearing with non-Newtonian lubricants or with lubricants having piezo-thermal viscosity characteristics takes reasonable CPU time and the corresponding results are also closer to the available experimental results. Hence, for accurate design one has to consider the effects of ETHE lubrication, but for practical purpose one may design or analyze the big-end bearing on the basis of the results for rigid bearing with lubricants having piezo-thermal viscosity characteristics or non-Newtonian behaviour.

CLOSURE

The kinematics of the big-end bearing and its dynamic loading are quite complex. The big-end bearing, therefore, has been a subject of extensive investigations, both theoretical and experimental, by a number of authors, particularly during the last two decades. A survey of the literature on the big-end bearing indicates that the study of some aspects such as variation of viscosity of lubricants due to temperature and pressure or due to its dependence on shear strain rate and misalignment in the bearings need more attention. To the best of the author's knowledge, most of the studies on the big-end bearing, have assumed the viscosity as constant. With this assumption, accurate solutions of the big-end bearing problems can not be obtained.

An analysis of the big-end bearing, taking into account the variation of viscosity, is rather complicated. In this thesis, an endeavour is made to include the viscosity variation due to pressure and temperature, in the analysis of the big-end bearing.

The author has not come across any literature on the analysis of the big-end bearings having non-Newtonian lubricants. For heavy duty engines, lubricants with specific properties are required which are often achieved by mixing various additives such as oxidation inhibitor, corrosion inhibitor, viscosity index improver, detergents, dispersants, defoaming agents in the base oils. Such lubricants show nonlinear relationship between shear stress and shear strain rate (non-Newtonian behaviour).

It is well known today that both the elastic deformation of bearing surface and the variation of viscosity of lubricants with

pressure can have a significant effect on the bearing performance. The elastic distortion of the big-end bearing due to hydrodynamic pressure is often larger than the nominal radial clearance. Hence, the present problem is also extended to study the effect of elastothermohydrodynamic lubrication on the performance of the big-end bearing.

The big-end bearing problem, being complex and challenging, attracts a large number of investigators. With the increasing computing power available, more and more complicated problems would be solved to obtain very realistic solutions for the big-end bearing. In this regard, the author feels that the big-end bearing problem would be analyzed taking into account the effects of contamination of oils and variation of viscosity of non-Newtonian lubricants with temperature. The solutions of complex problems obtained through involved algorithms need experimental validation. The author hopes that parallel experimental work on the big-end bearing will match theoretical investigations.

REFERENCES

1. Burwell, J.T. The Calculated Performance of Dynamically Loaded Sleeve Bearings, J. Applied Mechanics, p. A-231, Sept. 1947
2. Blount, E.A. Design Factors Influencing the Fatigue Resistance of Connecting-Rod Big-End Bearing, Proc.IME, Vol. 175, No. 10, p. 513, 1961
3. Booker, J.F. Dynamically Loaded Journal Bearings: Mobility Method of Solution, J. of Basic Engineering, p. 537, Sept.1965
4. Butcher, A.E. Developments in the Measurement of Oil-Film Thickness in Dynamically Loaded Bearings, Proc. IME, Vol. 182, Pt 3G, p. 105, 1967-68
5. Booker, J.F. Dynamically Loaded Journal Bearings: Maximum Film Pressure, Trans. ASME, J. of Lubrication Technology, p. 534, July, 1969
6. Booker, J.F. Dynamically-Loaded Journal Bearings: Numerical Application of the Mobility Method, J. of Lubrication Technology, p. 168, Jan. 1971
7. Blok, H. Full Journal Bearings Under Dynamic Duty: Impulse Method of Solution and Flapping Action, J. of Lubrication Technology, p. 168, April 1975
8. Boncompain, R. and Frene, J. Thermohydrodynamic Analysis of a finite Journal Bearing: Static and Dynamic Characteristics, Proc. 6th Leeds-Lyon Symposium on Tribology (Thermal Effects in Tribology), p.33, Sept. 1979
9. Carl, T.E. An Experimental Investigation of a Cylindrical Journal Bearing Under Constant and Sinusoidal Loading, Proc. IME, Vol. 178, Pt 3N, p. 100, 1963-64
10. Campbell, J., Love, P.P., Martin, F.A. and Rafique S.O. Bearings for Reciprocating Machinery: A Review of the Present State of Theoretical, Experimental and Service Knowledge, Proc. IME, Vol. 182, Pt. 3A p. 51, 1967-68
11. Cameron, A. Basic Lubrication Theory, Longmans Green and Co. London
12. DeHart, A.O. and Harwick, D.H. Engine Bearings Design:1969, Trans. SAE, Paper No. 690008, p. 69, 1969
13. Davison, C.H. Plain Bearings for the High Speed Diesel Engine Trans. SAE, Paper No. 760009, p, 1, 1976
14. Darby, R. Viscoelastic Fluids: An Introduction to their Properties and Behaviour, Marcel Dekker INC New York, p. 192, 1976

15. Furuhashi, S. The Temperature of a Crankpin Bearing of an Automobile Engine, Trans. ASLE, p. 203, 1967
16. Fantino, B., Frene, J. and DuParquet, J. Elastic Connecting-Rod Bearing with Piezoviscous Lubricant: Analysis of the Steady-State Characteristics, J. of Lubrication Technology, Vol. 101, p. 190, April 1979
17. Frene, J., Desailly, R. and Fantino, B. Hydrodynamics of an Elastic Connecting-Rod Bearing: Comparison of Theoretical and Experimental Results, Proc. of 5th Leeds Symposium on Tribology, Leeds, p. 329, Sept. 1978
18. Fantino, B., Godet, M. and Frene, J. Dynamics Behaviour of an Elastic Connecting-Rod Bearing: Theoretical Study, Proc. SAE, Studies of Engine Bearings and Lubrication, SP 539, No. 830307, p. 23, 1983
19. Fantino, B., and Frene, J. Comparison of Dynamic Behaviour of Elastic Connecting-Rod Bearing in Both Petrol and Diesel Engines, J. of Tribology, Vol. 107, p. 87, Jan. 1985
20. Goodwin, G. and Holmes, R. On the Continuous Monitoring of ~~Oil-Film Thickness in an Engine Bearing~~, Proc. IME, Vol. 192, p. 371, 1978
21. Goodwin, G. and Holmes, R. On the Continuous Temperature Monitoring of an Engine Bearing, Proc. IME, Vol. 191, p. 161, 1977
22. Goodwin, G. and Holmes, R. On Bearing Deformation and Temperature Distribution in Dynamically-Loaded Engine Bearings, Proc. IME, Paper C2/82, p. 9, 1982
23. Goenka, P.K. Analytical Curve-Fits for Solution Parameter of Dynamically Loaded Journal Bearings, J. of Tribology, Vol. 106, p. 421, Oct. 1984
24. Goenka, P.K., Dynamically Loaded Journal Bearings: Finite Element Method Analysis, J. of Tribology, Vol. 106, p. 429, Oct. 1984
25. Gerald, C.F. Applied Numerical Analysis, Addison Wesley Publishing Co. California, London.
26. Harrison, W.J. The Hydrodynamical Theory of the Lubrication of a Cylindrical Bearing Under Variable Load, and of a pivot Bearing, Trans. Cambridge Philosophical Society, Vol. 22, p. 373, 1920
27. Hersey, M.D. and Snapp, R.B. Testing Dynamically Loaded Bearings-I A Short History of Bearing Test Machines, Trans. ASME, p. 1247, Aug. 1957

28. Horsnell, R. and McCallion, H. Prediction of Some Journal-Bearing Characteristics Under Static and Dynamic Loading, Proc. IME, Lubrication and Wear Convention, p. 126, 1963
29. Hiruma, M. and Furuhashi, S. Measurement of the Journal Locus in the connecting-Rod Big-End Bearing of an Automobile Gasoline Engine, J. of Lubrication Technology, p. 249, April 1973
30. Hsu, Y.C. and Saibel, E. Slider Bearing Performance With a Non-Newtonian Lubricant, Trans. ASLE, Vol. 8, p. 191, 1965
31. Huebner, K.H. A Three-Dimensional Thermohydrodynamic Analysis of Sector Thrust Bearings, Trans. ASLE, 1973
32. Huebner, K.H. Application of Finite Element Methods to Thermohydrodynamic Lubrication, International Journal for Numerical Methods in Engineering, Vol. 8, p. 139, 1974
33. Huebner, K.H. The Finite Element Method for Engineers, John Wiley & Sons, New York, 1975
34. Hamming, R.W. and Feigenbaum, E.A. Introduction to Applied Numerical Analysis, McGraw-Hill-Book-Co. INC, New York
35. Hughes, W.F. and Brighton, J.A. Schaum's Outline of Theory and Problems of Fluid Dynamics, Schaum Publishing Co. New York, p. 232, 1967
36. Jain, S.C., Sinhasan, R., and Singh, D.V., Elastohydrodynamic Analysis of Cylindrical Journal Bearing with a Flexible Bearing Shell, Wear, Vol. 78, p. 325, 1982
37. Johnson, T.W. and O'Shaughnessy, T. Measurement of Temporary and Permanent Shear with the Instron Capillary Rheometer, Trans. SAE, Paper No. 770377, p. 1607, 1977
38. Lloyd, T., Horsnell, R. and McCallion, H. An Investigation into the Performance of Dynamically Loaded Journal Bearings: Theory, Proc. IME, Vol. 181, Pt 3B, p. 1, 1966-67
39. Lloyd, T., Horsnell, R. and McCallion H. An Investigation into the Performance of Dynamically Loaded Journal Bearings: Design Study, Proc. IME, Vol. 181, Pt 3B, p. 28, 1966-67
40. Lloyd, T. and McCallion, H. A Computer Program for the Design of Reciprocating Engine Bearings, Proc. IME, Vol. 182, Pt 3L, p. 193, 1967-68
41. Lloyd, T. and McCallion, H. Journal Bearings without Circumferential Symmetry Under Dynamic Loading, Proc. IME, Vol. 183, Pt 3P, p. 1 1968-69
42. LaBouff, G.A., and Booker, J.F. Dynamically Loaded Journal Bearings: A Finite Element Treatment for Rigid and Elastic Surfaces, J. of Tribology, Vol. 107, p. 505, Oct. 1985

43. Middleton, V., Dudley, B.R. and McCallion, H. An Investigation into the Performance of Dynamically Loaded Journal Bearings: Experiment, Proc. IME, Vol. 181, Pt 3B, p. 9, 1966-67
44. Martin, F.A. and Booker, J.F. Influence of Engine Inertia Forces on Minimum Film Thickness in Connecting-Rod Big-End Bearings, Proc. IME, Vol. 181, Pt 1, No. 30, p. 749, 1966-67
45. Martin, F.A. Developments in Engine Bearing Design, Tribology International, Vol. 16, p. 147, June 1983
46. Murty, K.G., Note on a Bard-type Scheme for Solving the Complementarity Problems, Opsearch, Vol. 11, p. 123, 1974
47. Oh, K.P. and Goenka, P.K. The Elastohydrodynamic Solution of Journal Bearings under Dynamic Loading, J. of Tribology, Vol. 107, p. 389, July 1985
48. Pigott, R.J.S. and Walsh, B.R., Universal Bearing Tester, Trans. ASME, p. 1267, Aug. 1957
49. Patel, M.J. Influence of Oil Balls on Premature Overlay Removal of Diesel Engine Connecting-Rod Bearings, Trans. SAE, Paper No. 810501, p. 1, 1981
50. Prokop'ev, V.N. Designing Plain Bearings for Reciprocating Machines, J. of Russian Engg. (Vestnik Mashinostroeniya), Vol. 54, No. 3, p. 20, 1974
51. Pinkus, O. and Sternlicht, B. Theory of Hydrodynamic Lubrication, McGraw Hill Book Co. INC New York, 1961
52. Russell, A.E. Some Bearing Tests Made With a Machine Producing Impulsive Loading, Proc. IME, Vol. 172, p. 1047, 1958
53. Radermacher, K. Experimental Investigation into Cylindrical Plain Bearings Under Loads Varying in Magnitude and Direction, Proc. IME, Vol. 178, Pt 3N, p. 120, 1963-64
54. Ross, J.M. and Slaymaker, R.R. Journal Center Orbits in piston Engine Bearings, Trans. SAE, Paper No. 690114, p. 548, 1969
55. Ross, J.M. Bearing Orbit Analysis, J. of Machine Design, p. 140, Oct. 1971
56. Ritchie, G.S. The Prediction of Journal Loci in Dynamically Loaded Internal Combustion Engine Bearings, Wear, Vol. 35, No. 2, p. 291, Dec. 1975
57. Raimondi, A.A. and Boyd, J.A. A Solution for the Finite Journal Bearing and its Application to Analysis and Design: III, Trans. ASLE, Vol. 1, No. 1, p. 194, April 1958
58. Swift, H.W. Fluctuating Loads in Sleeve Bearings, J. of the ICE Vol. 5, p. 161, 1937

59. Snapp, R.B. and Hersey, M.D. Testing Dynamically Loaded Bearings-II, A Diesel Engine Bearing Test Machine, Trans. ASME, p. 1260, Aug. 1957
60. Shelly, P.D. and Ettles, C. A Finite Element Method for the Calculation of Locus Paths in Dynamically Loaded Bearings, Proc. IME, Vol. 187 p. 79, 1983
61. Stewart, R.M. The Relationship Between Oil Viscosity and Engine Performance-A Literature Search, Trans. SAE, Paper No. 770372, p. 1574, 1977
62. Shaw, M.C. and Macks, F. Analysis and Lubrication of Bearings, McGraw Hill Book Co. INC New York, 1949
63. Smith, E.H., Temperature Variations in Crankshaft Bearings, Proc. 9th Leeds Symposium on Tribology, Paper iv(iii), p. 97, Leeds 1982 (Butterworth 1983)
64. Tempel, L.V., Moes, H. and Bosma, R. Numerical Simulation of Dynamically Loaded Flexible Short Journal Bearings, J. of Tribology, Vol. 107, p. 396 July 1985
65. Tempel, L.V., Moes, H. and Bosma, R. Starvation in Dynamically Loaded Flexible Short Journal Bearings, J. of Tribology, Vol. 107, p. 516, Oct. 1985
66. Wada, S. and Hayashi, H. Hydrodynamic Lubrication of Journal Bearings by Pseudoplastic Lubricants (Part-I, Theoretical Studies), Bull. JSME, Vol. 14, p. 268, 1971
67. Wada, S. and Hayashi, H. Hydrodynamic Lubrication of Journal Bearings by Pseudoplastic Lubricants (Part-II, Experimental Studies), Bull. JSME, Vol. 14, p. 279, 1971
68. Wilcock, D.F. and Booser, E.R. Bearing Design and Application, McGraw Hill Book Co. INC, New York, 1957
69. Zienkiewicz, O.C., The Finite Element Method, McGraw Hill Book Co. INC, New York, 1977

LIST OF PUBLICATIONS ON THE STUDIES
CARRIED OUT IN THIS THESIS

1. A Numerical Integration Scheme to Find Motion Trajectory of Big-End Bearing Centre, J. of The Institution of Engineers (India), Vol. 66, Part ME6, p. 166, May 1986
2. Analysis of a Big-End Bearing - A Finite Element Approach, Wear, Vol. 114, p. 275, 1987
3. Analysis of Big-End Bearing Having Non-Newtonian Fluid's, Accepted for publication in the journal of ASLE
4. A Study of Big-End Bearing with Piezoviscous Lubricants, To appear in MICROTECNIC Vol. No. 1/88, 1988
5. Performance of Big-End Bearings - A Review, Proc. of National Seminar on Bearings held on 17-18 Sept. 1987 at Madras (India)
6. Analysis of a Big-End Bearing - A Finite Element Approach, Accepted for publication as a Technical Note in Wear
7. Performance Characteristics of an Ungrooved Big-end Bearing with Misalignment, Communicated for Annual Meeting of ASLE

APPENDIX A-1

List of Non-Newtonian Oils

The following is the list of some of the oils [37] with code and viscosity index (VI) improver type. (All 10W-40 oils)

Commercial Oils

Code	VI improver type
C-1	Ethyl -propylene
C-2	Styrene-ester
C-3	Methacrylate
C-4	Ethylene-propylene
C-5	Methacrylate
C-6	EP and methacrylate

Experimental Oils

E-1	Hydrogenerated diene-styrene
E-2	Hydrogenerated diene-styrene
E-3	Methacrylate
E-4	Styrene-ester
E-5	Ethylene-propylene

In the literature [61], it has been shown that at low shear rate (below $10^3(\text{sec.}^{-1})$) as well as at high shear rate (above $10^6(\text{sec.}^{-1})$), the apparent viscosity has become constant. This condition has also been applied in the present calculation.

APPENDIX A-2

Heat Balance Condition

(1) To obtain the heat rate (Q_1) at the interface of lubricant and bearing inner surface, the following heat conduction equation is applied.

$$Q_1 = -K_o 2\pi R_1 L \left. \frac{\delta T}{\delta r} \right|_{r=R_1} \quad (\text{A.2.1})$$

or

$$\bar{Q}_1 = \frac{Q_1}{2\pi K_o T_o L} = -\bar{R}_1 \left. \frac{\delta \bar{T}}{\delta r} \right|_{\bar{r}=\bar{R}_1} \quad (\text{A.2.2})$$

where, Eq.(A.2.2) is written in nondimensional form and K_o is the thermal conductivity of oil, R_1 is the bearing inner radius, L is the axial length of bearing portion from which heat conduct and $\frac{\delta T}{\delta r}$ is the temperature gradient in radial direction.

(2) Heat rate (Q_2) from bearing inner surface to the bearing outer most surface (considering only the conduction of heat in radial direction) is given by

$$Q_2 = \frac{K_m 2\pi L}{R_o \log \frac{R_o}{R_1}} (T_b - T_s) = \frac{T_b - T_s}{\Omega_m} \quad (\text{A.2.3})$$

where, T_b and T_s are the bearing inner and outer most surface temperature respectively, R_o is the bearing outer most radius and Ω_m is defined as the heat resistance of the bearing body material.

(3) Heat rate from bearing outer most surface to the surrounding is given by

$$Q_3 = h_a 2\pi R_o L (T_s - T_a) = \frac{T_s - T_a}{\Omega_a} \quad (\text{A.2.4})$$

where, h_a is the convection heat transfer coefficient, T_a is the surrounding temperature and Ω_a is the heat resistance due to convection of heat.

Now applying the condition that $Q_2 = Q_3$ and by eliminating T_3 from equations (A.2.3-A.2.4), the following equation is obtained.

$$Q_2 = Q_3 = \frac{T_b - T_a}{\Omega_T} \quad (\text{A.2.5})$$

where, Ω_T is the total heat resistance and defined as

$$\Omega_T = \Omega_m + \Omega_a = \frac{1}{K_m 2\pi L} \log_e \frac{R_o}{R_i} + \frac{1}{h_a 2\pi R_o L}$$

From Eq.(A.2.5), the heat rate Q_2 or Q_3 in nondimensional form may be converted as

$$\bar{Q}_2 = \bar{Q}_3 = \frac{(\bar{T}_b - \bar{T}_a)}{\bar{\Omega}_T} \quad (\text{A.2.6})$$

which gives the normalizing factor for Ω_T as

$$\bar{\Omega}_T = 2\pi K_o L \Omega_T$$

(4) Now equate \bar{Q}_1 to \bar{Q}_2 or \bar{Q}_3 , the following relation is obtained which has been used to calculate bearing inner surface temperature (\bar{T}_b).

$$\bar{T}_b - \bar{T}_a = -\bar{R}_1 \bar{\Omega}_T \left. \frac{\delta \bar{T}}{\delta \bar{r}} \right|_{\bar{r}=\bar{R}_1} \quad (\text{A.2.7})$$

Thermal Constants

Oil used SAE - 30

Properties of SAE-30 oil at different temperature [11]

Temperature	25°C	40°C	100°C	Value of relation constants
Density @ (Kg/m ³)	886	876	839	b = 1361 a = 0.023669
Absolute viscosity μ_o (mPa.S)	229.474	98.725	10.50	$\theta_T = 23.3$ $\beta_T = 0.032/^\circ\text{C}$

Vogel formula

$$\mu_a = a \exp \{b/(T+\theta_T)\}$$

Reynolds formula $\mu_a = \mu_o \exp \{-\beta_T(T-T_o)\}$ Supply temperature $T_o = 89^\circ\text{C}$ density $@_o = 850 \text{ Kg/m}^3$ Viscosity at supply temperature $\mu_o = 14.95 \text{ mPa.S} (2.17 \times 10^{-6} \text{ reyn})$ From Reference [8]Lubricant thermal conductivity $k_o = 0.13 \text{ W/m}^\circ\text{C}$ or $\text{N/S}^\circ\text{C}$ or $\text{Joules/Sec.m}^\circ\text{C}$ Specific heat $C_v = 2000 \text{ J/Kg } ^\circ\text{C}$ Bearing material thermal conductivity $K_m = 51.9 \text{ W/m}^\circ\text{C}$

$$\bar{K}_o = \frac{\mu_o \Omega^2 R^2}{K_o T_o} = 0.05265, \quad (\text{Eq. (2.24)})$$

$$\bar{K}_v = \frac{@_o C_v R \Omega c}{K_o} = 6891.21, \quad (\text{Eq. (2.24)})$$

Peclet number $= (\bar{K}_v / \bar{R}) = 6891.21 / 1230 = 5.6$ Calculation of thermal total resistance (\bar{N}_T)Value of $R_o = 0.1590 \text{ m} (6.25 \text{ in})$ Ref. [42]

$$R_1 = 0.1016 \text{ m (4.0 in)}$$

In case of forced convection heat transfer, the value of h_m (heat transfer coefficient) can be taken quite large, hence using $h_m = 2000 \text{ W/m}^2 \text{ }^\circ\text{C}$ in the case of splashed lubrication system.

$$\begin{aligned} \bar{\theta}_T &= \frac{K_o}{K_m} \log_e \frac{R_o}{R_1} + \frac{K_o}{h_m R_o} \\ &= 0.0011 + 0.0004 \\ &= 0.0015 \end{aligned}$$

and

$$\bar{\beta}_T = \beta_T \times T_o = 2.848$$

APPENDIX A-3

Predictor-Corrector Formulae

The higher-order predictor-corrector formulae by Adams-Moulton [25] are given as

Predictor:

$$\overset{P}{e}_{i+1} = e_i + \frac{\delta \bar{t}}{24} (55\dot{e}_i - 59\dot{e}_{i-1} + 37\dot{e}_{i-2} - 9\dot{e}_{i-3}) \quad (\text{A.3.1})$$

$$\overset{P}{\beta}_{i+1} = \beta_i + \frac{\delta \bar{t}}{24} (55\dot{\beta}_i - 59\dot{\beta}_{i-1} + 37\dot{\beta}_{i-2} - 9\dot{\beta}_{i-3})$$

Corrector :

$$\overset{C}{e}_{i+1} = e_i + \frac{\delta \bar{t}}{24} (9\dot{e}_{i+1} + 19\dot{e}_i - 5\dot{e}_{i-1} + \dot{e}_{i-2}) \quad (\text{A.3.2})$$

$$\overset{C}{\beta}_{i+1} = \beta_i + \frac{\delta \bar{t}}{24} (9\dot{\beta}_{i+1} + 19\dot{\beta}_i - 5\dot{\beta}_{i-1} + \dot{\beta}_{i-2})$$

The predictor-corrector relations due to Euler-Cauchy modified formula are given as

Predictor:

$$\overset{P}{e}_{i+1} = e_{i-1} + 2 \delta \bar{t} \dot{e}_i \quad ; \quad \overset{P}{\beta}_{i+1} = \beta_{i-1} + 2 \delta \bar{t} \dot{\beta}_i \quad (\text{A.3.3})$$

$$\overset{P}{\ddot{e}}_{i+1} = \ddot{e}_{i-1} + 2 \delta \bar{t} \ddot{e}_i \quad ; \quad \overset{P}{\ddot{\beta}}_{i+1} = \ddot{\beta}_{i-1} + 2 \delta \bar{t} \ddot{\beta}_i \quad (\text{A.3.3})$$

Corrector:

$$\overset{C}{e}_{i+1} = e_i + (1/2) \delta \bar{t} (\dot{e}_{i+1} + \dot{e}_i) \quad ; \quad \overset{C}{\beta}_{i+1} = \beta_i + (1/2) \delta \bar{t} (\dot{\beta}_{i+1} + \dot{\beta}_i) \quad (\text{A.3.4})$$

The Euler's predictor formula is given as

$$\overset{P}{e}_{i+1} = e_i + \delta \bar{t} \dot{e}_i \quad ; \quad \overset{P}{\beta}_{i+1} = \beta_i + \delta \bar{t} \dot{\beta}_i \quad (\text{A.3.5})$$

The backward difference formula is

$$\overset{B}{\dot{e}}_i = (\dot{e}_i - \dot{e}_{i-1}) / \delta \bar{t} \quad ; \quad \overset{B}{\dot{\beta}}_i = (\dot{\beta}_i - \dot{\beta}_{i-1}) / \delta \bar{t} \quad (\text{A.3.6})$$

APPENDIX A-4

DATA FOR THE RUSTON-HORNSBY 6 VEB-X, Mk-III CONNECTING-ROD BIG-END BEARING USED THROUGHOUT THIS WORK.

Engine 6 cylinder, 600 rev/min, 600 b.h.p., turbo-charged diesel, four stroke, in line.

Bearing length (total) = 127.0 mm (5.0 in)

Bearing grooving central circumferential, 12.7 mm (0.5 in) wide

Bearing length of one land = 57.15 mm (2.25 in)

Radial clearance = 82.55 μ m (0.00325 in)

Bearing diameter (inner) = 203.2 mm (8.0 in)

Bearing diameter (outer) = 318 mm (12.52 in)

Length of connecting-rod = 782.3 mm (30.8 in)

Crank radius = 184.1 mm (7.25 in)

Engine speed (600 rev/min) = 62.84 rad/s.

Weight of piston and gudgeon pin = 805.08 N (181.0 lbf)

Weight of connecting-rod = 800.64 N (180.0 lbf)

Approximate reciprocating weight = $\frac{2}{3} \times 800.64 = 533.76$ N (120.0 lbf)

Approximate reciprocating weight = $\frac{1}{3} \times 800.64 + 805.08 = 1071.96$ N (241.0 lbf)

Estimated operating oil viscosity in bearing = 14.95 mPa.s (2.17×10^{-6} reyn)

Oil supply pressure = 0.2758 MPa (40.0 lbf/in²)

Bearing body material IRON [42]

Young's Modulus (E) = 107 GPa

Poisson's Ratio = 0.25

Thickness of bearing body = 57.4 mm [42]

Deformation coefficient $\bar{\phi} = 0.009229$

Table-A-4.1

Force components (SI units) on the connecting-rod big-end bearing of the Ruston-Hornsby 6VEB-X, Mk-III engine relative to the Cylinder axis

Crank angle θ_1 (deg.)	Big-End Bearing Forces, (kN)		
	F_{x1}	F_{y1}	Angle α (deg.)
0	115.34	-0.0	0.00
10	207.37	-17.28	-04.76
20	133.17	-27.92	-11.84
30	73.19	-33.38	-24.52
40	41.30	-37.43	-42.18
50	27.38	-41.11	-56.33
60	26.53	-45.01	-59.49
70	34.53	-49.15	-54.91
80	44.66	-52.18	-49.44
90	58.76	-54.58	-42.89
100	72.95	-55.33	-37.18
110	85.98	-54.13	-32.19
120	97.19	-50.75	-27.57
130	105.95	-45.37	-23.18
140	112.89	-38.28	-18.73
150	115.65	-29.57	-14.34
160	114.63	-19.88	-09.84
170	113.34	-09.96	-05.02
180	110.44	0.0	0.00
190	107.82	09.73	5.16
200	105.11	19.11	10.31

Table-A-4.1 Contd...

1	2	3	4
210	100.26	27.75	15.47
220	94.16	35.41	20.61
230	85.76	41.66	25.91
240	74.82	46.13	31.65
250	61.03	48.44	38.44
260	44.30	48.53	47.61
270	24.80	46.35	61.85
280	02.99	42.25	85.95
290	-20.34	36.68	119.01
300	-44.12	30.31	145.51
310	-67.12	23.78	160.49
320	-88.07	17.62	168.68
330	-105.77	12.17	173.43
340	-119.16	07.53	176.38
350	-127.52	03.58	178.39
360	-130.37	-0.0	180.00
370	-127.52	-03.58	181.61
380	-119.16	-07.53	183.62
390	-105.77	-12.17	186.57
400	-88.07	-17.62	191.32
410	-67.12	-23.78	199.51
420	-44.12	-30.31	214.49
430	-20.34	-36.68	240.99
440	02.99	-42.25	274.05
450	24.80	-46.35	298.15
460	44.30	-48.53	312.39

Table 4.1 Contd...

1	2	3	4
470	61.03	-48.44	321.56
480	74.82	-46.13	328.35
490	85.76	-41.66	334.09
500	94.16	-35.41	339.39
510	100.26	-27.75	344.53
520	104.35	-19.05	349.65
530	106.75	-09.69	354.81
540	107.51	0.0	360.00
550	106.76	09.69	365.19
560	104.35	19.05	370.35
570	100.26	27.75	375.47
580	94.16	35.41	380.61
590	86.87	41.86	385.73
600	77.04	46.57	391.15
610	63.96	49.11	397.51
620	49.06	49.68	405.36
630	31.40	47.95	416.78
640	13.06	44.70	433.47
650	-04.92	40.18	456.99
660	-18.06	35.74	476.81
670	-27.49	31.05	491.53
680	-28.25	26.78	496.53
690	-13.09	23.16	479.48
700	+15.71	18.43	409.55
710	51.37	10.89	371.97
720	115.34	0.0	360.00

APPENDIX A-5

EXPRESSION FOR FILM THICKNESS IN SKEW AXES SYSTEM

Definition: Fig.A-5.1a

O_p = origin of crank pin axes system (X', Y', Z')

O_b = origin of bearing axes system (X, Y, Z)

R = crank pin radius

R_b = $(R+c)$ = bearing radius

r = radial coordinate measured from O_p

e = eccentricity

h = film thickness

β = angular position of line of centres from fixed axis X'

The transformation from crank pin fixed axes X', Y', Z' to bearing axes X, Y, Z can be obtained by two rotations σ and δ , Fig.A-5.1b. The first rotation is about X' and the second rotation is about Y' . Right hand screw rule is followed in deciding the sign of the rotation. The transformation is

$$\begin{Bmatrix} X' \\ Y' \\ Z' \end{Bmatrix} = \begin{bmatrix} \cos\delta & 0 & -\sin\delta \\ \sin\sigma \sin\delta & \cos\sigma & \sin\sigma \cos\delta \\ \sin\delta \cos\sigma & -\sin\sigma & \cos\sigma \cos\delta \end{bmatrix} \begin{Bmatrix} x \\ y \\ z \end{Bmatrix} \quad (\text{A.5.1})$$

Therefore,

$$\begin{Bmatrix} x \\ y \\ z \end{Bmatrix} = \begin{bmatrix} \cos\delta & \sin\sigma \sin\delta & \sin\delta \cos\sigma \\ 0 & \cos\sigma & -\sin\sigma \\ -\sin\delta & \sin\sigma \cos\delta & \cos\sigma \cos\delta \end{bmatrix} \begin{Bmatrix} x' \\ y' \\ z' \end{Bmatrix} \quad (\text{A.5.2})$$

The equation of the bearing surface contour at any section with reference to the bearing or pin axes system, when the bearing centre O_b , and the pin centre O_p , Fig.A-5.1b, are coincident, can be written as

$$x^2 + y^2 = R_B^2 \quad (A.5.3)$$

Substituting the values of x and y from Eq.(A.5.2) into Eq.(A.5.3),

$$(x'\cos\delta + y'\sin\delta\sin\sigma + z'\sin\delta\cos\sigma)^2 + (y'\cos\sigma - z'\sin\sigma)^2 = R_B^2 \quad (A.5.4)$$

The skew components σ and δ being very small, $\sin\sigma$ and $\sin\delta$ may be taken as σ and δ respectively and $\cos\sigma$ and $\cos\delta$ both as unity. Also, neglecting the terms containing squares and products of small quantities, Eq (A.5.4) reduces to the following form:

$$x'^2 + y'^2 + 2x'z'\delta - 2y'z'\sigma = R_B^2 \quad (A.5.5)$$

If the bearing centre, O_B is shifted at an eccentricity e from the pin centre O_P , the equation (A.5.5) of the bearing surface contour is modified to the following form,

$$(x' - e \cos\beta)^2 + (y' - e \sin\beta)^2 + 2(x' - e \cos\beta)z'\delta - 2(y' - e \sin\beta)z'\sigma = R_B^2 \quad (A.5.6)$$

or neglecting comparatively small terms,

$$x'^2 - 2x'e \cos\beta + y'^2 - 2y'e \sin\beta + 2x'z'\delta - 2y'z'\sigma = R_B^2 \quad (A.5.7)$$

Eq.(A.5.7) can be expressed in cylindrical coordinates by

$$\begin{aligned} & \text{substituting, } x' = r\cos(\beta+\theta) \text{ and } y' = r\sin(\beta+\theta), \text{ and } x'^2 + y'^2 = r^2 \\ & r^2 - 2r\cos(\beta+\theta).e \cos\beta - 2r\sin(\beta+\theta).e \sin\beta \\ & + 2r\cos(\beta+\theta)z'\delta - 2r\sin(\beta+\theta)z'\sigma = R_B^2 \end{aligned} \quad (A.5.8)$$

or

$$\begin{aligned} & r^2 - 2r(e \cos(\beta+\theta)\cos\beta \\ & + e \sin(\beta+\theta)\sin\beta - z'\delta\cos(\beta+\theta) + z'\sigma\sin(\beta+\theta)) - R_B^2 = 0 \end{aligned} \quad (A.5.9)$$

or

$$r^2 - 2r(e \cos\theta - z'\delta\cos(\beta+\theta) + z'\sigma\sin(\beta+\theta)) - R_B^2 = 0 \quad (A.5.10)$$

Solving for r , and neglecting the terms containing squares and products of the small quantities,

$$r = e \cos\theta - z'\delta \cos(\beta+\theta) + z'\sigma\sin(\beta+\theta) + R_B \quad (A.5.11)$$

At any section, the film thickness, h is given by

$$h = r - R$$

Hence, the expression for film thickness, when bearing axes are skewed with respect to pin axes, can be obtained from Eqs. (A.5.11 and A.5.12) and relation $R_B = R + c$, such as

$$h = c + e \cos\theta - z'\delta \cos(\beta + \theta) + z'\sigma \sin(\beta + \theta) \quad (\text{A.5.13})$$

Using the normalizing factors, the nondimensional film thickness is

$$\bar{h} = 1 + \bar{e} \cos\theta - \bar{z}' \bar{R} \delta \cos(\beta + \theta) + \bar{z}' \bar{R} \sigma \sin(\beta + \theta) \quad (\text{A.5.14})$$

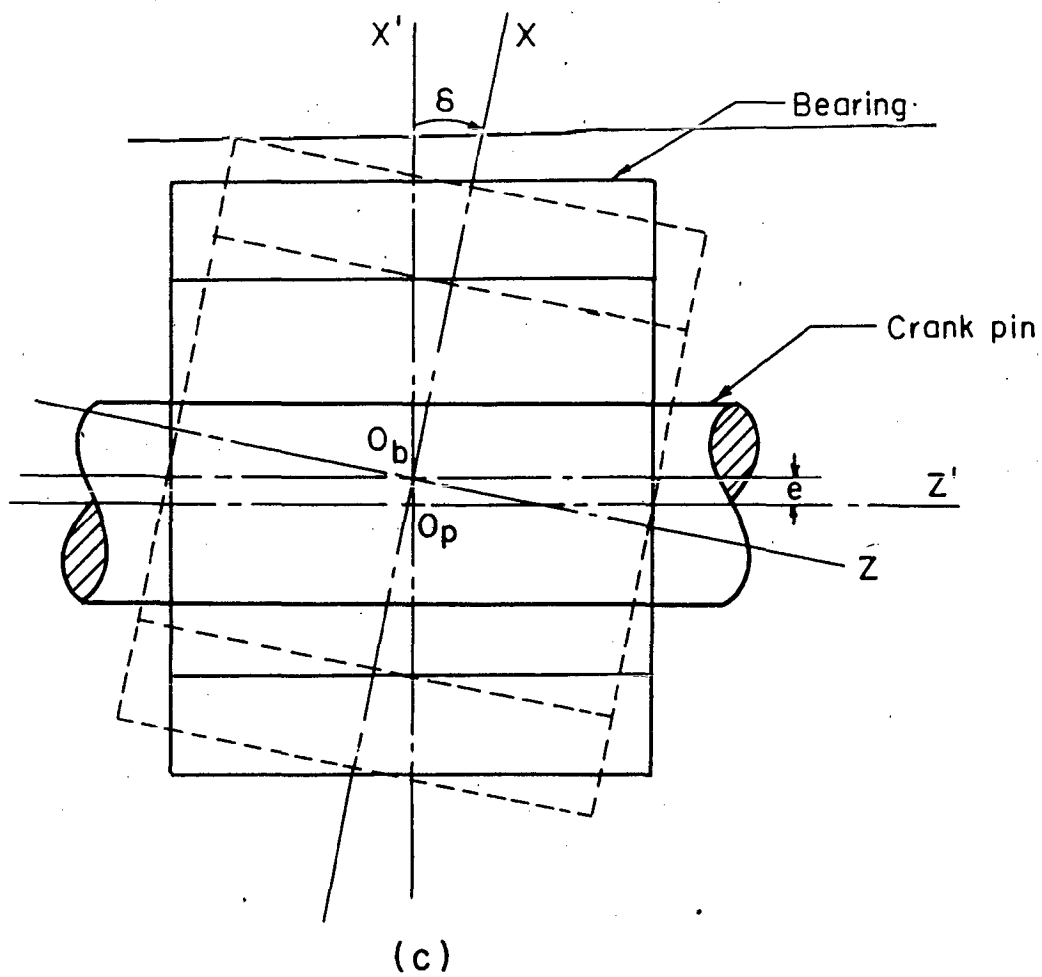
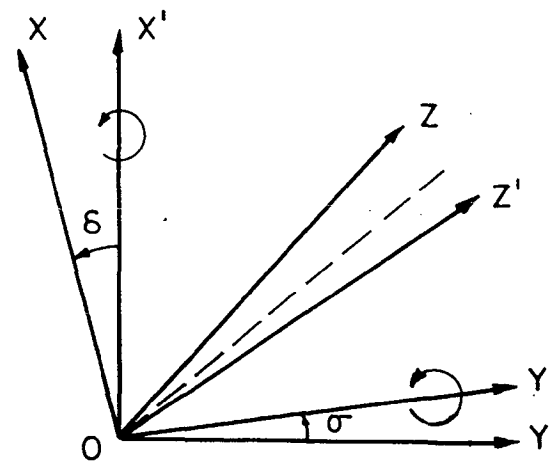
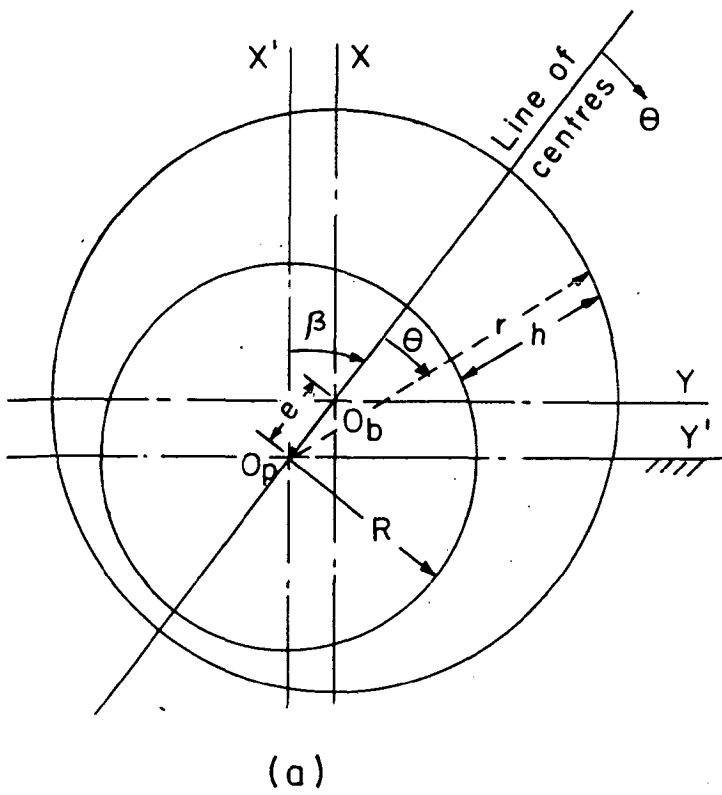


Fig. A-5-1 Axes misalignment in bearing system

APPENDIX A-6

THE BIG-END BEARING EQUILIBRIUM LOCUS

The big-end bearing centre orbit is calculated point by point using a time marching scheme. Initial conditions at any arbitrarily selected crank angle are required to compute the points on the orbit. The initial conditions are, however, not known a-priori. The values of ϵ and β obtained considering the wedge action alone is a good approximation of the initial conditions to compute the orbit points. For a selected crank angle, the value of eccentricity ratio ϵ can be iteratively computed at which the resultant of the fluid-film force components along and perpendicular to the line of centres, is equal to the force on the bearing. The attitude angle is then readily obtained from the values of the two fluid-film force components, which in turn gives β , Fig.4.4.

In order to have an option to calculate the bearing orbit points starting from any crank angle position, the values of ϵ and β are computed for the bearing load, Fig.4.2, considering the wedge action alone, at various crank angles. The equilibrium locus of ϵ and β is given in Fig.A-6.1, which is useful for selecting a suitable crank angle as a starting point at which the change in the values of ϵ or β is not steep. From the Fig.A-6.1, it is seen that any crank angle lying, for example, between 70° and 180° is suitable for good convergence of the orbit points.

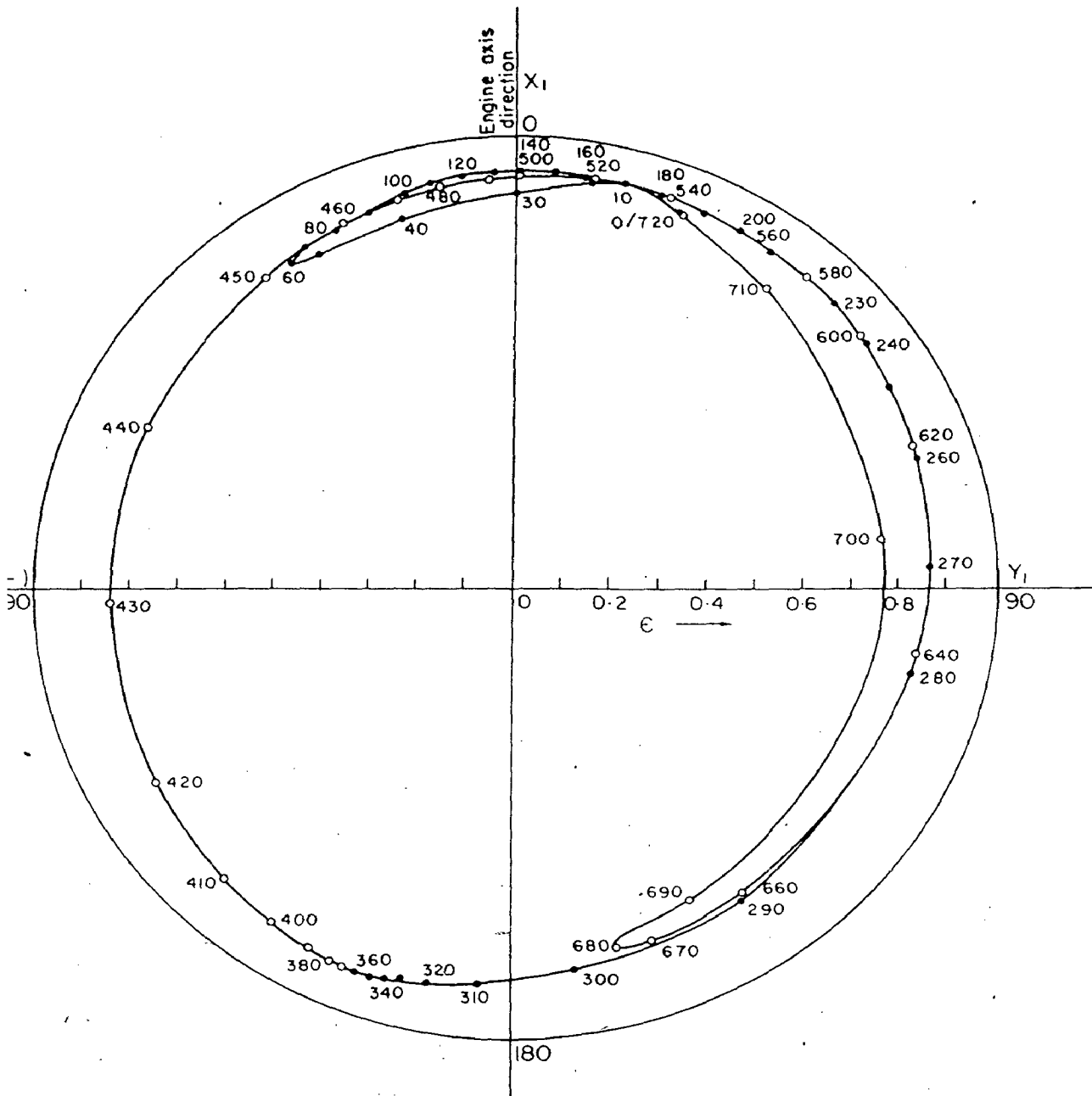


Fig. A-6-1 Bearing centre equilibrium locus



